



Polyphosphate kinase-1 regulates bacterial and host metabolic pathways involved in pathogenesis of *Mycobacterium tuberculosis*

Saurabh Chugh^a , Prabhakar Tiwari^a, Charu Suri^a, Sonu Kumar Gupta^a, Padam Singh^a , Rania Bouzeyen^b, Saqib Kidwai^a, Mitul Srivastava^a, Nagender Rao Rameshwaram^a, Yashwant Kumar^a , Shailendra Asthana^a, and Ramandeep Singh^{a,1}

Edited by Julien Vaubourgeix, Imperial College London, London, United Kingdom; received June 18, 2023; accepted December 1, 2023 by Editorial Board Member Carl F. Nathan

Inorganic polyphosphate (polyP) is primarily synthesized by Polyphosphate Kinase-1 (PPK-1) and regulates numerous cellular processes, including energy metabolism, stress adaptation, drug tolerance, and microbial pathogenesis. Here, we report that polyP interacts with acyl CoA carboxylases, enzymes involved in lipid biosynthesis in *Mycobacterium tuberculosis*. We show that deletion of *ppk-1* in *M. tuberculosis* results in transcriptional and metabolic reprogramming. In comparison to the parental strain, the Δ *ppk-1* mutant strain had reduced levels of virulence-associated lipids such as PDIMs and TDM. We also observed that polyP deficiency in *M. tuberculosis* is associated with enhanced phagosome–lysosome fusion in infected macrophages and attenuated growth in mice. Host RNA-seq analysis revealed decreased levels of transcripts encoding for proteins involved in either type I interferon signaling or formation of foamy macrophages in the lungs of Δ *ppk-1* mutant-infected mice relative to parental strain-infected animals. Using target-based screening and molecular docking, we have identified raloxifene hydrochloride as a broad-spectrum PPK-1 inhibitor. We show that raloxifene hydrochloride significantly enhanced the activity of isoniazid, bedaquiline, and pretomanid against *M. tuberculosis* in macrophages. Additionally, raloxifene inhibited the growth of *M. tuberculosis* in mice. This is an in-depth study that provides mechanistic insights into the regulation of mycobacterial pathogenesis by polyP deficiency.

Mycobacterium tuberculosis | inorganic polyphosphate | virulence-associated factors | target-based screening | pathogenesis

Inorganic polyphosphate (polyP) is present in species from all three kingdoms of life, and enzymes involved in polyP metabolism have been extensively studied in prokaryotes. Polyphosphate kinase-1 (PPK-1) primarily synthesizes polyP using ATP as substrate (1). Polyphosphate kinase-2 (PPK-2) generates polyP from GTP or ATP and uses polyP as a phosphate donor to synthesize GTP or ATP (2–5). Exopolyphosphatases degrade polyP and sequentially remove the terminal phosphate (6, 7). Studies have shown that mycobacteria accumulate polyP during the stationary phase of growth and following exposure to various stress conditions and drugs (8–10). It has been demonstrated that *Mycobacterium smegmatis* and *Mycobacterium tuberculosis* secrete polyP upon infecting *Dictyostelium discoideum* or macrophages and inhibit phagosome acidification and phagosome–lysosome fusion (11). The genome of *M. tuberculosis* encodes homologs of polyphosphate kinases (PPK-1/Rv2984 and PPK-2/Rv3232c) and exopolyphosphatases (PPX-1/Rv0496 and PPX-2/Rv1026) (12). The PPK-2 homolog is required for the survival of *M. smegmatis* in acidic and low-oxygen conditions and is essential for *M. tuberculosis* growth in mice and guinea pigs (5, 13, 14). PPX enzymes from *M. tuberculosis* can utilize polyP, ATP, or GTP as substrates, and their activity is inhibited by (p)ppGpp (15). We have recently shown that simultaneous deletion of *ppx-1* and *ppx-2* from *M. tuberculosis* results in reduced expression of the dormancy-associated genes and attenuated growth in mice and guinea pigs (16).

Previously, we had shown that deletion of *ppk-1* in *M. tuberculosis* is associated with polyP deficiency, increased susceptibility to isoniazid (INH), and attenuated growth in guinea pigs (8). Another study showed that the RNA polymerase binding protein RbpA and sigma factor B (*sigB*) regulate *ppk-1* expression and contribute to INH tolerance (17). In agreement, relative to the wild-type strain, polyP accumulating strains (Δ *ppk-2* strain) were resistant to INH-mediated killing (13, 14). Here, we have performed experiments to delineate the mechanisms by which polyP levels regulate *M. tuberculosis* pathogenesis. We show that polyP interacts with acyl CoA carboxylases (ACC) from *M. tuberculosis*, the enzymes that synthesize precursors for various lipids (18, 19). Further, the Δ *ppk-1*

Significance

Inorganic polyphosphate (polyP), a linear polymer of hundreds of phosphate residues, is synthesized by Polyphosphate kinase-1 (PPK-1). Studies have shown that polyP dysregulation impairs *Mycobacterium tuberculosis* growth in host tissues. Overall, our work provides a detailed mechanistic perspective on regulation of mycobacterial pathogenesis by deletion of *ppk-1*. We show that deletion of *ppk-1* affects glucose utilization and lipid biosynthesis in *M. tuberculosis*. In addition, the lungs of Δ *ppk-1* mutant strain-infected mice had reduced transcript levels of genes encoding for proteins involved in antimicrobial pathways. We have also identified a broad-spectrum inhibitor against the PPK-1 enzyme. We anticipate that PPK-1 targeting small molecules can reduce the duration of chemotherapy and be effective against bacteria that require polyP for virulence.

Author contributions: S.A. and R.S. designed research; S.C., P.T., C.S., S.K.G., P.S., R.B., S.K., M.S., N.R.R., and S.A. performed research; S.C., P.T., C.S., S.K.G., P.S., R.B., S.K., M.S., N.R.R., Y.K., S.A., and R.S. analyzed data; and S.C., C.S., Y.K., S.A., and R.S. wrote the paper.

The authors declare no competing interest.

This article is a PNAS Direct Submission. J.V. is a guest editor invited by the Editorial Board.

Copyright © 2024 the Author(s). Published by PNAS. This article is distributed under Creative Commons Attribution-NonCommercial-NoDerivatives License 4.0 (CC BY-NC-ND).

¹To whom correspondence may be addressed. Email: ramandeep@thsti.res.in.

This article contains supporting information online at <https://www.pnas.org/lookup/suppl/doi:10.1073/pnas.2309664121/-DCSupplemental>.

Published January 3, 2024.

mutant strain has reduced levels of lipids that contribute to mycobacterial pathogenesis relative to the wild-type and complemented strains. We also show enhanced phagosome–lysosome fusion in THP-1 macrophages infected with $\Delta ppk-1$ mutant strain compared to wild-type and complemented strain-infected macrophages. In comparison to the parental strain, lung transcriptional profiling revealed reduced expression of proteins involved in inflammatory pathways in lung tissues from $\Delta ppk-1$ mutant-infected mice. In the present study, we have identified raloxifene hydrochloride as a broad-spectrum PPK-1 inhibitor. The identified small molecule enhanced the activity of known anti-TB drugs in an additive manner and inhibited the growth of intracellular *M. tuberculosis* in macrophages and mice. Taken together, targeting the PPK-1 enzyme represents an approach for shortening the duration of therapy for drug-susceptible and drug-resistant *M. tuberculosis*.

Results

Acyl CoA Carboxylases from *M. tuberculosis* Interact with polyP. In order to identify polyP-interacting proteins from *M. tuberculosis*, pull-down experiments were performed using biotinylated polyP₇₀₀ (Fig. 1A). Using clarified lysates prepared from either mid-log or late-log phase, 11- and 20- polyP₇₀₀ interacting proteins were identified (Fig. 1B). Among these, eight interacting proteins were common in lysates prepared from mid-log and late-log phase *M. tuberculosis* cultures (SI Appendix, Table S1 and Dataset S1). Interestingly, the majority of the

commonly identified polyP₇₀₀ interacting proteins belonged to the ACC family of enzymes. These included AccA1 (Rv2501c), AccD1 (Rv2502c), AccA2 (Rv0973c), AccD2 (Rv0974c), AccD4 (Rv3799c), AccD5 (Rv3280), and AccE5 (Rv3281) (SI Appendix, Table S1 and Dataset S1). Since polyP has been demonstrated to replace ATP as a phosphate donor in various metabolic enzymatic reactions, we hypothesized that ACC enzymes can bind both ATP and polyP (20, 21). In our bio-layer interferometry (BLI) experiments, (His)₆-AccA1, (His)₆-AccD1, and (His)₆-PPK-1 showed a simple 1:1 binding with biotinylated polyP₇₀₀ (Fig. 1C). We did not observe binding of biotinylated polyP₇₀₀ with the remaining purified proteins. These observations suggest that AccA2, AccD2, AccD4, AccD5, and AccE5 might not interact directly and require an accessory *M. tuberculosis* protein or factor to interact with polyP. The dissociation constant (K_d) for (His)₆-AccA1 binding with polyP₇₀₀ and polyP₄₅ was 1.43 μ M and 1.1 μ M, respectively (Fig. 1D). In comparison, (His)₆-AccD1 displayed K_d values of 1.1 μ M for both polyP₇₀₀ and polyP₄₅ (Fig. 1D). As shown in SI Appendix, Fig. S1 A and B, no interaction was observed between (His)₆-AccA1 and (His)₆-AccD1 with polyP₃. Further, we performed molecular modeling and docking studies to identify polyP binding pockets in AccA1 and AccD1. We identified three and five potential clusters for polyP binding with AccA1 and AccD1, respectively (Fig. 1 E and F). Further, to establish the most likely orientation of polyP binding, focused docking was performed utilizing cluster representatives (as grid). For AccA1, the lowest docking energy and the highest population of polyP poses (number of conformations) were -4.0 kcal/mol and

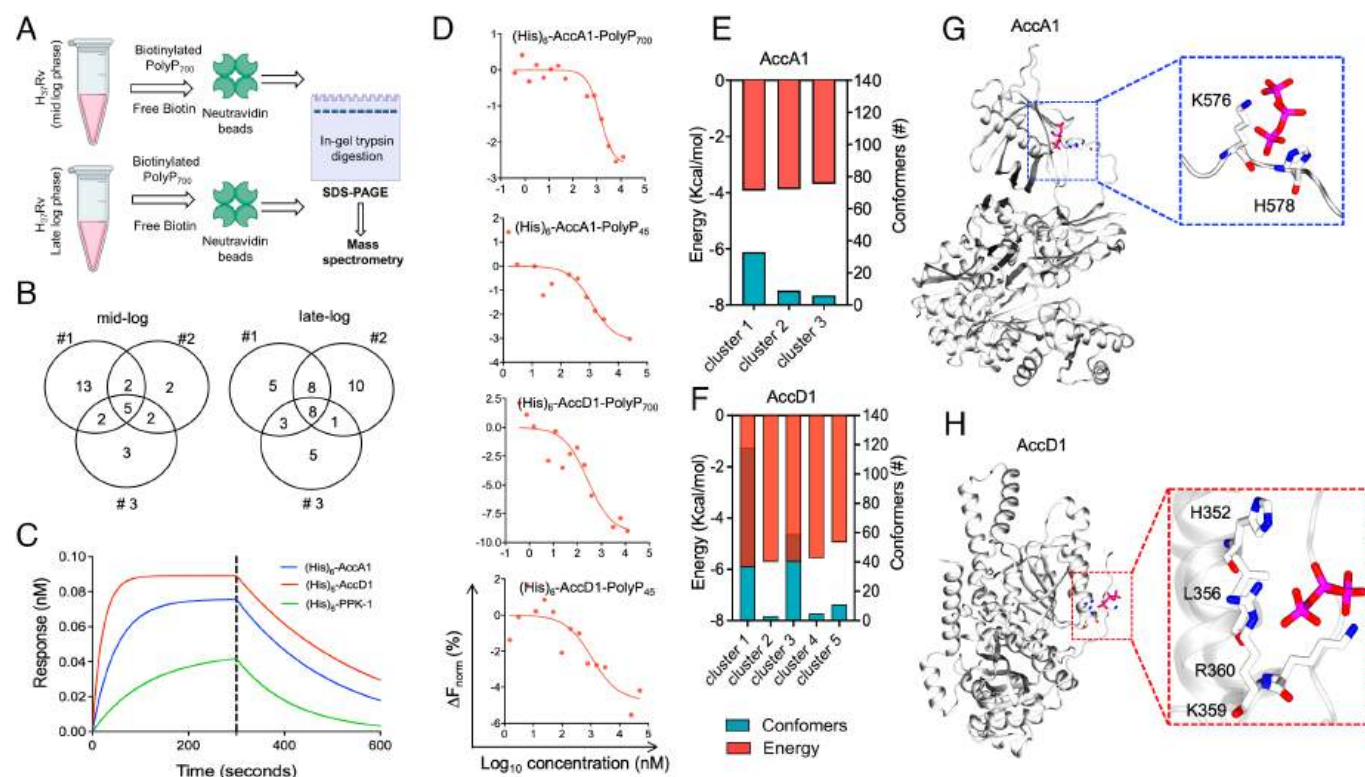


Fig. 1. Inorganic polyphosphate interacts with AccA1 and AccD1 enzymes from *M. tuberculosis*. (A) Schematic diagram showing the experimental design for identification of polyP₇₀₀ interacting proteins from *M. tuberculosis*. (B) Venn diagrams depicting the number of polyP₇₀₀ interacting proteins identified in three replicative samples from either mid-log or late-log phase cultures. (C) BLI sensogram showing the interaction between biotinylated polyP₇₀₀ with either (His)₆-AccA1 or (His)₆-AccD1 or (His)₆-PPK-1. (D) The binding affinity of (His)₆-AccA1 and (His)₆-AccD1 with either polyP₇₀₀ or polyP₄₅ was determined using MST. The data shown in panels (C) and (D) are representative of two independent experiments. (E and F) These panels represent the top clusters obtained from blind docking of polyP with AccA1 and AccD1. (G and H) The most likely pose of polyP binding on the modeled structure of AccA1 and AccD1 is shown. The zoom-in *Inset* highlights the critical residues of proteins that might be involved in polyP binding. The polyP and interacting residues are shown in licorice and colored atom-wise: C: magenta/white, N: blue, O: red, respectively.

32, respectively (Fig. 1E). For AccD1, the lowest docking energy and the highest population of polyP poses were -6.0 kcal/mol and 120, respectively (Fig. 1F). Interaction mapping analysis revealed that Lys576 and His578 of AccA1 and His352, Leu356, Lys359, and Arg360 of AccD1 might interact with polyP (Fig. 1G and H). In agreement with molecular docking studies, in comparison to wild-type protein, we observed significantly reduced binding of (His)₆-AccD1^{L356A} with biotinylated polyP₇₀₀ (SI Appendix, Fig. S1C). Taken together, these observations suggest that polyP interacts with AccA1 and AccD1 from *M. tuberculosis*.

Deletion of PPK-1 in *M. tuberculosis* Affects the Expression of Virulence-Associated Factors and Enhances Phagosome-Lysosome Fusion. In order to understand the mechanisms by which PPK-1 contributes to mycobacterial pathogenesis, we compared the transcription profiles of mid-log phase cultures of wild-type and $\Delta ppk-1$ mutant strains. We observed that, in comparison to the parental strain, the expression of 247 and 183 transcripts were decreased and increased, respectively, in $\Delta ppk-1$ mutant strain (Fig. 2A and Dataset S2). Functional categorization of these differentially expressed genes (DEGs) revealed that the majority of these encodes for conserved hypothetical proteins (CHP) or proteins involved in either intermediary metabolism

and respiration (IMR) or cell wall (CW) processes (SI Appendix, Table S2). This transcriptional reprogramming observed in the $\Delta ppk-1$ mutant strain might be associated with the differential expression of various regulatory proteins such as Rv2034, Rv1845c, Rv1773c, Rv3082c, Rv0485, Rv3173c, Rv2745c, Rv1152, Rv0377, Rv2642, Rv0353, Rv3058c, Rv3132c, Rv1129c, Rv0894, Rv0490, Rv3416, and Rv2011c (Fig. 2B). There is a possibility that polyP regulates the activity of these transcription factors, as reported for RpoS from *Escherichia coli* (22). Few of the transcripts with reduced expression encode for metabolic enzymes involved in either the production of cobalamin or porphyrin, storage or transport of metal ions, or peptidoglycan synthesis (Fig. 2C). The transcript levels of genes encoding for various ribosomal and ribosome-associated proteins were also increased in the $\Delta ppk-1$ mutant strain relative to the parental strain (Fig. 2D). These findings indicate a lower rate of translation in the $\Delta ppk-1$ mutant strain relative to the wild type, a phenomenon observed in *M. tuberculosis* upon nutrient deprivation (23). We also observed that transcripts of genes encoding for various toxin-antitoxin (TA) systems were differentially expressed between these two strains (Fig. 2E). Among these, transcript levels of the *vapBC15* TA system were increased by ~ 16.0 folds in the $\Delta ppk-1$ mutant strain relative to the parental strain (Fig. 2E and Dataset S2).

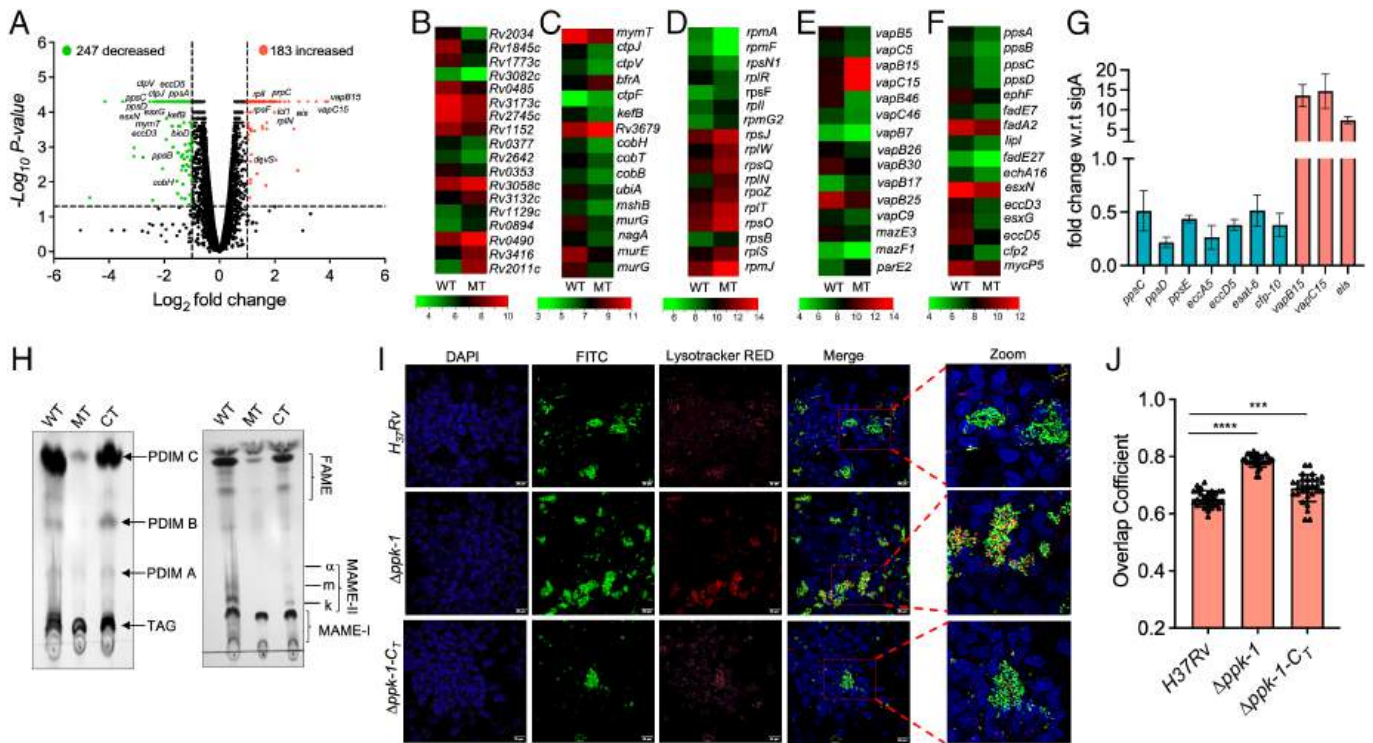


Fig. 2. (A–F) Effect of *ppk-1* deletion on the transcriptional profiles of *M. tuberculosis* (A) This panel shows the volcano plot comparing the expression profiles obtained from mid-log phase cultures of wild-type and $\Delta ppk-1$ mutant strain. (B–F) Heatmaps depicting differentially expressed transcripts involved in gene regulation (B), metal ion transport/cell wall biosynthesis (C), ribosomal proteins (D), toxin-antitoxin systems (E), and PDIMs biosynthesis/Type VII secretion system (F) in mid-log phase cultures of $\Delta ppk-1$ mutant strain relative to the parental strain. The color intensity in heatmaps represents the \log_2 value of raw read counts. (G) The transcript levels of various differentially expressed transcripts between $\Delta ppk-1$ mutant and parental strain were quantified using qPCR. The data obtained were normalized to *sigA* levels and are shown as mean \pm SE of relative fold change with respect to the parental strain. (H) Effect of *ppk-1* deletion on lipid biosynthesis in *M. tuberculosis*. This panel shows the profiles of apolar lipids isolated from mid-log phase cultures of various strains. WT, MT, and CT represent wild-type, $\Delta ppk-1$ mutant, and complemented strains. TAG, triacylglycerol; PDIM, phthiocerol dimycocerosate; FAME, fatty acid methyl esters; MAME, mycolic acid methyl esters. The data shown in panels (A–F and H) are obtained from two biological replicates. The data shown in (G) are obtained from two independent experiments performed in duplicates. (I and J) Deletion of *ppk-1* enhances phagosome-lysosome fusion in THP-1 macrophages infected with *M. tuberculosis*. (I) THP-1 macrophages were infected with FITC-labeled strains. The images were acquired using an Olympus FV3000 confocal microscope at 60 \times magnification. (Scale bars, 20 μ m.) (J) The overlap coefficient for co-localization between red and green fluorescent signals for all three strains was calculated using Olympus cellSens software. The data shown in this panel are mean \pm SE for the overlap coefficient calculated using 30 z-stacked images obtained from two independent experiments. The data were statistically analyzed by one-way ANOVA (*** P < 0.001, **** P < 0.0001). Photo credit: Mr. Saurabh Chugh, Translational Health Science and Technology Institute.

Intriguingly, the mutant strain also had reduced transcript levels of genes encoding for enzymes involved in either phthiocerol dimycocerosates (PDIM) biosynthesis (*pps* gene cluster, *ppsAB-CDE*) or components of type VII secretion systems (*eccD3*, *eccD5*, *esxG*, *esxN* and associated protease *mycP5*, Fig. 2F). The differential expression of a subset of these DEGs in *Δppk-1* mutant strain relative to the parental strain was confirmed by qPCR (Fig. 2G). In agreement with RNA-seq data, relative to the wild-type and complemented strain, levels of PDIMs, fatty acid methyl esters (FAMES), and mycolic acid methyl esters (MAME-II) were reduced in mid-log phase cultures of *Δppk-1* mutant strain (Fig. 2H). However, the levels of triacylglycerols and MAME-I were comparable in these strains (Fig. 2H). It has been previously shown that proteins belonging to ESX-1 and PDIMs are required for phagosome rupture and escape of *M. tuberculosis* to the cytosol (24, 25). In agreement, we found that THP-1 macrophages infected with the *Δppk-1* mutant strain showed increased phagosome-lysosome fusion compared to wild-type and complemented strain-infected macrophages (Fig. 2I and J). Taken together, these findings suggest that deletion of *ppk-1* leads to reduced levels of PDIMs, FAMES, and MAMEs and enhanced phagosome-lysosome fusion-mediated killing of *M. tuberculosis*.

Deletion of *ppk-1* Perturbs the Central Carbon and Trehalose Metabolism in *M. tuberculosis*. Previous studies have shown that *M. tuberculosis* glucokinase mainly utilizes polyP as the phosphate donor to convert glucose into glucose 6-phosphate (26, 27). Therefore, we

next compared the growth patterns of various strains in a medium containing glucose, glycerol, or cholesterol as the sole carbon source. The *Δppk-1* mutant strain displayed slower growth in a medium containing glucose in comparison to parental and complemented strains (Fig. 3A). However, the growth patterns of these strains were comparable in a medium containing either glycerol or cholesterol as the sole carbon source (SI Appendix, Fig. S2 A and B). We next performed untargeted metabolomics of samples prepared from mid-log phase cultures of wild-type and *Δppk-1* mutant strains grown in either complete 7H9 or glucose-containing medium. Principal component analysis revealed that the metabolite profiles obtained for both strains in a glucose-containing medium were more distinct than those obtained in the 7H9 medium (SI Appendix, Fig. S2 C and D). The relative levels of 91 and 24 metabolites were significantly altered between these two strains upon culturing in glucose-containing or complete 7H9 medium, respectively (Fig. 3B and C and Dataset S3). As expected, glucose 6-phosphate levels were significantly reduced in the *Δppk-1* mutant strain relative to the wild-type strain in both growth conditions (Fig. 3E). Also, the levels of intermediates from the pentose phosphate pathway (ribose-5-phosphate) and tricarboxylic acid (TCA) cycle (citric acid, succinate, fumarate, and malate levels) were reduced in the *Δppk-1* mutant strain upon culturing in glucose-containing medium (Fig. 3E). The levels of dihydroxyacetone phosphate and aconitate were non-significantly reduced in the *Δppk-1* mutant strain in the glucose-containing medium in comparison to the parental strain. The peaks corresponding to other intermediates of glycolysis and the pentose

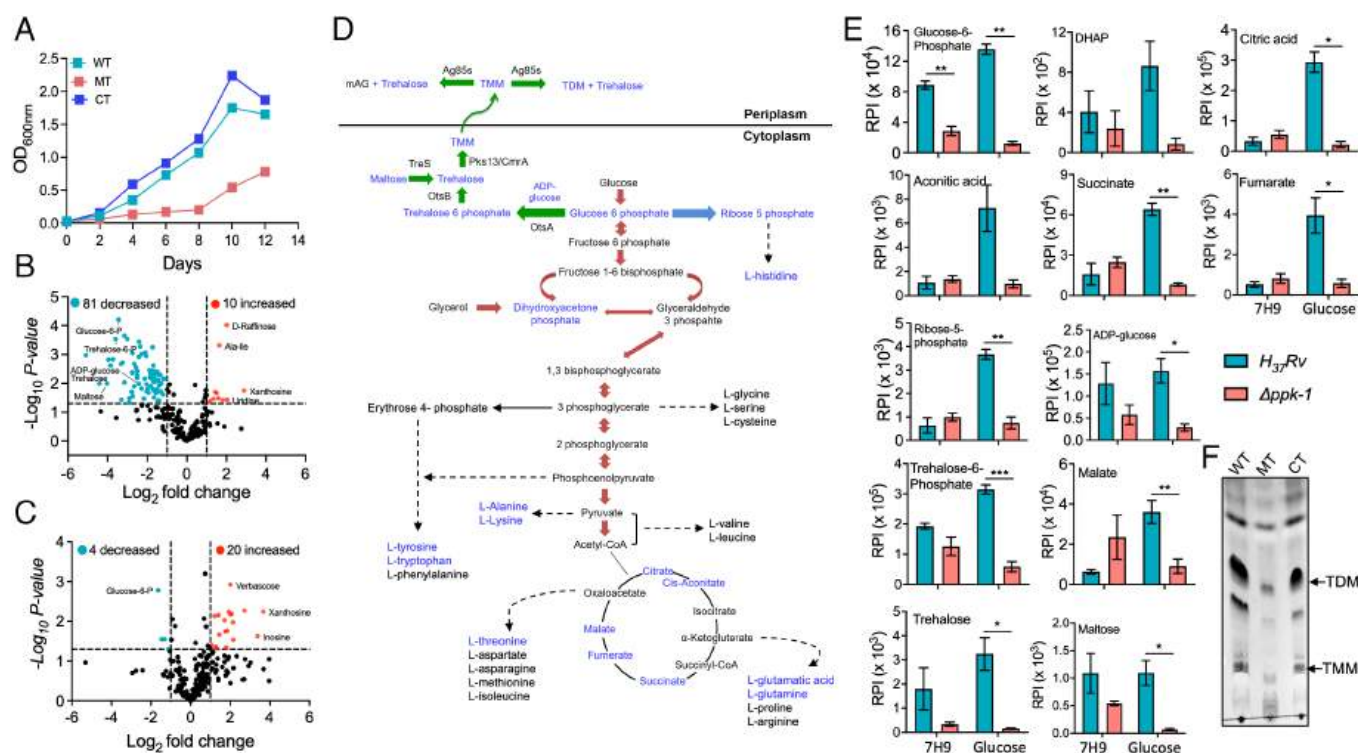


Fig. 3. Deletion of *ppk-1* perturbs central carbon and trehalose metabolism in *M. tuberculosis*. (A) The growth pattern of wild-type, *Δppk-1* mutant, and complemented strain was compared in the glucose-containing medium by measuring OD_{600nm} at regular intervals. The data shown in this panel are representative of two independent experiments. (B and C) This panel shows the volcano plot highlighting the relative metabolite levels in *Δppk-1* mutant and wild-type strains upon culturing in glucose-containing medium (B) or 7H9 (C) for 7 d. The data shown in panels (B) and (C) are obtained from three biological replicates. (D) A schematic showing the central carbon metabolism and TMM/TDM biosynthesis pathways in *M. tuberculosis*. The levels of metabolites highlighted in blue were reduced in the *Δppk-1* mutant strain relative to wild-type strain in glucose-containing medium. (E) This panel shows the relative levels of various metabolites in wild-type (blue bar) and *Δppk-1* mutant strain (red bar) upon culturing in either a complete 7H9 medium or in glucose-containing medium for 7 d. The data shown in this panel are mean \pm SE obtained from three replicates. RPI represents relative peak intensity. The data were statistically analyzed using the paired-two-tailed t test (* P < 0.05, ** P < 0.01, and *** P < 0.001). (F) Equal amount of TMM and TDM isolated from various strains was spotted on silica TLC plates, resolved, and analyzed. The data shown in this panel are representative of two independent experiments. TMM and TDM represent trehalose monomycolate and trehalose 6'6'-dimycolate, respectively. WT, MT, and CT represent wild-type, *Δppk-1* mutant, and complemented strains. Photo credit: Mr. Saurabh Chugh, Translational Health Science and Technology Institute.

phosphate pathway were not detected in our metabolite experiments. The intermediates of central carbon metabolism serve as precursors for amino acid synthesis in prokaryotes (Fig. 3D) (28). We observed that the levels of several amino acids were significantly reduced in $\Delta ppk-1$ mutant strain in a glucose-containing medium compared to the parental strain (SI Appendix, Fig. S2E). We also compared the metabolomic profiles of polyP deficient ($\Delta ppk-1$) and polyP accumulating (*dkppx*) strain in 7H9 medium. In comparison to *dkppx* strain, the levels of glucose-6-phosphate were reduced in the $\Delta ppk-1$ mutant strain (SI Appendix, Fig. S3A). Previously, it has been shown that the levels of pyrophosphate, NAD⁺, NADH, nicotinamide, malate, succinate, 2-methyl citrate, acetyl-CoA, and metabolites belonging to arginine metabolism such as arginine, citrulline, and ornithine were increased in $\Delta ppk-1$ mutant strain relative to the parental strain (29). In agreement, we noticed increased levels of NAD and ornithine in the *dkppx* strain relative to the $\Delta ppk-1$ mutant strain (SI Appendix, Fig. S3A). Interestingly, the levels of metabolites belonging to purine metabolism were altered between $\Delta ppk-1$ and *dkppx* strain (SI Appendix, Fig. S3B). We observed that the levels of ribose-5-phosphate, guanosine monophosphate, 5-aminoimidazole-4-carboxamide-1- β -D-ribofuranosyl 5'-monophosphate and inosine monophosphate were increased in *dkppx* strain in comparison to the $\Delta ppk-1$ mutant strain (SI Appendix, Fig. S3C). Also, we observed decreased levels of guanosine, inosine, and hypoxanthine in the *dkppx* strain relative to the $\Delta ppk-1$ mutant strain (SI Appendix, Fig. S3C). These observations suggest that polyP accumulation might inhibit the enzymes involved in the synthesis of guanosine, inosine, and hypoxanthine in *M. tuberculosis*.

It has been previously shown that glucose-6-phosphate is a precursor for synthesizing trehalose-6-phosphate and ADP-glucose, key intermediates in trehalose biosynthesis (Fig. 3D) (12, 30–33). We observed that relative to the wild-type strain, levels of trehalose-6-phosphate, the glycosyl donor, ADP-glucose, maltose, and trehalose were reduced in $\Delta ppk-1$ mutant strain in glucose-containing medium (Fig. 3E). We did not observe any significant differences in the levels of these intermediates between the two strains upon culturing in 7H9 medium (Fig. 3E). The levels trehalose-6-phosphate, trehalose, and ADP-glucose were also reduced in $\Delta ppk-1$ mutant strain relative to the *dkppx* strain in 7H9 medium (SI Appendix, Fig. S3A). Trehalose acts as a precursor for the biosynthesis of trehalose monomycolate (TMM), trehalose 6-6'-dimycolate (TDM), and mycolyl-arabinogalactan (mAG) in *M. tuberculosis* (34, 35). In agreement with our metabolomics data, the levels of TMM and TDM were also reduced in the $\Delta ppk-1$ mutant strain relative to the wild-type and complemented strains (Fig. 3F). In conclusion, we observed perturbations in central carbon metabolism and TMM/TDM biosynthesis upon deletion of *ppk-1* in *M. tuberculosis*.

Characterization of the Lung Transcriptional Signatures of Mice Infected with Parental and $\Delta ppk-1$ Mutant Strain. Previously, we reported that, compared to the wild-type strain, the $\Delta ppk-1$ mutant strain was attenuated for growth in guinea pigs (8). In the present study, we compared the growth of parental and $\Delta ppk-1$ mutant strains in aerosol-infected mice. The mice infected with the $\Delta ppk-1$ mutant strain displayed ~25.5-fold and ~95.0-fold reduced lung bacillary load in comparison to mice infected with the parental strain at 2 and 4 wk post-infection, respectively (Fig. 4A). In agreement, the splenic bacillary loads were also significantly reduced in $\Delta ppk-1$ mutant strain–infected mice at 4-wk post-infection (Fig. 4A). It has been shown that lipids are key components of the immune evasion strategy and are essential for intracellular growth of *M. tuberculosis* (36). Since the virulence-associated lipids levels were reduced in the mutant strain, we next

performed whole lung transcriptional profiling of wild-type and $\Delta ppk-1$ mutant strain–infected mice at 4 wk post-infection to investigate the effect of polyP deficiency on modulation of host antimicrobial pathways. We observed that the levels of 1100 (334 decreased and 766 increased) and 618 (242 decreased and 376 increased) transcripts were significantly altered in the lung tissues of naive versus wild type–infected and naive versus $\Delta ppk-1$ -infected mice, respectively (Fig. 4B and SI Appendix, Fig. S4 A and B and Dataset S4). We observed that the expression of 453 and 289 transcripts was decreased and increased, respectively, in the lung tissues of animals infected with the $\Delta ppk-1$ mutant strain relative to wild type–infected animals (Fig. 4C and Dataset S4). It has been shown that PDIMs are responsible for the coordinated secretion of ESAT-6 and CFP-10, which leads to phagosome rupture and the induction of Type I IFN signaling (25). In agreement, a subset of transcripts involved in Type I IFN signaling such as guanylate binding proteins (*gbp2a*, *gbp5*), *socs1*, *il-27*, *stat1*, and chemokines such as *cxcl10*, *cxcl9*, and *ccl5* were reduced in lung tissues of $\Delta ppk-1$ mutant–infected mice relative to mice infected with the parental strain (Fig. 4D and Dataset S4) (37). The death of *M. tuberculosis*–infected cells in a necrotic manner and subsequent inflammation has also been associated with phagosome rupture, an increase in cytosolic Ca²⁺, the generation of reactive oxygen species and ATP depletion (38, 39). We observed that the transcripts of genes associated with cell death (*pdcd1lg2*, *skap1*, *pdcd1*, *bcl2l15*, *sirt3*, *fasl*, and *aif1*), calcium transport channels (*cacna1c*, *cant1*, *c2cd4a*, *cabp4*, and *s100a14*), and potassium ions transporters (*dpp6*, *kcnt1*, *kctd18*, and *kcnj10*) were significantly decreased in the lung tissues of mice infected with $\Delta ppk-1$ mutant (Fig. 4E and Dataset S4). Several studies have shown that zinc is essential for virulence of various bacterial pathogens, including *M. tuberculosis* (40, 41). In accordance, in mice infected with the mutant strain, the expression of zinc finger proteins and gene clusters involved in zinc ion binding (such as *zfp661*, *zkscan5*, *zfx*, *zfp639*, *zfp60*, *zfp740*, *zfp219*, *zfp945*, *mefu*, *zfp37*, *zfp277*, *zfp386*, and *zfp82*) was also decreased (SI Appendix, Fig. S4C and Dataset S4).

It has been reported that *M. tuberculosis* utilizes PDIM-related surface lipids to recruit neutrophils and permissive monocytes, which subsequently leads to inflammation and disease severity in host tissues (42). In addition, PDIMs also obscure mycobacterial pathogen-associated molecular patterns (PAMPs) to inhibit toll-like receptor-mediated recruitment of microbicidal macrophages (43). In agreement, levels of transcripts encoding for various chemokines involved in monocytes and PMN-recruitment, such as *cxcl5*, *cxcl13*, *ccl2*, *ccl4*, and *ccl19*, were decreased in lung tissues of $\Delta ppk-1$ infected mice relative to animals infected with the wild-type strain (SI Appendix, Fig. S4D and Dataset S4). It has also been shown that *M. tuberculosis* cell wall lipids are crucial for mounting maximal T cell responses that contribute to TB pathogenesis (44). In agreement with reduced levels of virulence-associated lipids, we observed that the transcript levels of various pro-inflammatory and T cell cytokines, including *ifn- γ* , *tnf- α* , *il-12*, *il-17*, and *il-21* as well as T cell activated related markers such as *cd44* and *il-2* were reduced in lung tissue of $\Delta ppk-1$ infected mice when compared to wild type–infected mice (SI Appendix, Fig. S4E and Dataset S4). In concordance, the levels of IL-17A, IFN- γ , and TNF- α were reduced by 2.4-fold, 4.5-fold, and 3.0-fold, respectively, in lung homogenates of $\Delta ppk-1$ mutant strain–infected animals in comparison to wild type–infected animals (SI Appendix, Fig. S4F). However, no differences were observed in IL-10 levels in lung homogenates of mice infected with either the parental or $\Delta ppk-1$ mutant strain at days 28 post-infection (SI Appendix, Fig. S4F).

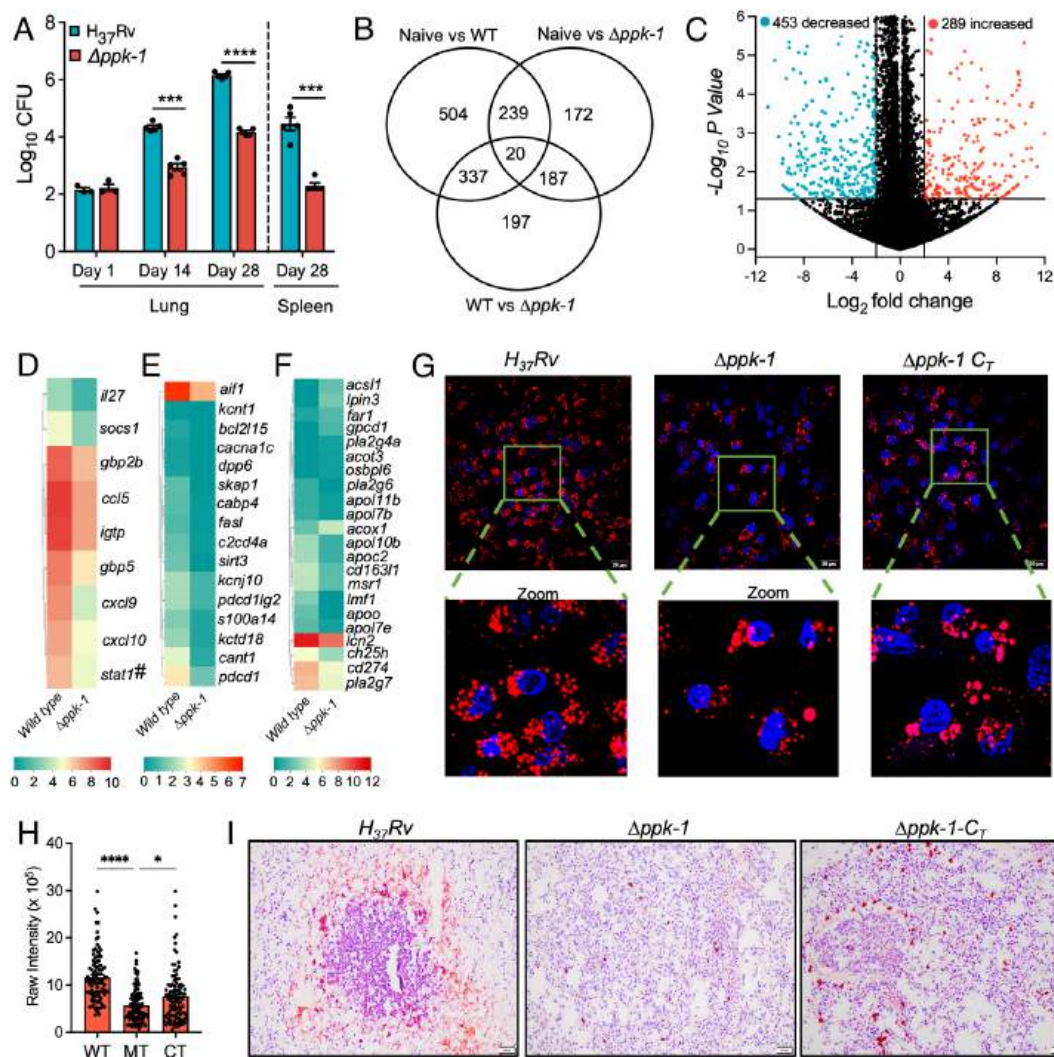


Fig. 4. (A) Deletion of *ppk-1* attenuates *M. tuberculosis* growth in mice. The data shown are mean \pm SE of \log_{10} of lung and splenic bacillary loads in mice infected with wild-type or $\Delta ppk-1$ mutant strain at days 1, 14, and 28 post-infection. The data were statistically analyzed using the paired-two-tailed *t* test (*** P < 0.001, **** P < 0.0001). (B and C) Comparison of transcriptional profiles obtained from lung tissues of naive or wild type-infected or $\Delta ppk-1$ mutant strain-infected mice. (B) Venn diagram showing correlation of expression profiles obtained from lung tissues of naive or wild type-infected or $\Delta ppk-1$ mutant strain-infected mice at days 28 post-infection. (C) The volcano plot shows comparative gene expression profiles from mice infected with either wild-type or $\Delta ppk-1$ mutant strain of *M. tuberculosis*. (D–F) Heatmaps showing differentially expressed transcripts in lungs of mice infected with either wild or $\Delta ppk-1$ mutant strain. These transcripts showing differential expression are involved in either Type I IFN signaling (D) or cell death, calcium and potassium transport channel (E) or foamy macrophages and lipids metabolism (F). The data shown are obtained from three biological replicates. #: The expression of *stat1* was reduced by 3.91-fold in $\Delta ppk-1$ mutant-infected mice relative to wild type-infected mice. The color intensity in heatmaps represent the \log_2 value of raw read counts. (G and H) Nile Red staining in macrophages infected with either wild type or $\Delta ppk-1$ mutant or complemented strain of *M. tuberculosis*. (G) THP-1 macrophages were infected with various strains and stained with Nile Red. The images were acquired using an Olympus FV3000 confocal microscope at 60 \times magnification. (Scale bars, 20 μ m.) (H) The raw intensity of Nile red-stained macrophages was quantified using Image J software. The data shown in this panel are mean \pm SE values of raw intensity obtained from 10 images from two independent experiments. The data obtained were statistically analyzed by one-way ANOVA (* P < 0.05; **** P < 0.0001). Photo credit: Mr. Saurabh Chugh, Translational Health Science and Technology Institute. (I) Oil red O and hematoxylin staining of lung sections of guinea pigs infected with various strains of *M. tuberculosis*. The representative Oil red O and hematoxylin stained lung sections from guinea pigs infected with various strains at days 28 post-infection is shown in this panel. The red color indicates the ORO-positive region. Images were acquired using an Olympus CX 43 microscope at 20 \times objective. (Scale bars, 20 μ m.) Photo credit: Dr. Bhisma Panda, Translational Health Science and Technology Institute.

Upon infection with *M. tuberculosis*, macrophages differentiate into lipid-overloaded foamy macrophages that accumulate cholesteryl esters and triglycerides, which serve as primary carbon sources for *M. tuberculosis* growth in vivo (45–47). *M. tuberculosis* infection induces the expression of proinflammatory cytokines such as IFN- γ and TNF- α , which contribute to the formation of foamy cells (48, 49). In addition, *M. tuberculosis*-infected macrophages release mycobacterial cell wall lipid-containing vesicles (TDM and oxygenated forms of mycolic acids), transforming surrounding infected and uninfected macrophages into foamy cells (50). In our RNA-seq data, transcript levels of genes encoding for foamy cell markers such as scavenger receptors (*msr1*, *cd163*)

and the checkpoint inhibitor *pd1* (*cd274*) were reduced in mice infected with the $\Delta ppk-1$ mutant strain relative to the parental strain-infected mice. In addition, the transcript levels of genes involved in lipid catabolism (such as *lmf1*, *apol10b*, *apoo*, *apol7e*, *pla2g7*, *pla2g6*, *apoc2*, *lcn2*, *apol11b*, *apol7b*, *ch25h*, *ccl1*, *cxox1*, *pla2g4a*, *far1*, *gpcpd1*, *lpin3*, *acot3*, and *osbp16*) were also differentially expressed in $\Delta ppk-1$ mutant-infected mice (Fig. 4F and Dataset S4). These observations suggest that infection of mice with the $\Delta ppk-1$ mutant strain might reduce foamy macrophage formation in lung tissues. In agreement with the RNA-seq data, we observed that THP-1 macrophages infected with the $\Delta ppk-1$ mutant strain had reduced lipid content compared to wild-type

and complemented strain-infected macrophages (Fig. 4 *G* and *H*). The lung sections of wild-type infected guinea pigs showed well-formed caseous lesions with a central necrotic core where oil red O positive cells organized as a cuff surrounding the central necrotic core (Fig. 4*I*). The lung sections of guinea pigs infected with the $\Delta ppk-1$ mutant strain showed significantly reduced oil red O staining in comparison to wild-type infected guinea pigs (Fig. 4*I*). We also observed that this defect was partially restored in guinea pigs infected with the complemented strain (Fig. 4*I*). Taken together, our data suggest that PPK-1 regulates *M. tuberculosis* virulence, the induction of type I interferon responses, inflammatory responses to exacerbate pathogenesis, and the formation of foamy macrophages in lung tissues.

Target-Based Screening Identifies Broad-Spectrum PPK-1 Inhibitor. Previous studies have shown that various microorganisms require PPK-1 for stress adaptation, virulence, and persistence (51, 52). These observations suggest that PPK-1 is an attractive target to identify small molecule inhibitors with a specific mechanism of action. In the present study, a collection of 1,280 pharmacologically active compounds belonging to the Sigma Lopac 1280 library was screened to identify small molecule inhibitors of PPK-1 (*SI Appendix, Fig. S5A*). The preliminary screening performed at 100 μ M concentration resulted in the identification of 60 compounds that inhibited PPK-1 enzymatic activity by at least 50% (*SI Appendix, Fig. S5B*). Among these, we shortlisted 11 molecules that were either FDA-approved or are in trials for clinical use against other diseases. These molecules did not inhibit luciferase activity but reduced PPK-1 enzymatic activity in vitro in a dose-dependent manner (*SI Appendix, Fig. S5C and D*). The structure, names, and TC_{50} values of the identified PPK-1 inhibitors are shown in *SI Appendix, Fig. S5E*. Among the identified small molecules, antimycobacterial activity has already been reported for trifluperazine (Cpd-1), perphenazine (Cpd-2), prochlorperazine (Cpd-4), and fluphenazine (Cpd-6) (53–55). We next determined the interaction of the remaining small molecules with PPK-1 using microscale thermophoresis (MST). As shown in Fig. 5*A*, Cpd-11, raloxifene hydrochloride (raloxifene) showed the highest binding with PPK-1. We further show that raloxifene binds to PPK-1 in a dose-dependent manner and displays K_d value of 40 μ M (Fig. 5*B*). As shown in Fig. 5 *C* and *D*, raloxifene inhibited both ATP and polyP synthesis activity associated with PPK-1 in a dose-dependent manner. We also observed that the Michaelis–Menten constant of PPK-1 for ADP increased by 2.73-fold and 1.70-fold in the presence of 6.25 μ M and 12.5 μ M of raloxifene, respectively (Fig. 5*E*). Further, in comparison to no drug control, V_{max} of the enzymatic reaction decreased by 2.4-fold and 6.1-fold in the presence of 6.25 μ M and 12.5 μ M of raloxifene, respectively (Fig. 5*E*). These data suggest that raloxifene inhibits PPK-1 protein by binding to a pocket other than the substrate binding site.

PPK-1 is a highly conserved enzyme in various bacterial pathogens, including *E. coli* and *Klebsiella pneumoniae* (56). We observed raloxifene inhibited the enzymatic activity associated with PPK-1 homologs from *E. coli* and *Klebsiella pneumoniae* by >95% (Fig. 5 *F* and *G*). Recently, mesalamine and gallein have been identified as inhibitors of PPK-1 enzymes from *E. coli* and *Pseudomonas aeruginosa*, respectively (57, 58). We observed that gallein inhibited both ATP and polyP synthesis activity associated with the PPK-1 homolog from *M. tuberculosis* (*SI Appendix, Fig. S6A–C*). However, mesalamine did not inhibit *M. tuberculosis* PPK1 enzymatic activity in vitro (*SI Appendix, Fig. S6D*). We next determined the levels of intracellular polyP in *E. coli* and *M. tuberculosis* in the presence of mesalamine, gallein, or raloxifene. As shown in Fig. 5*H*, exposure of *E. coli* to mesalamine and raloxifene

significantly reduced the intracellular polyP levels by ~50 to 65%. Also, treatment with raloxifene and gallein reduced the levels of intracellular polyP by ~35 to 55% in *M. tuberculosis* (Fig. 5*H*). These results imply that raloxifene and gallein are broad-spectrum PPK-1 inhibitors.

Identification of Critical Residues Involved in Raloxifene Binding with PPK-1 Homologs from Various Microorganisms. Using the SiteMap module, we identified Site1, Site2, and Site3 as probable raloxifene binding sites in the *M. tuberculosis* PPK-1 enzyme. The docking on these sites revealed that raloxifene binds at Site 1, Site 2, and Site 3 with GlideXp scores of –7.26 kcal/mol, –6.42 kcal/mol, and –4.14 kcal/mol, respectively (*SI Appendix, Table S3*). To further define the binding pose of raloxifene, Site 1 and Site 2 were re-scored using focused docking and MM-GBSA methods. We observed that raloxifene strongly binds to Site 2, with docking and MM-PBSA scores of –10.25 kcal/mol and –85.89 kcal/mol, respectively (*SI Appendix, Table S3*). The docking and MM-PBSA scores for raloxifene binding to Site 1 were –8.09 kcal/mol and –61.54 kcal/mol, respectively (*SI Appendix, Table S3*). We next identified *hot-spot* residues involved in establishing diverse interactions with raloxifene, such as electrostatic, non-polar, hydrogen bonds, and salt bridges. We noticed that raloxifene forms durable hydrogen bonds with Val98, Glu289, Arg674, and Asn675 of the PPK-1 protein from *M. tuberculosis* (Fig. 5*I* and *SI Appendix, Table S4*). Additionally, we observed the formation of a salt bridge between the Glu289 residue of PPK-1 protein and raloxifene (Fig. 5*I* and *SI Appendix, Table S4*). These observations suggest that Glu289 is critical for the stability of raloxifene inside the binding pocket as it forms intra hydrogen bonds with residues Arg310 and Phe462 in the APO protein (Fig. 5*J*). In addition, Glu57, Glu94, Val98, Asp287, Val290, Glu457, Asp670, and Glu681 of PPK-1 protein are also involved in raloxifene binding (Fig. 5*J*).

We also performed MD simulations to assess further the docking results for raloxifene binding with *M. tuberculosis* PPK-1. The rmsd analysis revealed that the complex was stable at around 6.7 Å till the completion of the trajectory (Fig. 5*J*). The converged trajectory was used for calculating the binding free energy using the MM-PBSA method, and it was observed to be –32.65 kcal/mol (*SI Appendix, Table S5*). Furthermore, per-residue energy decomposition analysis revealed that Glu57, Glu94, Val98, Glu289, Val290, and Arg674 contributed substantially with energy contributions greater than –1.0 kcal/mol (Fig. 5*K*). Molecular docking studies also revealed that the raloxifene binding site in PPK-1 homologs from *E. coli*, *K. pneumoniae*, and *M. tuberculosis* is similar (*SI Appendix, Fig. S6E–H* and *Table S4*). We observed that raloxifene binds *E. coli* and *K. pneumoniae* PPK-1 with MM-GBSA scores of –96.84 and –61.69 kcal/mol, respectively. Molecular docking of gallein with *M. tuberculosis* PPK-1 revealed that it also binds close to the ATP binding site (*SI Appendix, Fig. S6I*). The residues involved in the binding of gallein with *M. tuberculosis* PPK-1 are shown in (*SI Appendix, Table S4*). In agreement with molecular docking experiments, we observed that mutation of Glu289 to alanine abrogated the ability of raloxifene to inhibit PPK-1 enzymatic activity (Fig. 5*L*). We also observed that the enzymatic activity associated with (His)₆-PPK-1 and (His)₆-PPK-1^{E289A} proteins was comparable to each other (Fig. 5*M*). As reported earlier, (His)₆-PPK-1^{H491A} was inactive in our enzymatic assays (Fig. 5*M*) (59). Taken together, these results suggest that the binding pocket of raloxifene in PPK-1 homologs from various microorganisms is similar and Glu289 residue is important for the interaction of *M. tuberculosis* homolog with raloxifene.

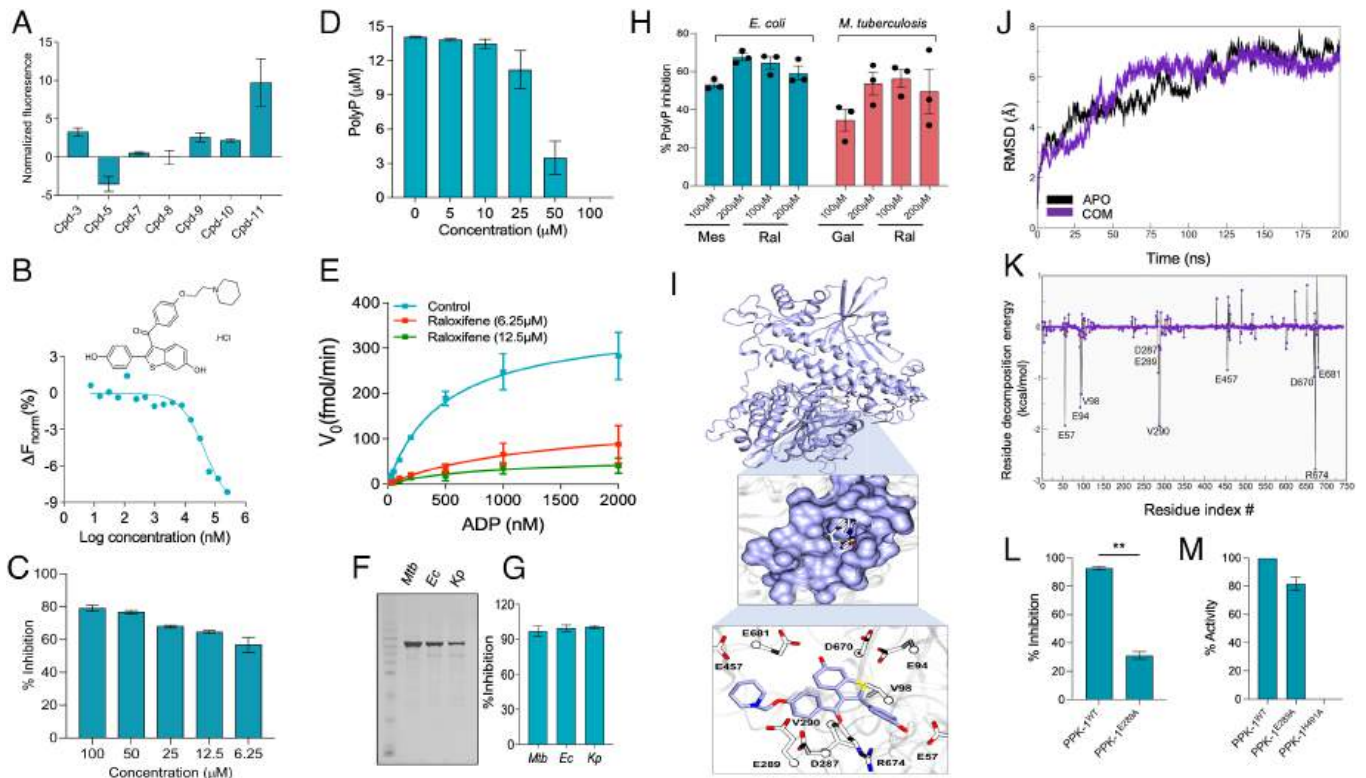


Fig. 5. Target-based screening identifies raloxifene hydrochloride as an inhibitor of PPK-1 from *M. tuberculosis*. (A) Microscale thermophoresis (MST) binding data of (His)₆-PPK-1 with primary hits obtained from preliminary screening assays. The y-axis depicts the normalized fluorescence values, and the x-axis represents compound IDs. The data shown in this panel are mean \pm SE of normalized fluorescence obtained from two independent experiments performed in duplicates. (B) Dose-response curve showing the interaction between *M. tuberculosis* (His)₆-PPK-1 with various concentrations of raloxifene hydrochloride. The data obtained are plotted as response versus concentration and are representative of two independent experiments. The structure of raloxifene hydrochloride is also shown in this panel. (C and D) Dose-dependent inhibition of *M. tuberculosis* PPK-1 enzyme-dependent ATP (C) and PolyP (D) synthesis in the presence of varying raloxifene concentrations was calculated. (E) Michaelis-Menten (MM) plot for *M. tuberculosis* PPK-1 enzyme activity in the absence or presence of raloxifene. (F) SDS-PAGE showing the purified PPK-1 homologs from *M. tuberculosis* (Mtb), *E. coli* (Ec), and *K. pneumoniae* (Kp). (G) Inhibition of ATP synthesis activity of PPK-1 homologs from Mtb, Ec, and Kp in the presence of 100 μ M raloxifene was calculated. The data shown in panels (C), (D), (E), and (G) are mean \pm SE obtained from three independent experiments performed in duplicates. (H) Effect of mesalamine, gallein, and raloxifene on polyP accumulation in *E. coli* or *M. tuberculosis*. The data shown in this panel are mean \pm SE of % polyP inhibition obtained from three independent experiments. (I) This panel depicts the docking of raloxifene on the modeled structure of *M. tuberculosis* PPK-1. In the upper panel, the protein (colored in ice blue and render in the new cartoon) and best conformer of raloxifene (colored atom-wise C: ice blue, O: red, and N: blue, rendered in licorice) is shown. In the middle panel, the residues lining the binding site of raloxifene are shown. In the lower panel, key residues of *M. tuberculosis* PPK-1 that are involved in interaction with raloxifene are shown in licorice: White and their respective C α atoms are shown in Corey Pauling Koltun (CPK) representation. For clarity, only the sidechain and C α of residues are shown. (J and K) Time-wise dynamic stability measurement of raloxifene binding in *M. tuberculosis* PPK-1 protein using molecular dynamics simulations. (J) Rms stability analysis in APO (black) and with complex (purple). (K) Per-residue decomposition of raloxifene interacting residues with PPK-1 homolog from *M. tuberculosis*. (L) Inhibition assay of *M. tuberculosis* PPK-1^{WT} and PPK-1^{E289A} enzyme-dependent ATP synthesis in the presence of 100 μ M raloxifene. (M) Comparison of ATP synthesis activity of PPK-1^{WT}, PPK-1^{E289A}, and PPK-1^{H491A}. The data shown in panels (L) and (M) are mean \pm SE obtained from three independent experiments performed in duplicates. The data obtained were statistically analyzed using the paired-two-tailed *t* test (***P* < 0.01).

Raloxifene Inhibits *M. tuberculosis* Growth in THP-1 Macrophages and Mice.

Since PPK-1 is required for the intracellular survival of *M. tuberculosis* in macrophages, we next investigated the activity of raloxifene alone or in combination with existing TB drugs on *M. tuberculosis* growth inside THP-1 macrophages (8). We observed ~19.4-fold and ~12.0-fold inhibition of *M. tuberculosis* growth in macrophages after exposure to INH and raloxifene, respectively (Fig. 6A). The addition of raloxifene increased the intracellular activity of INH by ~7.0-fold (Fig. 6A). We next determined the effect of raloxifene on the growth of an INH-resistant strain inside macrophages. We observed that exposure to raloxifene inhibited the growth of INH-resistant *M. tuberculosis* strain by ~25.0-fold in macrophages (Fig. 6A). We also observed ~14.0-fold and ~13.5-fold inhibition of *M. tuberculosis* growth inside macrophages after exposure to BDQ or PTM, respectively (Fig. 6B). The addition of raloxifene increased the intracellular activity of BDQ and PTM by ~32.0-fold and ~42.0-fold, respectively (Fig. 6B). In our checkerboard assays, we observed that raloxifene showed additive interactions with either INH or BDQ, or PTM in intracellular

killing assays (SI Appendix, Fig. S7). We observed that the HSA synergy score for the combination of raloxifene with INH, BDQ, and PTM was 6.179, 6.723, and 3.599, respectively (SI Appendix, Fig. S7). We next determined whether oral administration of raloxifene inhibits *M. tuberculosis* growth in vivo. We observed that in comparison to the vehicle-treated group, administration of INH or raloxifene reduced the lung bacillary loads by ~16.0-fold and 3.0-fold, respectively, after 4 wk of treatment (Fig. 6C). In spleens, in comparison to the vehicle-treated group, we observed 197.0-fold and 7.0-fold reduction in bacterial burdens in INH or raloxifene-treated mice, respectively (Fig. 6D). We next performed experiments to determine the effect of oral administration of raloxifene on the intracellular growth of wild-type, Δ ppk-1 mutant, and complemented strain in chronic mice model of infection. As expected, Δ ppk-1 mutant displayed attenuated phenotype in the lung and spleens of mice in comparison to the parental strain at 4 wk post-infection. As reported in guinea pigs, we observed that this growth defect was partially restored in the complemented strain (8) (Fig. 6E). In comparison to the vehicle-treated group,

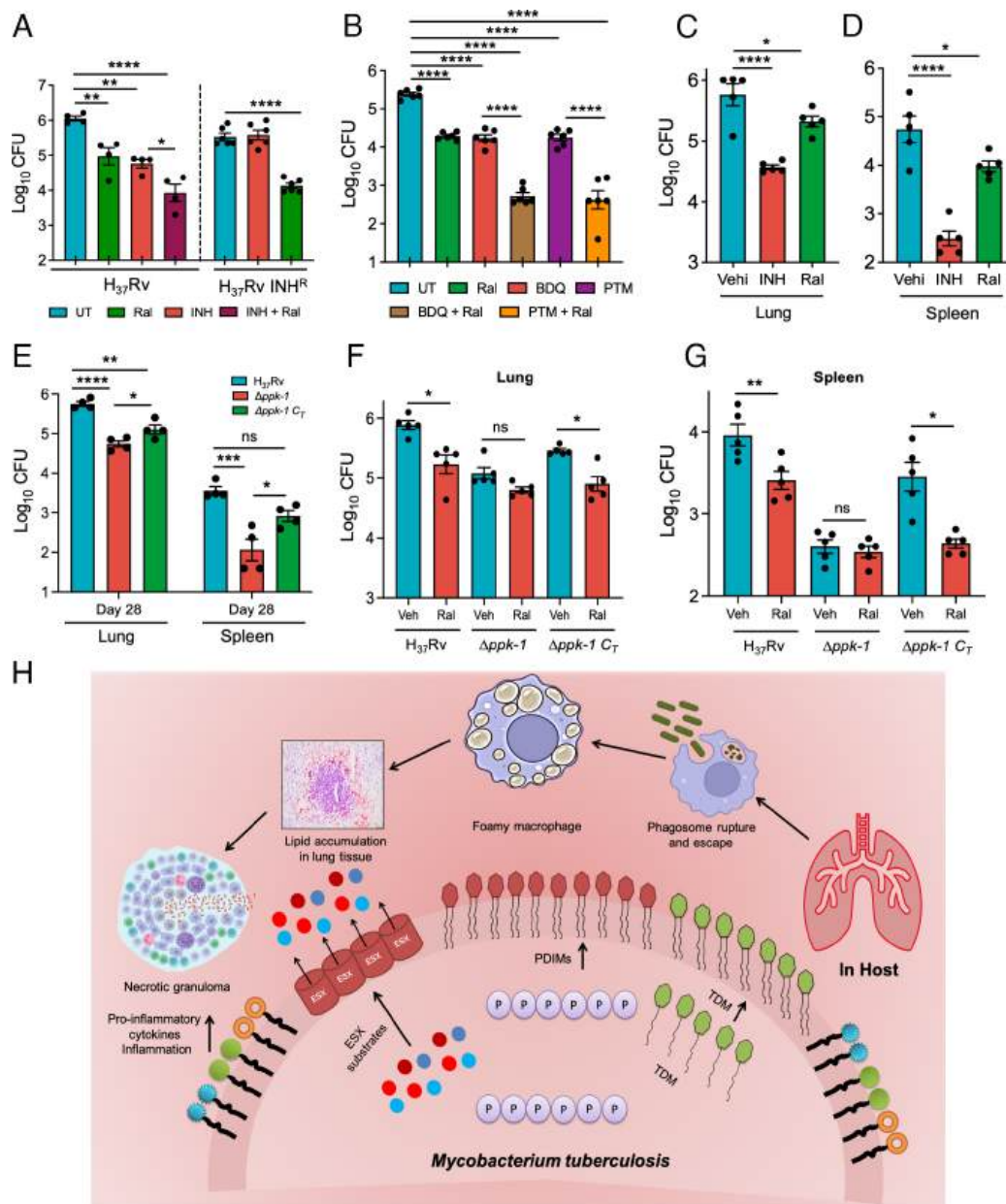


Fig. 6. (A and B) Antimycobacterial activity of raloxifene alone or in combination with known TB drugs in macrophages. The intracellular killing experiment against *M. tuberculosis* was performed. The concentration of drugs used were isoniazid (INH, 10 μ M), raloxifene (Ral, 50 μ M), bedaquiline (BDQ, 10 μ M), and pretomanid (PTM, 10 μ M). The data shown in these panels are mean \pm SE of \log_{10} CFU obtained from two or three independent experiments performed in duplicates. (C and D) Oral administration of raloxifene inhibits the growth of *M. tuberculosis* in mice. Four-week aerosol infected female mice were treated with either 120 mg/kg raloxifene or 10 mg/kg INH for 4 wk. The data shown in these panels are mean \pm SE of \log_{10} CFU in lung (C) or spleens (D) obtained from various groups. (E–G) PPK-1 specific in vivo activity of raloxifene. Six- to eight-week-old female mice were infected with either wild type or $\Delta ppk-1$ mutant or complemented strain via aerosol route for 4 wk. (E) This panel shows lung and splenic bacillary load in mice infected with wild type or $\Delta ppk-1$ mutant or complemented strain. (F and G) The bacterial burdens were determined in the lungs and spleens of vehicle and raloxifene-treated mice infected with indicated groups at 4 wk post-treatment. The data obtained were statistically analyzed by one-way ANOVA [panels (A–E), * P < 0.05, ** P < 0.01, *** P < 0.001, **** P < 0.0001] or paired two-tailed t test [panels (F and G), * P < 0.05, ** P < 0.01]. (H) Deletion of *ppk-1* from *M. tuberculosis* affects the expression of bacterial and host metabolic pathways implicated in disease pathogenesis. *M. tuberculosis* virulence factors such as PDIMs and ESX-1 induce phagosome rupture and escape, and promote bacterial pathogenesis in host tissues. These virulence factors and TMM and TDM trigger lipid-laden foamy macrophage formation. These foamy macrophages provide a favorable environment and support bacterial nutrition and persistence. *M. tuberculosis* infection induces the secretion of various pro-inflammatory cytokines, which contribute to tissue damage, inflammation, and disease progression. In the present study, we show reduced levels of various virulence-associated factors such as PDIMs, TMM, and TDM in mid-log phase cultures of the $\Delta ppk-1$ mutant strain. The reduced levels of these virulence factors are most likely to be associated with i) increased phagosome-lysosome fusion in macrophages, ii) reduced Type-I IFN signaling, inflammation, and formation of foamy macrophages and iii) faster clearance of $\Delta ppk-1$ mutant strain from host tissues. Panel (H) was generated using BioRender.

the lung bacillary loads were reduced by ~ 4.5 -folds and ~ 3.5 -folds, respectively, in raloxifene-treated wild-type and complemented strain-infected mice at 4 wk post-treatment (Fig. 6F). Similarly, the splenic bacillary load was decreased by ~ 3.5 -folds and ~ 6.5 -folds, respectively, in raloxifene-treated wild-type and complemented

infected mice, in comparison to vehicle-treated group (Fig. 6G). However, no differences were observed in lungs and splenic bacterial loads in vehicle-treated and raloxifene-treated $\Delta ppk-1$ mutant-infected mice at 4 wk post-treatment (Fig. 6F and G). Overall, these findings show that raloxifene enhanced the activity

of known TB drugs and also inhibited the growth of *M. tuberculosis* in macrophages and mice by targeting PPK-1.

Discussion

Previous studies have reported that polyP homeostasis influences *M. tuberculosis* pathogenesis and susceptibility to current TB drugs (8, 10, 13, 14, 16, 29). However, the regulation of *M. tuberculosis* pathogenesis by PolyP deficiency is still unclear. In the present study, we have identified several polyP interacting proteins. Many of these interacting proteins require ATP for cellular functions, which raises the possibility that polyP can substitute ATP for their enzymatic activity. We show that polyP interacts with AccA1 and AccD1 proteins from *M. tuberculosis*. This interaction was specific for long-chain polyP as no interaction was observed with short-chain polyP. Studies have shown that AccA1-AccD1 forms a multisubunit complex and is involved in the leucine degradation pathway (60). These enzymes catalyze the carboxylation of acetyl-CoA to malonyl-CoA, a precursor for fatty-acid biosynthesis (61). We speculate that polyP levels might regulate the activity of the AccA1-AccD1 enzyme complex and contribute to lipid biosynthesis in *M. tuberculosis*. Previously, it has been shown that polyP forms a complex with Lon protease and promotes degradation of ribosomal proteins during amino acid starvation (62). Interestingly, ClpP2 was also identified as a polyP interacting protein from late-log phase cultures of *M. tuberculosis*. It has been shown that various *M. tuberculosis* antitoxins belonging to TA systems are Clp protease substrates. The degradation of these antitoxins by cellular protease might result in derepression of the TA operon and toxin activation (63). Therefore, we hypothesize that polyP might regulate ClpP2-mediated degradation of antitoxins, eventually leading to differential expression of TA systems, including *vapBC15*, in the $\Delta ppk-1$ mutant strain. DnaK, a chaperone protein involved in protein folding, the RNA polymerase subunits RpoB and RpoC and transcription terminator Rho were also identified as polyP interacting proteins from late-log phase cultures of *M. tuberculosis*. These observations suggest that polyP might regulate the rates of translation and transcription in *M. tuberculosis*, as reported for *E. coli* (64).

Previously, it has been shown that phosphoglucokinase from *M. tuberculosis* prefers polyP as a phosphoryl donor for conversion of glucose to glucose-6-phosphate (26, 27). As expected, the $\Delta ppk-1$ mutant strain displayed a growth defect in the 7H9 medium containing glucose as the carbon source. Glucose-6-phosphate is a key intermediate in central carbon metabolism and acts as a precursor for trehalose biosynthesis. In agreement, the levels of glucose-6-phosphate, intermediates belonging to the TCA cycle, trehalose metabolism, and amino acids were significantly reduced in the $\Delta ppk-1$ mutant strain relative to the parental strain in the glucose-containing medium. Also, the mutant strain had lower levels of virulence-associated lipids such as PDIMs, TDM, and TMM relative to the parental and complemented strains. In agreement with the reduced levels of PDIMs, we observed increased phagosome-lysosome fusion in macrophages and decreased Type I IFN signaling in lung tissues of mice upon infection with the $\Delta ppk-1$ mutant strain relative to the wild-type strain. We also observed reduced expression of transcripts encoding for proteins involved in calcium signaling and cell death in the lungs of animals infected with the $\Delta ppk-1$ mutant strain. It has been reported that the host limits the access of trace metal ions such as Fe^{2+} , Zn^{2+} , and Cu^{2+} to intracellular pathogens, which thwarts microbial growth (65). Recently, it has been shown that *M. tuberculosis* produces zinc-scavenging molecules kupyaphores, and these are essential to establish infection in mice (41). We observed reduced transcript levels of various zinc finger proteins in lung tissues of mice infected with the $\Delta ppk-1$ mutant strain, suggesting a zinc-limiting environment. It has

also been shown that *M. tuberculosis* deploys the ESX-3 system to maintain zinc and iron homeostasis (66, 67). In agreement, we observed the reduced transcript levels of *eccD3*, a component of the ESX-3 secretion system, in mid-log phase cultures of the $\Delta ppk-1$ mutant strain.

Several studies have shown that *M. tuberculosis* infected macrophages in granulomas accumulate lipid droplets and differentiate into foamy macrophages. Foamy macrophages represent a favorable niche for the intracellular multiplication and dissemination of *M. tuberculosis* (50, 68). In agreement with the reduced levels of PDIMs, TMM, and TDM, we observed that transcript levels of markers associated with the formation of foamy macrophages were reduced in animals infected with the $\Delta ppk-1$ mutant strain. Reduced neutral lipid content in THP-1 macrophages and lung tissues of $\Delta ppk-1$ infected guinea pigs substantiates our RNA-seq data. It has also been shown that strains harboring deletions in proteins involved in mycolic acid biosynthesis or the ESX-1 secretion system generate a weaker T_H1 immune response upon infection (69, 70). As expected, the levels of various inflammatory cytokines and chemokines were significantly reduced in mutant strain-infected mice relative to wild type strain-infected mice. This reduced expression of host inflammatory markers in the lungs of $\Delta ppk-1$ mutant infected animals could be attributed to decreased bacterial burdens and alteration of host-pathogen interactions resulting from polyP deficiency. In support of the latter, it has been reported that *M. smegmatis* and *M. tuberculosis* secrete polyP and inhibit phagosome acidification and phagosome-lysosome fusion (11). In addition, it has also been demonstrated that polyP exacerbates LPS-mediated inflammatory response in macrophages and mice (71).

Using target-based screening, we have identified raloxifene as an inhibitor of PPK-1 homolog from *M. tuberculosis*. Raloxifene is a selective estrogen receptor modulator and is being used in the treatment of osteoporosis and invasive breast cancer (72). Several studies have identified small molecules such as gallicin and mesalamine that inhibit PPK-1 homologs from *E. coli* *P. aeruginosa* or *V. cholerae* (51, 57). We show that gallicin also inhibited the activity of PPK-1 homolog from *M. tuberculosis*, however, no inhibition was observed in the presence of mesalamine. In agreement, the levels of intracellular polyP were decreased upon exposure of *M. tuberculosis* to raloxifene or gallicin in vitro. We also observed that raloxifene inhibited the activity of PPK-1 homologs from *E. coli* and *K. pneumoniae*. Also, the binding patterns of raloxifene with PPK-1 homologs of *E. coli*, *K. pneumoniae*, and *M. tuberculosis* were similar. Computational studies revealed that in APO protein, Glu289 is involved in the formation of an intra-hydrogen bond network with Arg310 and Phe462, and this network is destabilized by the binding of raloxifene. In agreement, the mutation of Glu289 to alanine reduced the ability of raloxifene to inhibit the *M. tuberculosis* PPK-1 enzyme. Previously, we have shown that polyP deficiency results in attenuation and enhanced susceptibility of *M. tuberculosis* against INH (8). In agreement, the *M. tuberculosis* strain deficient in the stringent response ($\Delta relA$, with reduced polyP levels) is also more susceptible to INH during the chronic phase of infection in mice lung tissues (73). Also, several studies have shown that polyP accumulating *M. tuberculosis* strains are tolerant to INH-mediated killing (13, 14). In agreement with our earlier observations, we observed that raloxifene was able to inhibit *M. tuberculosis* growth in macrophages, mice and also enhance INH, BDQ, and PTM intracellular activity. We observed that raloxifene also inhibited the growth of INH resistant *M. tuberculosis* strain in THP-1 macrophages. These observations suggest that inhibitors of stringent response pathway (PPK-1/RelA) in combination with existing

drugs may shorten the duration of chemotherapy. Identification of PPK1-specific inhibitors, in addition to small molecules such as BDQ and Q-203, would further validate the processes of ATP synthesis as targets for TB drug discovery (74, 75).

This detailed study delineates the mechanisms by which polyP contributes to pathogenesis and identifies small molecule inhibitors against the PPK-1 enzyme from *M. tuberculosis*. We demonstrate that deletion of *ppk-1* affects the expression of virulence-associated genes, lipid biosynthesis, and utilization of glucose as the carbon source in *M. tuberculosis*. The decreased levels of these lipid molecules might result in increased phagolysosome fusion with reduced necrosis and dissemination to the cytosol, reduced formation of foamy macrophages, metal ion deficient environment in granulomas, minimal inflammatory, and T_H1 response in mice (Fig. 6H). The identified small molecules may be combined with current TB drugs to eradicate both drug-susceptible and drug-resistant populations in different metabolic states. Future experiments would be performed to delineate the exact mechanisms for the observed reduced expression of inflammatory markers in the lungs of $\Delta ppk-1$ infected mice. Since polyP accumulation has been reported in *M. tuberculosis* at later stages of growth, we would also perform experiments to compare the transcriptional profiles of parental, polyP deficient and accumulating strains in these conditions (10). Since PPK-1 is a highly conserved enzyme, the identified PPK-1-specific inhibitors may possess broad-spectrum in vivo activity.

Materials and Methods

The detailed description of all protocols used in the study is provided in [SI Appendix, Materials and Methods](#).

Bacterial Strains, Culture Conditions, and Plasmids. Details are in [SI Appendix](#). The bacterial strains and plasmids used in the study are listed in [SI Appendix, Table S6](#).

Pull-Down Assays. In order to identify polyP₇₀₀ interacting proteins, pull-down assays were performed using clarified lysates prepared from mid-log or late-log phase cultures of *M. tuberculosis*.

Cloning, Expression, and Protein Purification. In order to purify recombinant proteins, various wild-type genes or their mutant derivatives were PCR amplified and cloned into pET28b.

Bacterial RNA-Seq Experiments. Total RNA was isolated from mid-log phase cultures of various strains and shipped to AgriGenome Labs Pvt. Ltd. for sequencing on an Illumina HiSeq platform.

Metabolomics Experiments. Total metabolites were extracted from various strains grown in 7H9 (wild-type, $\Delta ppk-1$, and $\Delta kppx$) and glucose medium (wild-type and $\Delta ppk-1$) for 7 d. The mass-spectrometric data were collected in both positive and negative mode at 1,20,000 resolutions in MS1 mode and 30,000 resolution in data-dependent MS2 scan mode using an Orbitrap fusion tribrid mass spectrometer equipped with a heated electrospray ionization (HESI) source.

Lipid Extraction and Thin Layer Chromatography. Apolar lipid fraction, TMM, and TDM were isolated from mid-log phase cultures of various *M. tuberculosis* strains.

Target-Based Screening Assays. For target-based screening experiments, recombinant *M. tuberculosis* PPK-1 protein was purified, and activity assays were performed. PPK-1 reverse enzymatic reaction was performed in 50 mM Tris-Cl- pH-7.4, 40 mM (NH₄)₂SO₄, 4 μ M MgCl₂, 100 nM ADP, and 300 nM (His)₆-PPK-1 enzyme. All reaction plates included buffer-only, enzyme-only, and substrate-only control.

PPK-1-Dependent polyP Synthesis Assays. The PPK-1-dependent forward enzymatic reaction was performed as previously described (57).

Quantification of Intracellular polyP Levels in *E. coli* and *M. tuberculosis*. Intracellular polyP was extracted from *E. coli*, and *M. tuberculosis* after exposure to various drugs was extracted as per standard protocols. The quantification of polyP was performed using the toluidine blue method.

Bio-Layer Interferometry and Microscale Thermophoresis Experiments. The protein-small molecule interactions were performed using BLI and MST.

Macrophage Experiments. THP-1 macrophages were infected with *M. tuberculosis* at a multiplicity of infection of 1:10. The infected macrophages were subsequently treated with various drugs, and CFU enumeration or luciferase measurements were performed after 4 d.

Molecular Docking and Dynamics Studies. Schrodinger-2017 was used for all docking-related experiments. Molecular dynamics (MD) simulations were performed using the Antechamber module of AmberTools, and protein parameters were assigned using the AMBER ff14SB force field.

Mice Virulence and Efficacy Experiments. For virulence studies, 6- to 8-wk-old female Balb/c mice were infected with various strains via aerosol route. For efficacy experiments, *M. tuberculosis*-infected mice were orally administered with INH or raloxifene for 6 d a week for 28 d. The bacterial loads were determined in the lungs and spleens at designated time points as per standard protocols.

Host RNA-Seq and Cytokine Measurement Experiments. For host transcriptional analysis, total RNA was isolated from lung tissues of uninfected or mice infected with wild-type or $\Delta ppk-1$ mutant strain at 4 wk post-infection. The samples were shipped to Bionivid Technology Private Ltd. for RNA sequencing. The levels of cytokines in lung homogenates were determined by ELISA.

Nile Red Staining. For Nile red staining, infected macrophages were fixed with 4% paraformaldehyde and stained with Nile red.

Hematoxylin and Oil Red O Staining of Lung Sections of Infected Guinea Pigs. The lungs from 4-wk infected guinea pigs were fixed in 4% formalin and stained with hematoxylin and Oil Red O solution.

Statistical Analysis. GraphPad Prism version 8 (GraphPad Software Inc.) was used for statistical analysis and the generation of graphs. The data were considered significant at $P < 0.05$. The statistical test used is mentioned in the respective figure legends.

Data, Materials, and Software Availability. The RNA-seq data reported in this article has been obtained from mid-log phase cultures of *Mycobacterium tuberculosis* strains or lung tissues of uninfected and infected *Mus musculus*. The raw data sequence files have been deposited in the repository of the National Center for Biotechnology Information and can be accessed using BioProject [PRJNA892734](#) (*M. tuberculosis*) (76) and [PRJNA892458](#) (*Mus musculus*) (77).

ACKNOWLEDGMENTS. We are thankful to the technical staff of IDRF and, SAF, THSTI, for their assistance during BSL-3 and animal experiments. S.C. and M.S. acknowledge the Council of Scientific and Industrial Research and the Department of Biotechnology, respectively, for their research fellowship. P.S. acknowledges the Department of Science and Technology for his fellowship (PDF/2018/002454). We sincerely thank Dr. Bill Jacobs (Albert Einstein College of Medicine, United States) for providing the INH-resistant strain of *M. tuberculosis*. The plasmid pMV306hsp+LuxG13 was a gift from Brian Robertson & Siouxsie Wiles (Addgene plasmid # 26161; <http://n2t.net/addgene:26161>; RRID:Addgene_26161). Mr. Amit (Institute of Liver and Biliary Science, India) is greatly acknowledged for oil red O staining of guinea lung sections. The authors sincerely thank Dr. Bhisma Panda (THSTI) for acquiring images of oil-red O-stained guinea lung sections. R.S. acknowledges the financial support from the Indian Council of Medical Research (5/8/5/21/2019/ECD-1) and Wellcome Trust-DBT India Alliance (IA/S/19/2/504646). S.A. acknowledge the funding received from Department of Biotechnology, India through Translational Research Program (BT/PR30159/MED/15/188/2018). The funders had no role in study design, results analysis and manuscript preparation.

Author affiliations: ^aTranslational Health Science and Technology Institute, National Capital Region Biotech Science Cluster, Faridabad 121001, India; and ^bInstitut Pasteur de Tunis, Laboratory of Transmission, Control and Immunobiology of Infections, LR11 IPT02, Tunis 1002, Tunisia

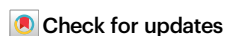
1. K. Ahn, A. Kornberg, Polyphosphate kinase from. Purification and demonstration of a phosphoenzyme intermediate. *J. Biol. Chem.* **265**, 11734–11739 (1990).
2. H. Zhang, K. Ishige, A. Kornberg, A polyphosphate kinase (PPK2) widely conserved in bacteria. *Proc. Natl. Acad. Sci. U.S.A.* **99**, 16678–16683 (2002).
3. K. Ishige, H. Zhang, A. Kornberg, Polyphosphate kinase (PPK2), a potent, polyphosphate-driven generator of GTP. *Proc. Natl. Acad. Sci. U.S.A.* **99**, 16684–16688 (2002).
4. B. Nocek *et al.*, Polyphosphate-dependent synthesis of ATP and ADP by the family-2 polyphosphate kinases in bacteria. *Proc. Natl. Acad. Sci. U.S.A.* **105**, 17730–17735 (2008).
5. K. Sureka, S. Sanyal, J. Basu, M. Kundu, Polyphosphate kinase 2: A modulator of nucleoside diphosphate kinase activity in mycobacteria. *Mol. Microbiol.* **74**, 1187–1197 (2009).
6. K. D. Kumble, A. Kornberg, Endopolyphosphatases for long chain inorganic polyphosphate in yeast and mammals. *J. Biol. Chem.* **271**, 27146–27151 (1996).
7. A. Sethuraman, N. N. Rao, A. Kornberg, The endopolyphosphate gene: Essential in. *Proc. Natl. Acad. Sci. U.S.A.* **98**, 8542–8547 (2001).
8. R. Singh *et al.*, Polyphosphate deficiency in is associated with enhanced drug susceptibility and impaired growth in guinea pigs. *J. Bacteriol.* **195**, 2839–2851 (2013).
9. K. Sureka *et al.*, Polyphosphate kinase is involved in stress-induced mprAB-sigE-rel signalling in mycobacteria. *Mol. Microbiol.* **65**, 261–276 (2007).
10. Y. M. Chuang *et al.*, Deficiency of the novel exopolyphosphatase Rv1026/PPX2 leads to metabolic downshift and altered cell wall permeability in. *mBio* **6**, e02428 (2015).
11. R. Rijal, L. A. Cadena, M. R. Smith, J. F. Carr, R. H. Gomer, Polyphosphate is an extracellular signal that can facilitate bacterial survival in eukaryotic cells. *Proc. Natl. Acad. Sci. U.S.A.* **117**, 31923–31934 (2020).
12. S. T. Cole *et al.*, Deciphering the biology of from the complete genome sequence. *Nature* **393**, 537–544 (1998).
13. Y. M. Chuang, D. A. Belchis, P. C. Karakousis, The polyphosphate kinase gene *ppk2* is required for inorganic polyphosphate regulation and virulence. *mBio* **4**, e00039–00013 (2013).
14. M. Singh *et al.*, Establishing virulence associated polyphosphate kinase 2 as a drug target for *Mycobacterium tuberculosis*. *Sci. Rep.* **6**, 26900 (2016).
15. M. Y. Choi *et al.*, The two PPX-GppA homologues from *Mycobacterium tuberculosis* have distinct biochemical activities. *PLoS One* **7**, e42561 (2012).
16. P. Tiwari *et al.*, Exopolyphosphatases PPK1 and PPK2 from *Mycobacterium tuberculosis* regulate dormancy response and pathogenesis. *Microb. Pathog.* **173**, 105885 (2022).
17. Z. Wang *et al.*, RbpA and sigma(B) association regulates polyphosphate levels to modulate mycobacterial isoniazid-tolerance. *Mol. Microbiol.* **108**, 627–640 (2018).
18. L. Tong, Structure and function of biotin-dependent carboxylases. *Cell Mol. Life Sci.* **70**, 863–891 (2013).
19. J. E. Cronan Jr., G. L. Waldrop, Multi-subunit acetyl-CoA carboxylases. *Prog. Lipid. Res.* **41**, 407–435 (2002).
20. M. Szymona, J. Widomski, A kinetic study on inorganic polyphosphate glucokinase from *Mycobacterium tuberculosis* H37Ra. *Physiol. Chem. Phys.* **6**, 393–404 (1974).
21. P. C. Hsieh, T. H. Kowalczyk, N. F. Phillips, Kinetic mechanisms of polyphosphate glucokinase from *Mycobacterium tuberculosis*. *Biochemistry* **35**, 9772–9781 (1996).
22. T. Shiba *et al.*, Inorganic polyphosphate and the induction of *rpoS* expression. *Proc. Natl. Acad. Sci. U.S.A.* **94**, 11210–11215 (1997).
23. H. I. Boshoff *et al.*, The transcriptional responses of *Mycobacterium tuberculosis* to inhibitors of metabolism: Novel insights into drug mechanisms of action. *J. Biol. Chem.* **279**, 40174–40184 (2004).
24. J. Augenstein *et al.*, ESX-1 and phthiocerol dimycocerosates of *Mycobacterium tuberculosis* act in concert to cause phagosomal rupture and host cell apoptosis. *Cell Microbiol.* **19**, e12726 (2017).
25. A. K. Barczak *et al.*, Systematic, multiparametric analysis of *Mycobacterium tuberculosis* intracellular infection offers insight into coordinated virulence. *PLoS Pathog.* **13**, e1006363 (2017).
26. P. C. Hsieh, B. C. Shenoy, F. C. Haase, J. E. Jentoft, N. F. Phillips, Involvement of tryptophan(s) at the active site of polyphosphate/ATP glucokinase from *Mycobacterium tuberculosis*. *Biochemistry* **32**, 6243–6249 (1993).
27. P. C. Hsieh, B. C. Shenoy, J. E. Jentoft, N. F. Phillips, Purification of polyphosphate and ATP glucose phosphotransferase from *Mycobacterium tuberculosis* H37Ra: Evidence that poly(P) and ATP glucokinase activities are catalyzed by the same enzyme. *Protein Expr. Purif.* **4**, 76–84 (1993).
28. H. E. Umberger, Amino acid biosynthesis and its regulation. *Annu. Rev. Biochem.* **47**, 532–606 (1978).
29. Y. M. Chuang *et al.*, Stringent response factors PPK1 and PPK2 play an important role in *Mycobacterium tuberculosis* metabolism, biofilm formation, and sensitivity to isoniazid in vivo. *Antimicrob. Agents Chemother.* **60**, 6460–6470 (2016).
30. H. N. Murphy *et al.*, The OtsAB pathway is essential for trehalose biosynthesis in *Mycobacterium tuberculosis*. *J. Biol. Chem.* **280**, 14524–14529 (2005).
31. M. A. Ballicora, A. A. Iglesias, J. Preiss, ADP-glucose pyrophosphorylase, a regulatory enzyme for bacterial glycogen synthesis. *Microbiol. Mol. Biol. Rev.* **67**, 213–225, table of contents (2003).
32. S. Bornemann, alpha-Glucan biosynthesis and the GlgE pathway in *Mycobacterium tuberculosis*. *Biochem. Soc. Trans.* **44**, 68–73 (2016).
33. K. A. L. De Smet, A. Weston, I. N. Brown, D. B. Young, B. D. Robertson, Three pathways for trehalose biosynthesis in mycobacteria. *Microbiology (Reading)* **146**, 199–208 (2000).
34. C. M. Goins, S. Dajnowicz, M. D. Smith, J. M. Parks, D. R. Ronning, Mycolyltransferase from *Mycobacterium tuberculosis* in covalent complex with tetrahydrolipstatin provides insights into antigen 85 catalysis. *J. Biol. Chem.* **293**, 3651–3662 (2018).
35. K. Takayama, C. Wang, G. S. Besra, Pathway to synthesis and processing of mycolic acids in *Mycobacterium tuberculosis*. *Clin. Microbiol. Rev.* **18**, 81–101 (2005).
36. P. Chandra, S. J. Grigsby, J. A. Phillips, Immune evasion and provocation by *Mycobacterium tuberculosis*. *Nat. Rev. Microbiol.* **20**, 750–766 (2022), 10.1038/s41579-022-00763-4.
37. F. McNab, K. Mayer-Barber, A. Sher, A. Wack, A. O'Garra, Type I interferons in infectious disease. *Nat. Rev. Immunol.* **15**, 87–103 (2015).
38. S. Orrenius, B. Zhivotovsky, P. Nicotera, Regulation of cell death: The calcium-apoptosis link. *Nat. Rev. Mol. Cell Biol.* **4**, 552–565 (2003).
39. N. Festjens, T. Vanden Berghe, P. Vandenabeele, Necrosis, a well-orchestrated form of cell demise: Signalling cascades, important mediators and concomitant immune response. *Biochim. Biophys. Acta* **1757**, 1371–1387 (2006).
40. D. Corbett *et al.*, Two zinc uptake systems contribute to the full virulence of *Listeria monocytogenes* during growth in vitro and in vivo. *Infect. Immun.* **80**, 14–21 (2012).
41. K. Mehdiratta *et al.*, Kupyaphores are zinc homeostatic metallophores required for colonization of *Mycobacterium tuberculosis*. *Proc. Natl. Acad. Sci. U.S.A.* **119**, e2110293119 (2022).
42. C. J. Cambier, S. M. O'Leary, M. P. O'Sullivan, J. Keane, L. Ramakrishnan, Phenolic glycolipid facilitates mycobacterial escape from microbicidal tissue-resident macrophages. *Immunity* **47**, 552–565.e554 (2017).
43. E. Kugelberg, Immune evasion: Mycobacteria hide from TLRs. *Nat. Rev. Immunol.* **14**, 62–63 (2014).
44. F. Abebe, M. Belay, M. Legesse, A. Mihret, K. S. Franken, Association of ESAT-6/CFP-10-induced IFN-gamma, TNF-alpha and IL-10 with clinical tuberculosis: Evidence from cohorts of pulmonary tuberculosis patients, household contacts and community controls in an endemic setting. *Clin. Exp. Immunol.* **189**, 241–249 (2017).
45. V. Guerini *et al.*, Storage lipid studies in tuberculosis reveal that foam cell biogenesis is disease-specific. *PLoS Pathog.* **14**, e1007223 (2018).
46. D. Shim, H. Kim, S. J. Shin, *Mycobacterium tuberculosis* infection-driven foamy macrophages and their implications in tuberculosis control as targets for host-directed therapy. *Front. Immunol.* **11**, 910 (2020).
47. J. E. Griffin *et al.*, Cholesterol catabolism by *Mycobacterium tuberculosis* requires transcriptional and metabolic adaptations. *Chem. Biol.* **19**, 218–227 (2012).
48. N. Jaisinghani *et al.*, Necrosis driven triglyceride synthesis primes macrophages for inflammation during *Mycobacterium tuberculosis* infection. *Front. Immunol.* **9**, 1490 (2018).
49. M. Knight, J. Braverman, K. Asfaha, K. Gronert, S. Stanley, Lipid droplet formation in *Mycobacterium tuberculosis* infected macrophages requires IFN-gamma/HIF-1alpha signaling and supports host defense. *PLoS Pathog.* **14**, e1006874 (2018).
50. D. G. Russell, P. J. Cardona, M. J. Kim, S. Allain, F. Altare, Foamy macrophages and the progression of the human tuberculosis granuloma. *Nat. Immunol.* **10**, 943–948 (2009).
51. M. Q. Bowlin, M. J. Gray, Inorganic polyphosphate in host and microbe biology. *Trends Microbiol.* **29**, 1013–1023 (2021).
52. N. N. Rao, A. Kornberg, Inorganic polyphosphate supports resistance and survival of stationary-phase *Escherichia coli*. *J. Bacteriol.* **178**, 1394–1400 (1996).
53. M. J. Advani, I. Siddiqui, P. Sharma, H. Reddy, Activity of trifluoperazine against replicating, non-replicating and drug resistant *M. tuberculosis*. *PLoS One* **7**, e44245 (2012).
54. A. J. Warman *et al.*, Antitubercular pharmacodynamics of phenothiazines. *J. Antimicrob. Chemother.* **68**, 869–880 (2013).
55. H. Shubin, J. Sherson, E. Pennes, A. Glaskin, A. Sokmensuer, Prochlorperazine (compazine) as an aid in the treatment of pulmonary tuberculosis. *Antibiotic Med. Clin. Ther. (New York)* **5**, 305–309 (1958).
56. M. R. Brown, A. Kornberg, The long and short of it - polyphosphate, PPK and bacterial survival. *Trends Biochem. Sci.* **33**, 284–290 (2008).
57. N. Neville *et al.*, A dual-specificity inhibitor targets polyphosphate kinase 1 and 2 enzymes to attenuate virulence of *Pseudomonas aeruginosa*. *mBio* **12**, e0059221 (2021).
58. J. U. Dahl *et al.*, The anti-inflammatory drug mesalazine targets bacterial polyphosphate accumulation. *Nat. Microbiol.* **2**, 16267 (2017).
59. P. Mittal, S. Karthikeyan, P. K. Chakraborti, Amino acids involved in polyphosphate synthesis and its mobilization are distinct in polyphosphate kinase-1 from *Mycobacterium tuberculosis*. *PLoS One* **6**, e27398 (2011).
60. M. T. Ehebauer *et al.*, Characterization of the mycobacterial acyl-CoA carboxylase holo complexes reveals their functional expansion into amino acid catabolism. *PLoS Pathog.* **11**, e1004623 (2015).
61. R. Gande *et al.*, Acyl-CoA carboxylases (accD2 and accD3), together with a unique polyketide synthase (Cg-pks), are key to mycolic acid biosynthesis in *Corynebacterium* species such as *Corynebacterium glutamicum* and *Mycobacterium tuberculosis*. *J. Biol. Chem.* **279**, 44847–44857 (2004).
62. A. Kuroda *et al.*, Role of inorganic polyphosphate in promoting ribosomal protein degradation by the Lon protease in *E. coli*. *Science* **293**, 705–708 (2001).
63. P. Bordes, P. Genevieux, Control of toxin-antitoxin systems by proteases in *Mycobacterium tuberculosis*. *Front. Mol. Biosci.* **8**, 691399 (2021).
64. M. J. Gray *et al.*, Polyphosphate is a primordial chaperone. *Mol. Cell* **53**, 689–699 (2014).
65. M. I. Hood, E. P. Skaar, Nutritional immunity: Transition metals at the pathogen-host interface. *Nat. Rev. Microbiol.* **10**, 525–537 (2012).
66. M. S. Siegrist *et al.*, Mycobacterial *Esx-3* is required for mycobactin-mediated iron acquisition. *Proc. Natl. Acad. Sci. U.S.A.* **106**, 18792–18797 (2009).
67. A. Serafini, F. Boldrin, G. Palu, R. Manganello, Characterization of a *Mycobacterium tuberculosis* ESX-3 conditional mutant: Essentiality and rescue by iron and zinc. *J. Bacteriol.* **191**, 6340–6344 (2009).
68. P. Peyron *et al.*, Foamy macrophages from tuberculous patients' granulomas constitute a nutrient-rich reservoir for *M. tuberculosis* persistence. *PLoS Pathog.* **4**, e1000204 (2008).
69. H. S. Clemmensen *et al.*, An attenuated *Mycobacterium tuberculosis* clinical strain with a defect in ESX-1 secretion induces minimal host immune responses and pathology. *Sci. Rep.* **7**, 46666 (2017).
70. V. Rao, N. Fujiwara, S. A. Porcelli, M. S. Glickman, *Mycobacterium tuberculosis* controls host innate immune activation through cyclopropane modification of a glycolipid effector molecule. *J. Exp. Med.* **201**, 535–543 (2005).
71. T. Ito *et al.*, Inorganic polyphosphate potentiates lipopolysaccharide-induced macrophage inflammatory response. *J. Biol. Chem.* **295**, 4014–4023 (2020).
72. W. L. Lee, H. T. Chao, M. H. Cheng, P. H. Wang, Rationale for using raloxifene to prevent both osteoporosis and breast cancer in postmenopausal women. *Maturitas* **60**, 92–107 (2008).
73. N. K. Dutta *et al.*, Inhibiting the stringent response blocks *Mycobacterium tuberculosis* entry into quiescence and reduces persistence. *Sci. Adv.* **5**, eaav2104 (2019).
74. K. Pethe *et al.*, Discovery of Q203, a potent clinical candidate for the treatment of tuberculosis. *Nat. Med.* **19**, 1157–1160 (2013).
75. K. Andries *et al.*, A diarylquinoline drug active on the ATP synthase of *Mycobacterium tuberculosis*. *Science* **307**, 223–227 (2005).
76. Chugh *et al.*, RNA sequencing analysis of total RNA isolated from mid-log phase cultures of wild type and $\Delta ppk1$ mutant strain of *Mycobacterium tuberculosis* H37Rv. NCBI. <https://www.ncbi.nlm.nih.gov/bioproject/PRJNA892734>. Deposited 21 October 2021.
77. Chugh *et al.*, Host RNA-seq analysis of mRNA isolated from naive and mice infected with either wild type or $\Delta ppk1$ mutant strain at 28 days post-infection. NCBI. <https://www.ncbi.nlm.nih.gov/bioproject/PRJNA892458>. Deposited 20 October 2021.

Mycobacterium tuberculosis strain with deletions in *menT3* and *menT4* is attenuated and confers protection in mice and guinea pigs

Received: 6 August 2023

Accepted: 29 May 2024

Published online: 27 June 2024



Tannu Priya Gosain¹, Saurabh Chugh¹, Zaigham Abbas Rizvi²,
Neeraj Kumar Chauhan¹, Saqib Kidwai¹, Krishan Gopal Thakur³, Amit Awasthi² &
Ramandeep Singh¹✉

The genome of *Mycobacterium tuberculosis* encodes for a large repertoire of toxin-antitoxin systems. In the present study, MenT3 and MenT4 toxins belonging to MenAT subfamily of TA systems have been functionally characterized. We demonstrate that ectopic expression of these toxins inhibits bacterial growth and this is rescued upon co-expression of their cognate antitoxins. Here, we show that simultaneous deletion of *menT3* and *menT4* results in enhanced susceptibility of *M. tuberculosis* upon exposure to oxidative stress and attenuated growth in guinea pigs and mice. We observed reduced expression of transcripts encoding for proteins that are essential or required for intracellular growth in mid-log phase cultures of $\Delta menT4\Delta T3$ compared to parental strain. Further, the transcript levels of proteins involved in efficient bacterial clearance were increased in lung tissues of $\Delta menT4\Delta T3$ infected mice relative to parental strain infected mice. We show that immunization of mice and guinea pigs with $\Delta menT4\Delta T3$ confers significant protection against *M. tuberculosis* infection. Remarkably, immunization of mice with $\Delta menT4\Delta T3$ results in increased antigen-specific T_H1 bias and activated memory T cell response. We conclude that MenT3 and MenT4 are important for *M. tuberculosis* pathogenicity and strains lacking *menT3* and *menT4* have the potential to be explored further as vaccine candidates.

TA systems are small genetic elements that are prevalent in most prokaryote genomes^{1–3}. TA systems comprise two genes that encode for a stable toxin and unstable antitoxin^{1–7}. TA systems have been classified into eight types based on the nature of antitoxin (protein or RNA) and the mechanisms by which toxin activity is neutralized^{2,8}. In type I, III and VIII TA systems, antitoxins are small non-coding RNAs

while in the remaining subfamilies, antitoxins are proteins^{2,8}. The toxins belonging to type I–type VII TA systems are proteinaceous in nature. However, in the case of the type VIII TA system, the toxin is a small RNA^{2,8}. The expression of toxins belonging to TA systems inhibits bacterial growth in either bactericidal or bacteriostatic manner by targeting essential cellular processes such as transcription, replication,

¹Centre for Tuberculosis Research, Translational Health Sciences and Technology Institute, NCR Biotech Science Cluster, 3rd Milestone, Faridabad-Gurugram Expressway, Faridabad 121001, India. ²Centre for Immunobiology and Immunotherapy, Translational Health Sciences and Technology Institute, NCR Biotech Science Cluster, 3rd Milestone, Faridabad-Gurugram Expressway, Faridabad 121001, India. ³Structural Biology Laboratory, Council of Scientific and Industrial Research-Institute of Microbial Technology (CSIR-IMTECH), Chandigarh 160036, India. ✉e-mail: ramandeep@thsti.res.in

translation, cell wall biosynthesis, membrane integrity and cytoskeleton formation^{1,9}. These systems have been demonstrated to contribute to plasmid maintenance, abortive phage infection, antibiotic persistence and pathogenesis^{1,10}. The detailed phylogenetic and bioinformatic analysis revealed that *M. tuberculosis* genome encodes for ≥ 90 TA systems, which are highly conserved in members of the *M. tuberculosis* complex^{11–14}. Most of these belong to various subfamilies of type II TA systems such as VapBC, MazEF, RelBE, HigBA, ParDE, HicAB, MbcAT, PezAT, DarTG and Rse-Xre. The toxins belonging to type II TA systems inhibit *M. tuberculosis* growth by cleaving either mRNA or tRNA or rRNA or degrading NAD⁺ or inhibiting DNA gyrase activity or by ADP ribosylation of single-stranded DNA^{15–20}. Additionally, subsets of TA systems exhibit differential expression patterns upon *M. tuberculosis* exposure to stress conditions^{12,21,22}. Many of these systems are dispensable for the survival of *M. tuberculosis* in stress conditions, thereby indicating that these modules might function cumulatively and contribute to stress adaptation^{18,21,23–25}. We have previously reported that TA systems or toxins belonging to the type II subfamily are essential for *M. tuberculosis* to establish infection in mice or guinea pigs^{21,23,25–27}.

The genome of *M. tuberculosis* encodes for four proteins belonging to the DUF1814 family of nucleotidyl transferases^{11,28}. These proteins, MenT1, MenT2, MenT3 and MenT4, share sequence homology with toxins from type IV TA systems. The antitoxins and toxins of type IV TA systems do not interact but compete for binding to the cellular target^{1,2,8}. MenT proteins harbor four highly conserved motifs, including nucleotidyl transferase (NTase) like domain. Motifs I and II are present at the amino-terminus and comprise of hG[G/S]X_{9–13}DhD domain. Due to its similarity to RxxRxxR observed in tRNA NTases, motif III, KLxAaxxR is predicted to be involved in base stacking interactions for incoming nucleotides. Motif IV comprises a pentad of conserved amino acids +DxxD. Studies have shown that mutation of highly conserved residues in MenT3 (G62 in motif I, D82 in motif II, K189 in motif III and D208 in motif IV) abolishes its growth inhibition activity in *E. coli*²⁹. The three-dimensional structures of MenT1, MenT3 and MenT4 toxins from *M. tuberculosis* have been solved at a resolution of 1.65 Å, 1.6 Å and 1.2 Å, respectively^{30,31}. These toxins feature a common toxin fold and are bilobed globular proteins³⁰. A more detailed analysis revealed that the overall architectures of MenT3 and MenT4 are similar with a root mean square deviation (RMSD) of 4.7 Å. Upon superimposition of the two structures, the authors observed that the active site residues of MenT3 (D80, K189 and D211) and MenT4 (D69, K171 and D186) were at a similar position³⁰. Superimposition of MenT1 with MenT3 or MenT4 resulted in an RMSD of 3.829 Å and 4.232 Å, respectively, and a similar alignment of core regions³¹. In another study it has been shown that MenA3 phosphorylates and inactivates the cognate toxin, MenT3²⁹. It has also been reported that MenT1, MenT3 and MenT4 possess nucleotidyl transferase activity^{30,31}. MenT3 displays a preference for pyrimidines and modifies *M. tuberculosis* tRNA^{Ser} isoacceptors³⁰. Cai et al. demonstrated that MenT3 also weakly modifies tRNA^{Leu}. Recently, it has been reported that MenT4 exhibits a preference for GTP and modifies several tRNAs, including tRNA^{Ser}³¹. Taken together, these findings suggest that overexpression of MenT toxins results in growth inhibition by preventing aminoacylation and tRNA charging^{30,31}.

Despite significant advancements in the characterization of type II TA systems, very limited information is available about the role of MenAT TA systems in the physiology and pathogenesis of *M. tuberculosis*. In the present study, we have performed experiments to investigate the contribution of MenT3 and MenT4 in *M. tuberculosis* physiology and pathogenesis. We show that MenT3 and MenT4 are mutually redundant and simultaneous deletion of *menT3* and *menT4* results in increased susceptibility to oxidative stress and severe attenuation of *M. tuberculosis* in mice and guinea pigs. Using host RNA-seq, we demonstrate that transcripts encoding for proteins involved in calcium signaling, immune responses, apoptosis, and autophagy were

differentially expressed in lung tissues of mice infected with Δ menT4ΔT3 relative to parental strain infected mice. We also demonstrate that immunization with Δ menT4ΔT3 strain (1) imparts significant protection against *M. tuberculosis* in mice and guinea pigs and (2) increases antigen-specific T_H1 immune responses and activated memory T-cell response in mice compared to naive mice. Taken together, this study has enhanced our understanding of the contribution of toxins belonging to MenAT TA systems in mycobacterial physiology and pathogenesis.

Results

Ectopic expression of MenT3 and MenT4 results in growth inhibition

In order to investigate the effect of overexpression of MenT3 or MenT4 on the growth of *E. coli* or *M. tuberculosis*, wild type toxins or their mutants were individually cloned in either pET28b (IPTG inducible) or pTetR (Atc inducible) expression vectors. As reported earlier, overexpression of MenT3 or MenT4 inhibited *E. coli* growth in comparison to uninduced cultures (Fig. 1a, b)³⁰. Further, G62, K189, D208 in motifs I, III and IV of MenT3 and G51, D71 in motifs I and II of MenT4 were mutated, cloned in pET28b and growth assays were performed (Fig. 1Sa). As expected, overexpression of either MenT3^{G62A} or MenT3^{K189A} or MenT3^{D208A} or MenT4^{G51A} or MenT4^{D71A} proteins did not inhibit *E. coli* growth (Figs. 1a, b and 1Sb). Next, to verify whether the co-expression of antitoxins can alleviate the growth inhibition activity of MenT3 and MenT4 toxins, we cloned them along with their cognate or non-cognate antitoxin in MCS-I and MCS-II of an IPTG inducible expression system, pETDuet. We observed that growth inhibition associated with MenT3 and MenT4 overexpression was restored by co-expression of their cognate antitoxins, MenA3 and MenA4, respectively (Fig. 1c, d). However, no growth restoration was seen upon co-expression of MenT3 and MenT4 with their non-cognate antitoxins (Fig. 1c, d). In agreement with *E. coli* data, we observed that inducible expression of either MenT3 or MenT4 also inhibited *M. tuberculosis* growth (Fig. 1e). In comparison to strain harboring vector control, overexpression of MenT3 and MenT4 reduced the bacterial growth by ~ 5.0-fold at 4 days post-induction (Fig. 1f). This growth defect upon overexpression of either MenT3 or MenT4 increased to ~28.0- and 15.0-fold, respectively, at 7 days post-induction (Fig. 1f).

Deletion of both *menT3* and *menT4* increases the susceptibility of *M. tuberculosis* to oxidative stress

The abundance of TA systems in members of the *M. tuberculosis* complex raises a possibility that these might function in a cumulative manner and contribute to *M. tuberculosis* survival in stress conditions and host tissues^{11,12,14}. In order to understand the role of MenT3 and MenT4 in the physiology of *M. tuberculosis*, we constructed Δ menT3, Δ menT4 single mutant and Δ menT4ΔT3 double mutant strain using temperature-sensitive mycobacteriophages (Fig. 1g). As shown in Fig. 1h, PCR amplification using *menT3* locus-specific primers resulted in amplifications of sizes 882 bp, 1.5 kb and 1.5 kb using genomic DNA isolated from wild type, Δ menT3 and Δ menT4ΔT3 strains of *M. tuberculosis*, respectively. PCR amplification of sizes 885 bp, 2.0 kb and 2.0 kb were obtained from genomic DNA isolated from wild type, Δ menT4 and Δ menT4ΔT3 strains of *M. tuberculosis*, respectively, using *menT4* locus primers (Fig. 1h). Whole genome sequencing revealed that sequences aligning to *menT3* and *menT4* locus were missing from the reads obtained from Δ menT4ΔT3 genomic DNA in comparison to reads obtained from the wild type strain (Fig. S2). These observations confirmed that the open reading frame for *menT3* and *menT4* has been replaced with kanamycin and hygromycin resistance gene, respectively, in the Δ menT4ΔT3 strain of *M. tuberculosis*.

We next compared the growth patterns of wild type and Δ menT4ΔT3 *M. tuberculosis* strains in liquid culture. We observed that both strains displayed comparable bacterial counts during various

stages of growth in vitro. We also compared the survival of parental and $\Delta menT4\Delta T3$ strains after exposure to various stress conditions. As shown in Fig. 2a, relative to the parental strain, $\Delta menT4\Delta T3$ strain was ~8.5-fold more susceptible to oxidative stress after exposure for 24 h. However, at 72 h post-exposure to oxidative stress, $\Delta menT4\Delta T3$ showed ~225.0-fold increased susceptibility in comparison to the parental strain (Fig. 2a). We also observed that complementation of the double mutant strain with *menT3* partially restored this growth defect (Fig. S3a). However, we were unable to restore this growth defect of double mutant strain upon complementation with *menT4* (Fig. S3a). qPCR studies revealed that the transcript levels for *menT3* and *menT4* were restored in their respective single-complemented strain (Fig. S5a). We also found that the sensitivity of wild type, $\Delta menT3$ and $\Delta menT4$ was comparable after being exposed to oxidative stress (Fig. S3c, d). Previously, it has been demonstrated that a subset of toxins is induced in response to stress conditions such as low oxygen, nutrient limiting, macrophage engulfment or drug exposure. The increased transcription and synthesis of toxins lead to TA systems activation and subsequent growth inhibition^{12,21,22,32}. Since $\Delta menT4\Delta T3$ was susceptible upon

exposure to oxidative stress relative to the parental strain, we next measured the relative levels of *menT3* and *menT4* in these conditions. We observed that the transcript levels of *menT3* and *menT4* remained unchanged after being exposed to oxidative stress (Fig. S3b). The survival of parental, $\Delta menT3$, $\Delta menT4$ and $\Delta menT4\Delta T3$ strains was comparable upon exposure to either nitrosative or nutritional or acidic stress (Figs. 2b–d and S3e–j). We also compared the ability of wild type, $\Delta menT3$, $\Delta menT4$ and $\Delta menT4\Delta T3$ to infect and survive inside THP-1 macrophages. The growth patterns of these strains were similar at days 2, 4 and 6 post-infection in macrophages (Figs. 2e and S4a, b). Taken together, these observations suggest that MenT3 and MenT4 are mutually redundant for in vitro growth, and simultaneous deletion of both *menT3* and *menT4* increased the susceptibility of *M. tuberculosis* to oxidative stress.

Deletion of both *menT3* and *menT4* impairs the virulence of *M. tuberculosis* in guinea pigs

Previously, we have reported that simultaneous deletion of MazF ribonucleases *mazF3*, *mazF6* and *mazF9* or *higB1* or *vapBC3* or *vapBC4*

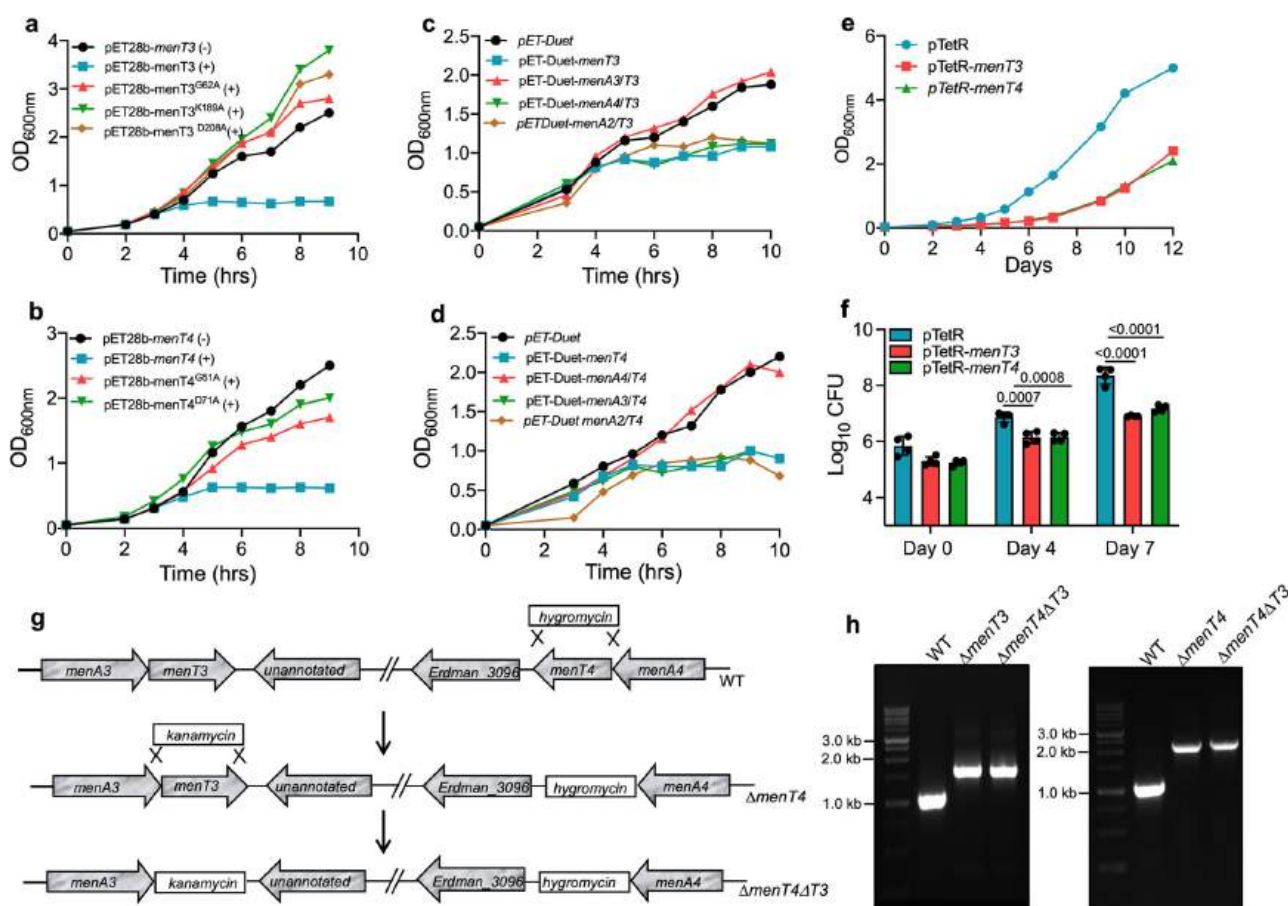


Fig. 1 | Functional characterization of MenT3 and MenT4 toxins belonging to MenAT subfamily of TA systems from *M. tuberculosis*. **a–f** Overexpression of MenT3 and MenT4 inhibits the growth of *E. coli* and *M. tuberculosis*. **a, b** These panels show growth patterns of *E. coli* BL-21 (pLysS, λ DE3) strains harboring pET28b derivatives expressing either wild type or mutant MenT3 (**a**) or wild type or mutant MenT4 (**b**) proteins in the absence or presence of inducer. **c, d** These panels depict growth patterns of *E. coli* BL21 (pLysS, λ DE3) strains harboring pET-Duet constructs overexpressing MenT3 (**c**) or MenT4 (**d**) either alone or along with their cognate or non-cognate antitoxins. The growth of various strains was determined by measuring OD_{600nm}. The data shown in these panels are representative of two independent experiments. **e, f** The growth patterns of *M. tuberculosis* H37Rv harboring pTetR derivatives expressing either MenT3 or MenT4 are shown in these panels. The growth of recombinant strains was determined by measuring either OD_{600nm} (**e**) or

bacterial counts (**f**). The data shown in (**e**) is representative of two independent experiments. The data shown in (**f**) is mean \pm SD of log₁₀ CFU obtained from two independent experiments, each performed with duplicate cultures. *p* values depicted on the graphs were assessed using one-way ANOVA. **g, h** Construction of $\Delta menT4\Delta T3$ strain of *M. tuberculosis*. **g** Schematic representation of *menT3* and *menT4* locus in parental, $\Delta menT4$ and $\Delta menT4\Delta T3$ strain of *M. tuberculosis* Erdman is shown. The open reading frame of *menT4* was replaced with the hygromycin resistance gene in $\Delta menT4$ strain of *M. tuberculosis*. In the double mutant strain, $\Delta menT4\Delta T3$, the open reading frame of *menT3* and *menT4* were replaced with kanamycin and hygromycin resistance gene, respectively. **h** The replacement of *menT3* and *menT4* with kanamycin and hygromycin resistance gene, respectively, in their respective single and double mutant strain was confirmed by PCR using gene-specific primers. Source Data are provided as a Source Data file.

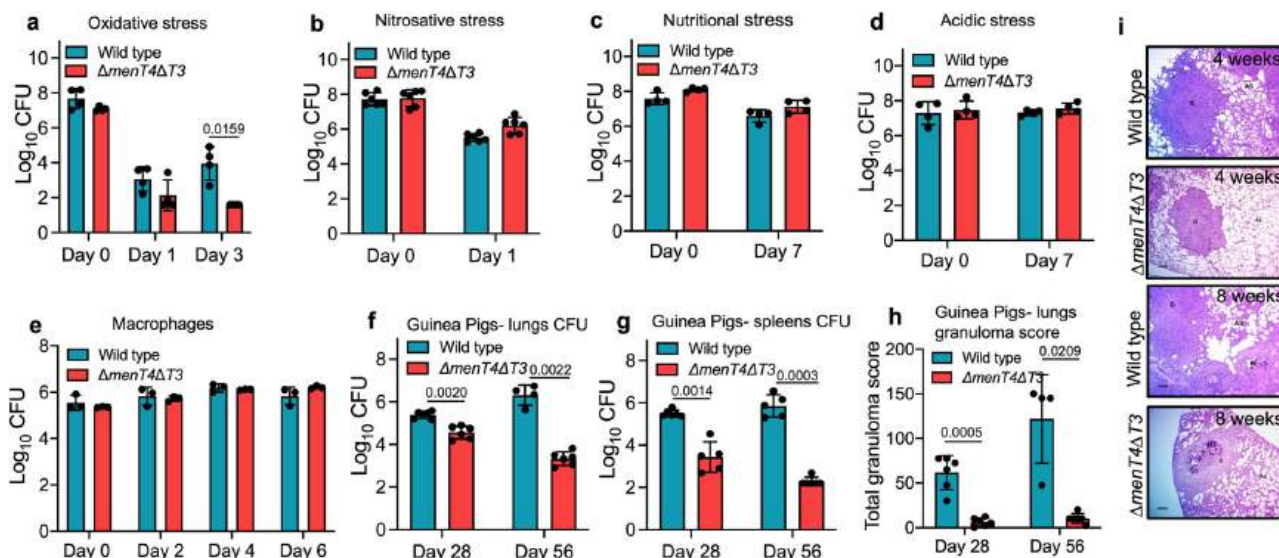


Fig. 2 | MenT3 and MenT4 are cumulatively essential for *M. tuberculosis* to survive in oxidative stress and establish infection in guinea pigs. The growth of wild type and $\Delta menT4\Delta T3$ was compared after exposure to either oxidative (a) or nitrosative (b) or nutritional (c) or acidic (d) stress. The data shown in these panels are mean \pm SD of \log_{10} CFU obtained from two (a, c, d) or three (b) independent experiments, each performed with duplicate cultures. e THP-1 macrophages were infected with various strains, and the number of intracellular bacteria was determined at different time points. The data shown in this panel are mean \pm SD of \log_{10} CFU obtained from triplicate wells and representative of two independent experiments performed in duplicates or triplicates. The data shown in these panels in mean \pm SD of \log_{10} CFU in lungs (f) and spleens (g) of guinea pigs (Duncan Hartley strain) infected with either wild type or $\Delta menT4\Delta T3$ strain at 4- and 8-weeks post-infection. The data shown in these panels in mean \pm SD of \log_{10} CFU obtained from

6 animals (except in (f) week 8, wild type $n = 4$ and in (g) week 4, $\Delta menT4\Delta T3$ $n = 5$ and week 8, wild type $n = 5$). The data shown for the 4-week time point are representative of two independent experiments. The data shown for the 8-week time point are obtained from a single experiment. h The data shown in this panel are mean \pm SD of total granuloma score in H&E-stained sections of guinea pigs infected with wild type or $\Delta menT4\Delta T3$ strain of *M. tuberculosis* at 4- and 8-weeks post-infection. The data shown are obtained from 6 animals from a single experiment (except in week 8, wild type $n = 4$). i This panel shows representative images of H&E-stained sections of lung tissues of guinea pigs infected with either wild type or $\Delta menT4\Delta T3$ strain at 4- or 8-week post-infection. Scale bar, 100 μ m. p values depicted on the graphs were assessed using a two-tailed paired *t*-test. Source Data are provided as a Source Data file.

or *vapBC11* or *vapC22* significantly reduced *M. tuberculosis* growth in guinea pigs^{21,23,25–27}. However, deletions in either *relE1* or *relE2* or *relE3* or *vapC28* or *vapC21* or *darTG* did not reduce *M. tuberculosis* growth in guinea pigs or mice^{21,24,33,34}. In addition to type II TA systems, we have recently shown that MenT2 toxin belonging to the MenAT subfamily is also essential for *M. tuberculosis* pathogenesis in guinea pigs³⁵. Previously, high throughput screening assays such as transposon site hybridization (TRASH) and designer array for defined mutant analysis (DeADMan) have been performed to identify genes necessary for in vivo growth of *M. tuberculosis*^{36,37}. According to these studies, *menT3* and *menT4* are mutually redundant and not required for *M. tuberculosis* to establish infection in mice^{36,37}. In the present study, we compared the growth of wild type and $\Delta menT4\Delta T3$ strains in aerosol-infected guinea pigs. We observed that lung bacillary loads were decreased by ~ 6.6- and 950.0-fold in guinea pigs infected with $\Delta menT4\Delta T3$ at 4- and 8 weeks post-infection, respectively, relative to parental strain infected guinea pigs (Fig. 2f). As shown in Fig. 2g, we observed ~117.0- and ~3750.0-fold reduction in bacterial loads in spleens of $\Delta menT4\Delta T3$ infected guinea pigs relative to wild type strain infected guinea pigs at 4- and 8-weeks post-infection, respectively. In agreement with bacterial burdens, H&E-stained lung sections from guinea pigs infected with wild type strain displayed increased cellular infiltration and severely reduced alveolar spaces (Fig. 2i). This increased cellular infiltration indicates severe inflammation and pathology in lung tissue sections of wild type strain infected guinea pigs at both time points (Fig. 2i). In comparison, the histologically stained lung sections of $\Delta menT4\Delta T3$ infected guinea pigs demonstrated intact lung architecture and large alveolar spaces at both time points (Fig. 2i). At both time points, the total granuloma score in lungs of $\Delta menT4\Delta T3$ infected guinea pigs was significantly decreased by ~10.0-fold in comparison to total granuloma score in lung sections

from guinea pigs infected with the wild type strain (Fig. 2h). Taken together, we demonstrate that simultaneous deletion of *menT3* and *menT4* results in attenuation of *M. tuberculosis* growth in guinea pigs.

Deletion of both *menT3* and *menT4* alters the transcriptional profiles of *M. tuberculosis*

We next compared the transcriptional profiles of mid-log phase cultures of wild type and $\Delta menT4\Delta T3$ strain to identify the differentially expressed pathways following the simultaneous deletion of *menT3* and *menT4* in *M. tuberculosis*. Using a 2.0-fold cut-off and p_{adj} value of ≤ 0.05 , we observed that compared to the parental strain, transcripts encoding for 36 and 51 proteins were increased and decreased, respectively, in $\Delta menT4\Delta T3$ (Supplementary Data 1). The DEGs were further annotated as per the functional category listed by mycobrowser (<https://mycobrowser.epfl.ch/>). Approximately, 33 and 23% of the transcripts with differential expression encoded for either conserved hypothetical proteins or proteins involved in intermediary metabolism and respiration (Table 1). Interestingly, we observed that the expression of toxins belonging to type II TA systems such as Erdman_0269 (Rv0240, *vapC24*), Erdman_0658 (Rv0598c, *vapC27*), Erdman_2181 (Rv1982c, *vapC36*) and Erdman_2744 (Rv2494, *vapC38*) was increased in mid-log phase cultures of $\Delta menT4\Delta T3$ relative to the wild type strain (Supplementary Data 1). We also noticed that relative to the parental strain, the levels of transcripts encoding for proteins involved in *M. tuberculosis* adaptation in host tissues were significantly reduced in the $\Delta menT4\Delta T3$. These included Erdman_0097 (Rv0081), a regulatory protein known to be upregulated upon exposure to low oxygen and Erdman_0100 (Rv0084, *hycD*), a protein involved in formate metabolism^{38,39}. In addition to these, the transcript levels of Erdman_0321 (Rv0287, *esxG*), a protein involved in the inhibition of phagosome maturation and pathogenesis of *M. tuberculosis*, were also

Table 1 | Differential expression of genes in $\Delta menT4\Delta T3$ strain relative to the wild type strain

S. No	Functional category	No. of down-regulated DEGs	No. of upregulated DEGs
1.	Conserved hypothetical protein	17	11
3.	Intermediary metabolism and respiration	9	11
4.	Virulence, detoxification, adaptation	2	4
5.	PE/PPE	8	–
6.	Lipid metabolism	3	–
7.	Cell wall and cell processes	10	6
8.	Regulatory proteins	1	–
9.	Information pathways	1	3
10.	Stable RNA	–	1

The number of upregulated and downregulated genes in the $\Delta menT4\Delta T3$ strain classified as per their functional annotation are shown. The data were obtained from two biological replicates.

reduced in the $\Delta menT4\Delta T3$ strain (Supplementary Data 1)⁴⁰. As shown in Supplementary Data 1, the levels of transcripts encoding for proteins essential for growth (Erdman_3437 (Rv3137), Erdman_3739 (Rv3418c), stress adaptation (Erdman_0630 (Rv0574c), Erdman_2884 (Rv2624c)) and interaction with host Interferon- γ (IFN- γ) (Erdman_1325, Rv1183) were also reduced in $\Delta menT4\Delta T3$ strain relative to the parental strain^{36,41–44}. Several studies have reported that replacing an open reading frame with an antibiotic selection marker might affect the expression of neighboring genes due to the polar effect. However, we observed that the relative levels of *menT3* and *menT4* neighboring genes were comparable in both wild type and $\Delta menT4\Delta T3$ strains (Fig. S5b and Supplementary Data 1). Another possible explanation for the observed attenuated phenotype of $\Delta menT4\Delta T3$ in vivo might be the loss of apolar lipids such as PDIMs during in vitro culturing⁴⁵. In order to rule out this possibility, we compared polar and apolar lipid profiles of mid-log phase cultures of wild type, $\Delta menT3$, $\Delta menT4$ and $\Delta menT4\Delta T3$ strains. We observed that the relative levels of apolar lipids (PDIMs, TAG), mycolic acids (MAMEs, FAMEs) and polar lipids (TAG, FAM and DAG) were comparable in wild type and various mutant strains (Fig. S5c). Overall, the data suggests that the attenuated phenotype of the $\Delta menT4\Delta T3$ strain in guinea pigs is most likely associated with reduced levels of transcripts encoding for proteins required for either stress adaptation or virulence of *M. tuberculosis*.

Deletion of both *menT3* and *menT4* results in attenuation of *M. tuberculosis* growth in mice

We next compared the growth of wild type and $\Delta menT4\Delta T3$ strain in aerosol-infected Balb/c mice at 4 and 8-weeks post-infection. As shown in Fig. 3a, b, the lung and splenic bacillary loads in $\Delta menT4\Delta T3$ infected mice were decreased by 10.0- and 14.0-fold, respectively, in comparison to wild type infected mice at 4-weeks post-infection. However, at 8 weeks post-infection, we observed 7.0- and 13.0-fold reduction in lungs and splenic bacillary loads in $\Delta menT4\Delta T3$ infected mice compared to mice infected with the wild type strain (Fig. 3a, b). As shown in Fig. S4c, d, we were unable to restore this growth defect in the lungs and spleens of infected animals upon complementation of the double mutant strain with either *menT3* or *menT4*. These observations suggest that both *MenT3* and *MenT4* contribute cumulatively to the ability of *M. tuberculosis* to establish infection in host tissues. We next performed RNA-seq analysis of lung tissues of uninfected mice and those infected with either parental or $\Delta menT4\Delta T3$ strains at 4-weeks post-infection to understand the plausible underlying mechanisms associated with the attenuated phenotype of the double mutant strain in vivo. Using a p_{adj} value of ≤ 0.05 and a cut-off fold change value of

4.0 and -4.0 , we observed that relative to uninfected animals, the expression of 826 and 423 transcripts were increased or decreased in mice infected with the parental strain (Figs. 3c, S4e and Supplementary Data 2). As shown in Fig. 3c, the transcript levels of 312 and 119 genes were increased or decreased, respectively, in mice infected with the $\Delta menT4\Delta T3$ strain relative to uninfected animals (Fig. S4f and Supplementary Data 3). The transcript levels of 330 and 160 genes were increased or decreased in animals infected with $\Delta menT4\Delta T3$ strain in comparison to profiles obtained from parental strain-infected mice (Fig. 3c, d and Supplementary Data 4).

We noticed that relative to the parental strain, the transcript levels of genes encoding for proteins involved in calcium signaling were increased in animals infected with $\Delta menT4\Delta T3$ strain (Fig. 3e and Supplementary Data 4). Previously, it has been shown that increased calcium levels are associated with the induction of numerous anti-microbial pathways such as autophagy and apoptosis⁴⁶. Previously, it has been reported that *Adcy1* is activated by *apoA-1* to promote cholesterol efflux from THP-1 macrophage foam cells⁴⁷. The formation of foamy macrophages is associated with disease progression that leads to cavitation and release of infectious bacilli⁴⁸. In agreement, we observed ~ 4.0 -fold increased expression of *adcy1* in the lungs of mice infected with $\Delta menT4\Delta T3$ strain relative to the parental strain (Supplementary Data 4). *M. tuberculosis* inhibits phagolysosome fusion by interfering with phosphatidylinositol 3-phosphate (PI3P) signaling⁴⁹. We observed increased expression of *adra1a* in lung tissues of $\Delta menT4\Delta T3$ strain-infected mice compared to the parental strain (Supplementary Data 4). *Adra1a* is involved in the release of inositol 1,4,5-triphosphate and the activation of protein kinase C^{50–52}. Studies have shown that deletion of protein kinase C results in higher susceptibility to TB due to increased lung pathology, the release of proinflammatory cytokines and bacterial burdens^{53,54}. Numerous studies have shown that bacterial pathogens are able to establish persistent infection by subverting autophagy⁵⁵. We observed that the levels of transcripts encoding for proteins involved in apoptosis and autophagy, such as *slc4a1*, *bub1*, *nod1*, *rnfl52*, *atg16l1*, *gba*, *tsc1*, *phf23*, *map2k7*, *mfn2* and *wnt11*, were differentially expressed in lung tissues of mice infected with $\Delta menT4\Delta T3$ strain compared to the parental strain (Fig. 3f and Supplementary Data 4). Autophagy acts as an immune effector mechanism, resulting in phagosomal maturation that mediates mycobacteria clearance⁵⁶. Studies have shown that *Bub1* and *Phf23* act as negative regulators of autophagy^{57–59}. As shown in Supplementary Data 4, we observed reduced expression of *bub1* and *phf23* transcript in lung tissues of $\Delta menT4\Delta T3$ strain infected mice relative to the parental strain infected animals. Additionally, we observed that the levels of transcripts encoding for *atg16l1* were increased in $\Delta menT4\Delta T3$ infected mice lung tissues (Fig. 3f and Supplementary Data 4). Previously it has been shown that depletion of *Atg16l1* is associated with increased *M. tuberculosis* growth and susceptibility in mice⁶⁰. The reduced levels of *ptpro* also suggest reduced inflammation and enhanced apoptosis in lung tissues of $\Delta menT4\Delta T3$ infected animals relative to mice infected with the parental strain⁶¹ (Supplementary Data 4). We also observed an increased level of *wnt11* transcript in lung tissues of $\Delta menT4\Delta T3$ strain infected mice compared to the parental strain infected animals (Supplementary Data 4). Previously, it has been shown that overexpression of *wnt11* in intestinal epithelial cells decreased *Salmonella* invasion and inhibited bacteria induced intestinal inflammation⁶².

Furthermore, we observed varied expression of several transcripts associated with immune response in $\Delta menT4\Delta T3$ strain infected mice relative to the parental strain infected mice (Supplementary Data 4). We observed reduced levels of transcripts encoding for various cytokines and chemokines such as *il-21*, *ccl1*, *cxcl5*, *cxcl3*, *ccl4*, and *ccl21a* in $\Delta menT4\Delta T3$ infected mice (Fig. 3g and Supplementary Data 4). Studies have shown that increased expression of *Ccl1* is associated with increased endoplasmic reticulum stress and

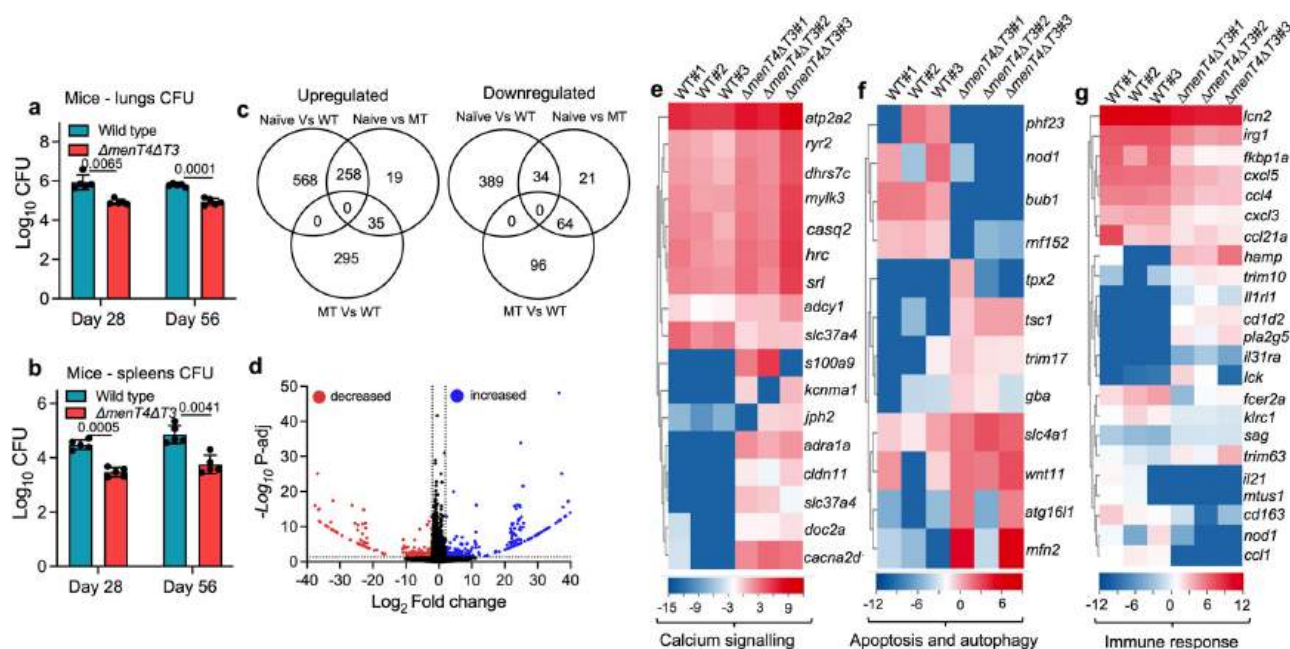


Fig. 3 | Global transcriptional changes in lung tissues of mice infected with either wild type or $\Delta menT4\Delta T3$ strain at 4 weeks post-infection. **a, b** Deletion of *menT3* and *menT4* attenuates *M. tuberculosis* growth in lungs and spleens of mice. The data shown in these panels are mean \pm SD of \log_{10} CFU in lungs (**a**) or spleens (**b**) of infected Balb/c mice at 4- and 8-weeks post-infection obtained from 5 animals. The data shown in these panels for 4-week time point are representative of two independent experiments. The data shown for the 8-week time point are obtained from a single experiment. p values depicted on the graphs were assessed using a two-tailed paired t -test. **c-g** Host transcriptional profiles of lung tissues from uninfected or mice infected with either wild type or $\Delta menT4\Delta T3$ strain. **c** Venn diagram depicting correlation of expression profiles obtained from lung tissues of either uninfected or mice infected with parental or $\Delta menT4\Delta T3$ strain at 4 weeks

post-infection. **d** Volcano plot comparing transcription profiles obtained from lung tissues of mice infected with either wild type or $\Delta menT4\Delta T3$ strain at 4 weeks post-infection. The transcripts with increased or decreased expression have been shown as blue or red dots, respectively. The black dots represent the transcripts that remain unchanged and are not statistically different between these two groups. **e-g** Heat maps showing transcripts with differential expression in mice infected with either wild type or $\Delta menT4\Delta T3$ strain at 4 weeks post-infection. The transcripts with differential expression in mice infected with these strains are involved in either calcium signaling (**e**) or apoptosis/autophagy (**f**), or immune response (**g**). The color intensity in heatmaps represents the \log_2 value of normalized expression counts. The data shown in (**c-g**) are obtained from three independent biological replicates. Source Data are provided as a Source Data file.

granuloma formation during mycobacterial treatment⁶³. Further, it has been reported that elevated plasma levels of Ccl1, Ccl3, Cxcl1, Cxcl9, and Cxcl10 correlate with disease severity in infected individuals⁶⁴. Furthermore, Cxcl5 secreted by pulmonary epithelial cells contributes to excessive neutrophilic inflammation, and mice deficient in Cxcl5 exhibit enhanced survival upon high-dose of *M. tuberculosis* infection compared to wild type mice⁶⁵. The transcript levels of *sag*, *hamp*, *il1rl1*, *lck*, and *pla2g5* that encode for proteins involved in the activation of macrophages, neutrophils or T-cells were also increased in lung tissues of mice infected with the mutant strain in comparison to lung tissues from parental strain infected mice (Fig. 3g and Supplementary Data 4)^{66–69}. It has also been reported that increased levels of Pla2g5 result in enhanced adaptive immune response and phagocytosis of bacteria by macrophages^{70,71}. Taken together, these observations suggest that the in vivo attenuated phenotype of $\Delta menT4\Delta T3$ in lung tissues is most likely associated with increased expression of proteins involved in either calcium homeostasis, apoptosis or autophagy along with decreased expression of transcripts associated with inflammatory response.

Immunization with $\Delta menT4\Delta T3$ strain imparts protection in mice and guinea pigs against *M. tuberculosis* challenge

Studies have shown that immunization of animals with live attenuated *M. tuberculosis* strains provides long-term protection against challenge with virulent strain as these strains closely mimic the antigenic repertoire of the infectious agent^{72–74}. Since *M. tuberculosis* is an intracellular pathogen with pulmonary pathology driven by IFN γ response, C57BL/6 is a widely used strain to study immunological responses, DC-NK cross-talk and T_H1 cellular responses^{75–80}. Since $\Delta menT4\Delta T3$ was significantly

attenuated for growth in guinea pigs, we next evaluated whether immunization with this strain imparts protection against *M. tuberculosis* challenge in C57BL/6 mice (Fig. 4a). We found that the number of immunizing bacilli (*Mycobacterium bovis* Bacille Calmette- Guerin Pasteur, BCG and $\Delta menT4\Delta T3$) in lungs and spleens of immunized C57BL/6 mice were below the detection limit at 6 weeks post-immunization. In comparison to naive mice, vaccination with $\Delta menT4\Delta T3$ reduced lung and splenic loads of *M. tuberculosis* by -7.5- and 5.0-folds, respectively, at 4 weeks post-infection (Fig. 4b, c). In comparison to naive mice, immunization with BCG reduced the bacterial counts by 32.0-fold and 7.5-fold in lungs and spleens, respectively, at 4 weeks post-infection (Fig. 4b, c). At 10 weeks post-challenge with *M. tuberculosis*, immunization with $\Delta menT4\Delta T3$ reduced the bacterial numbers by - 4.5-fold and 18.5-fold in lungs and spleens, respectively, in comparison to naive mice (Fig. 4d, e). At 10 weeks post-infection, in comparison to naive mice, immunization with BCG reduced lungs and splenic bacillary loads by -8.5-fold and 4.4-fold, respectively (Fig. 4d, e). We observed that immunization with $\Delta menT4\Delta T3$ imparted -4.0-fold increased protection in comparison to immunization with BCG in spleens at 10 weeks post-infection (Fig. 4e).

Next, we assessed the ability of $\Delta menT4\Delta T3$ to impart protection against challenge with *M. tuberculosis* in guinea pigs (Duncan Hartley strain) (Fig. 4f). As observed in C57BL/6 mice, the lung and splenic bacillary loads in BCG and $\Delta menT4\Delta T3$ immunized guinea pigs were below the detection limit at 6 weeks post-immunization. In comparison to naive guinea pigs, we observed -70.0-fold and 6.0-fold reduction in bacterial numbers in the lungs of $\Delta menT4\Delta T3$ and BCG vaccinated guinea pigs, respectively, at 4 weeks post-infection (Fig. 4g). We observed -11.0-fold reduction in lung bacillary loads in

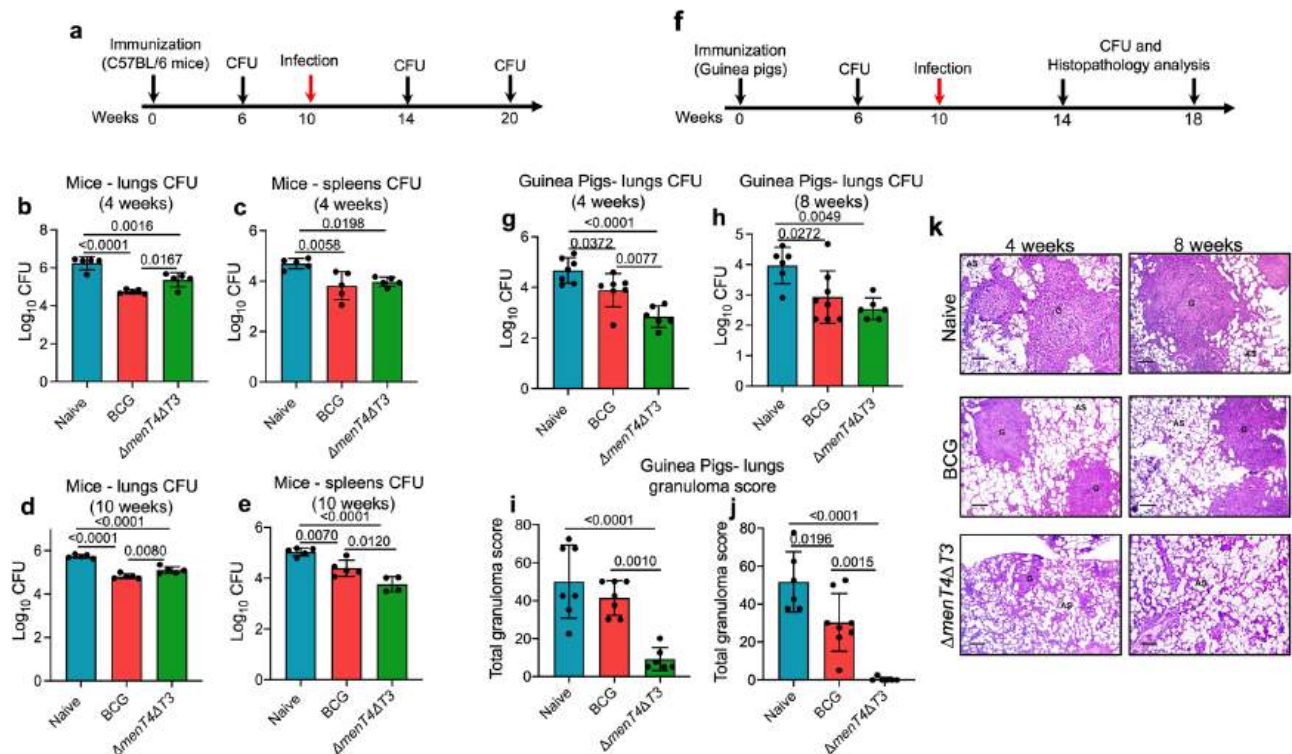


Fig. 4 | Immunization of mice and guinea pigs with $\Delta menT4\Delta T3$ imparts protection against *M. tuberculosis* challenge. **a–f** 8 weeks old female C57BL/6 mice were immunized subcutaneously with 5×10^5 CFU of either *M. bovis* BCG or $\Delta menT4\Delta T3$. At 10 weeks post-immunization, animals were challenged with *M. tuberculosis* and bacterial enumeration was performed at 4- and 10 weeks post-infection. **b–e** The data shown in these panels is mean \pm SD of \log_{10} CFU in lungs (**b, d**) and spleens (**c, e**) of naive or BCG or $\Delta menT4\Delta T3$ immunized mice after challenge with *M. tuberculosis* at 4 weeks (**b, c**) and 10 weeks (**d, e**) post-infection. The data shown in these panels are mean \pm SD of \log_{10} CFU obtained from 5 animals from a single experiment (except in **e**) week 10, $\Delta menT4\Delta T3$ $n = 4$). **f** 6–8-week-old female guinea pigs (Duncan Hartley strain) were immunized intradermally with 1×10^5 CFU of either *M. bovis* BCG or $\Delta menT4\Delta T3$. At 10 weeks post-immunization, animals were challenged with *M. tuberculosis* and bacterial enumeration and histopathology analysis were performed at 4 and 8-weeks post-infection. The bacterial

burdens in the lungs of naive or BCG or $\Delta menT4\Delta T3$ immunized guinea pigs were determined after challenge with *M. tuberculosis* at 4 (**g**) and 8 weeks (**h**) post-challenge. The data shown are mean \pm SD of \log_{10} CFU obtained from 6 animals from a single experiment (except in **g**) week 4, naive and BCG $n = 7$ and in **h**) week 8, BCG $n = 8$). The data shown in this panel are mean \pm SD of total granuloma score obtained from H&E stained lung sections of naive or BCG or $\Delta menT4\Delta T3$ immunized guinea pigs at 4 weeks (**i**) and 8 weeks (**j**) post-challenge. The data shown are obtained from 6 animals from a single experiment (except in **i**) week 4, naive and BCG $n = 7$ and in **j**) week 8, BCG $n = 8$). **k** This panel shows representative images of H&E-stained sections of lung tissues of naive or immunized guinea pigs after infection with *M. tuberculosis* for 4 weeks or 8 weeks. Scale bar, 100 μ m. p values depicted on the graphs were assessed using one-way ANOVA. Source Data are provided as a Source Data file.

$\Delta menT4\Delta T3$ immunized animals in comparison to BCG vaccinated guinea pigs (Fig. 4g). Further, we observed immunization with either BCG or $\Delta menT4\Delta T3$ reduced lung bacillary loads by 11.0- and 27.0-fold, respectively, in comparison to naive animals at 8 weeks post-challenge (Fig. 4h). However, 2.5-fold increased protection in $\Delta menT4\Delta T3$ immunized animals in comparison to BCG immunized guinea pigs was not statistically significant (Fig. 4h). We also performed histopathology analysis of lung sections to determine the extent of disease progression in unvaccinated and vaccinated guinea pigs at both time points. As shown in Fig. 4i, j, the total granuloma score in lung sections of naive guinea pigs was 50.0 at both time points. In comparison, the total granuloma score in guinea pigs immunized with BCG was reduced by 1.70-fold in comparison to naive animals at 8-weeks post-infection (Fig. 4j). In comparison to naive guinea pigs, immunization with $\Delta menT4\Delta T3$ significantly reduced the total granuloma score by 5.5- and 124.0-fold at 4- and 8-weeks post-infection, respectively (Fig. 4i, j). The total granuloma score was reduced by 4.5- and 73.0-fold in $\Delta menT4\Delta T3$ immunized guinea pigs in comparison to guinea pigs immunized with BCG at 4- and 8-weeks post-infection, respectively (Fig. 4i, j). The histopathological analysis revealed large granulomas and significant tissue damage in H&E-stained lung sections from naive animals. In comparison, the number of tubercles and tissue damage was reduced in guinea pigs immunized

with BCG (Fig. 4k). In agreement with the total granuloma score, we observed normal lung architecture and few granulomas in the H&E-stained section of guinea pigs immunized with $\Delta menT4\Delta T3$ at both time points (Fig. 4k). Taken together, these observations suggest that immunization with $\Delta menT4\Delta T3$ resulted in significant protection against challenge with *M. tuberculosis* in both mice and guinea pigs.

Immunization of mice with $\Delta menT4\Delta T3$ induces a T_H1 -biased response and activated memory T cell response

In order to determine immune correlates of protection in $\Delta menT4\Delta T3$ immunized mice, we evaluated the antigen-specific adaptive T cell response in spleens of naive, BCG and $\Delta menT4\Delta T3$ vaccinated C57BL/6 mice at 6 weeks post-immunization (Fig. S6). We observed that immunization of mice with $\Delta menT4\Delta T3$ promoted antigen-specific T_H1 response by increasing the frequency of IFN- γ^+ CD4 $^+$ T-cells by 270% and 190% in comparison to naive and BCG immunized mice, respectively (Fig. 5a, b). Also, in comparison to naive mice, immunization with BCG resulted in 145% increase in the frequency of IFN- γ^+ CD4 $^+$ T-cells (Fig. 5a, b). Similarly, we observed an increase in the frequency of IFN- γ^+ CD8 $^+$ T-cells by 300–450% in $\Delta menT4\Delta T3$ vaccinated mice compared to naive and BCG immunized mice (Fig. 5d, e). T-bet is the master transcription factor for T_H1 cells and also negatively regulates T_H2 immune response⁸¹. In comparison to naive mice, immunization with

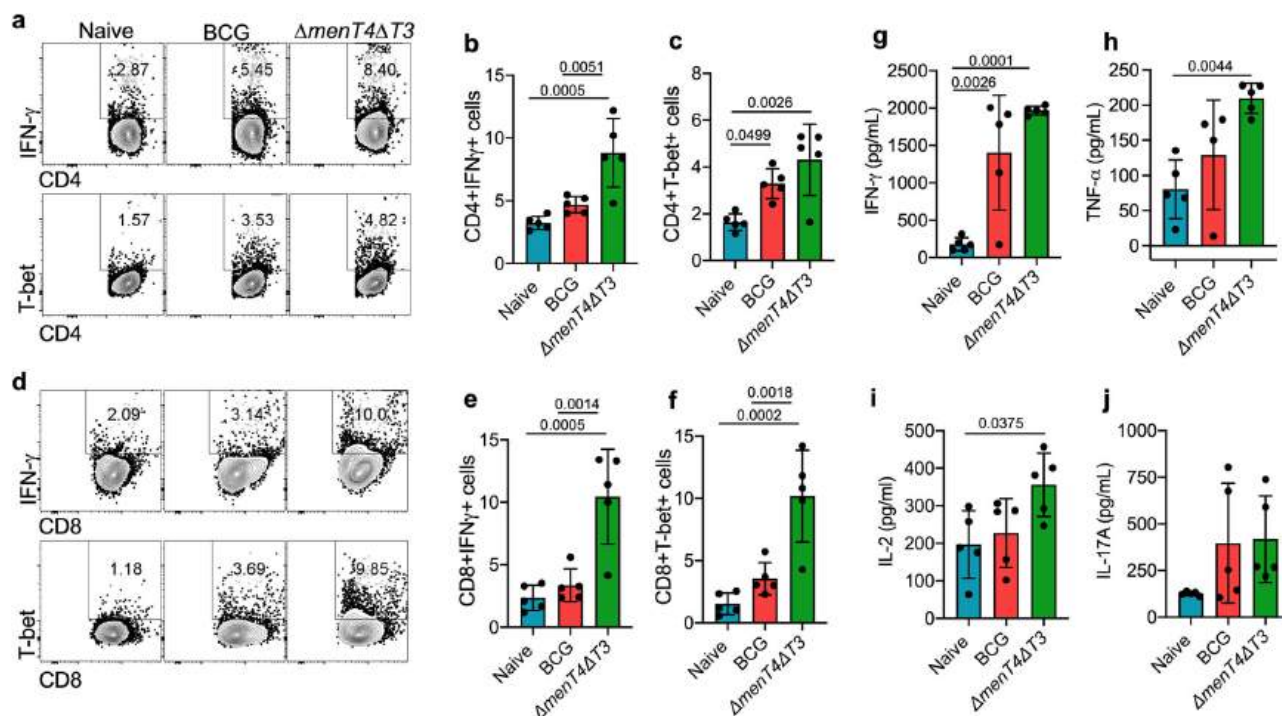


Fig. 5 | Immunization of mice with $\Delta menT4\Delta T3$ results in increased antigen-specific T_H1 response. **a–f** C57BL/6 mice immunized with saline or BCG or $\Delta menT4\Delta T3$ were sacrificed at 6 weeks post-immunization, and intracellular cytokines were measured in PPD-stimulated splenocytes. **a** Representative FACS plots depicting percentage frequency of CD4⁺ IFN- γ ⁺ and CD4⁺ T-bet⁺ T cells in spleens of naive or BCG or $\Delta menT4\Delta T3$ immunized mice. These panels show mean \pm SD of percentage frequency CD4⁺ IFN- γ ⁺ (**b**) and CD4⁺ T-bet⁺ (**c**) in spleens of naive or BCG or $\Delta menT4\Delta T3$ immunized mice. **d** Representative FACS plots depicting percentage frequency of CD8⁺ IFN- γ ⁺ and CD8⁺ T-bet⁺ T cells in spleens of naive or BCG or $\Delta menT4\Delta T3$ immunized mice. These panels show the percentage frequency of

CD8⁺ IFN- γ ⁺ (**e**) and CD8⁺ T-bet⁺ (**f**) T cells in the spleens of naive or BCG or $\Delta menT4\Delta T3$ immunized mice. The data shown in (**b**, **c**, **e**, **f**) are mean \pm S.D. of the proportion of T-cells obtained from five animals from a single experiment. The levels of secreted IFN- γ (**g**), TNF- α (**h**), IL-2 (**i**), IL-17A (**j**) were measured in the culture supernatants from PPD-stimulated splenocytes by ELISA. The data shown are mean \pm SD of cytokine levels in PPD-stimulated splenocytes obtained from five animals from a single experiment (except in (**h**), BCG $n = 4$). p values depicted on the graphs were assessed using one-way ANOVA. Source Data are provided as a Source Data file.

$\Delta menT4\Delta T3$ significantly enhanced the frequency of T-bet⁺ expressing CD4⁺ and CD8⁺ T cells by ~250% and ~650%, respectively (Fig. 5a, c, d, f). In comparison to BCG immunized mice, the frequency of T-bet⁺ expressing CD4⁺ and CD8⁺ T-cells were increased by 130.0% and 285.0%, respectively, in $\Delta menT4\Delta T3$ immunized mice, respectively (Fig. 5a, c, d, f). We also observed that the frequency of T-bet⁺ expressing CD4⁺ and CD8⁺ T cells increased by 2.0- and 2.31-fold in BCG immunized mice as compared to naive mice (Fig. 5a, c, d, f). The frequency of IL-17A secreting CD4⁺ T cells in $\Delta menT4\Delta T3$ immunized mice and BCG immunized mice increased by ~150% and 140%, respectively, in comparison to naive mice (Fig. S7a, b). This increase was observed to be non-significant in comparison to the proportion of cells obtained in naive mice. We also determined the levels of various cytokines in the supernatants of PPD-stimulated splenocytes. In agreement with our immunophenotyping experiments, the levels of IFN- γ were significantly increased in culture supernatants from PPD-stimulated splenocytes obtained from BCG and $\Delta menT4\Delta T3$ immunized groups in comparison to naive animals (Fig. 5g). Notably, TNF- α levels were increased by ~1.6-fold and ~2.5-fold in culture supernatants from PPD-stimulated splenocytes obtained from the $\Delta menT4\Delta T3$ immunized group in comparison to BCG immunized and naive group (Fig. 5h). The levels of IL-2 were also significantly increased in culture supernatants from PPD-stimulated splenocytes obtained from $\Delta menT4\Delta T3$ immunized mice in comparison to naive animals (Fig. 5i). In agreement with FACS data, the levels of secreted IL-17A were not significantly changed in supernatants of PPD-stimulated splenocytes from naive, BCG and $\Delta menT4\Delta T3$ immunized mice (Fig. 5j). Previously, it has been shown that the FoxP3 transcription factor is mostly

expressed by regulatory T cells and dampens the antimicrobial inflammatory immune response^{82,83}. Immunization of mice with $\Delta menT4\Delta T3$ did not result in significant changes in the frequency of FoxP3⁺CD4⁺ T-cells in comparison to naive mice (Fig. S7a, c). These observations suggest that $\Delta menT4\Delta T3$ immunization-induced protection against *M. tuberculosis* challenge might be independent of Treg cells. Together, our data suggests that immunization with $\Delta menT4\Delta T3$ results in the expansion of antigen-specific T_H1 response, which may contribute to protection against *M. tuberculosis* infection.

Furthermore, we also evaluated the effector and memory T cell response in spleens of immunized mice (Fig. S8). We observed a significant increase in the frequency of activated memory T helper and T cytotoxic cells by 2.70-fold and 3.80-fold, respectively, in $\Delta menT4\Delta T3$ immunized mice and by ~1.60- and 2.30-fold, respectively, in mice immunized with BCG in comparison to naive mice (Fig. 6a–d). In comparison to BCG immunized mice, the frequency of activated memory CD4⁺ and CD8⁺ T cells were increased by ~1.70- and 1.60-fold, respectively, in $\Delta menT4\Delta T3$ immunized mice (Fig. 6a–d). Furthermore, a slight increase, though not statistically significant, in the frequency of effector T helper cells was observed in $\Delta menT4\Delta T3$ immunized as compared to naive mice (from 14.96 to 17.62%) and BCG immunized mice (from 11.44 to 17.62%) (Fig. S9a, c). Moreover, in comparison to naive mice, the frequency of effector memory CD4⁺ T cells decreased from 18.2 to 13.26% in $\Delta menT4\Delta T3$ immunized mice (Fig. S9a, d). We also observed that the frequency of effector memory CD4⁺ T cells was significantly reduced in $\Delta menT4\Delta T3$ immunized mice in comparison to BCG immunized mice (Fig. S9a, d). However, the frequency of effector and effector memory CD8⁺ T cells were comparable in naive and

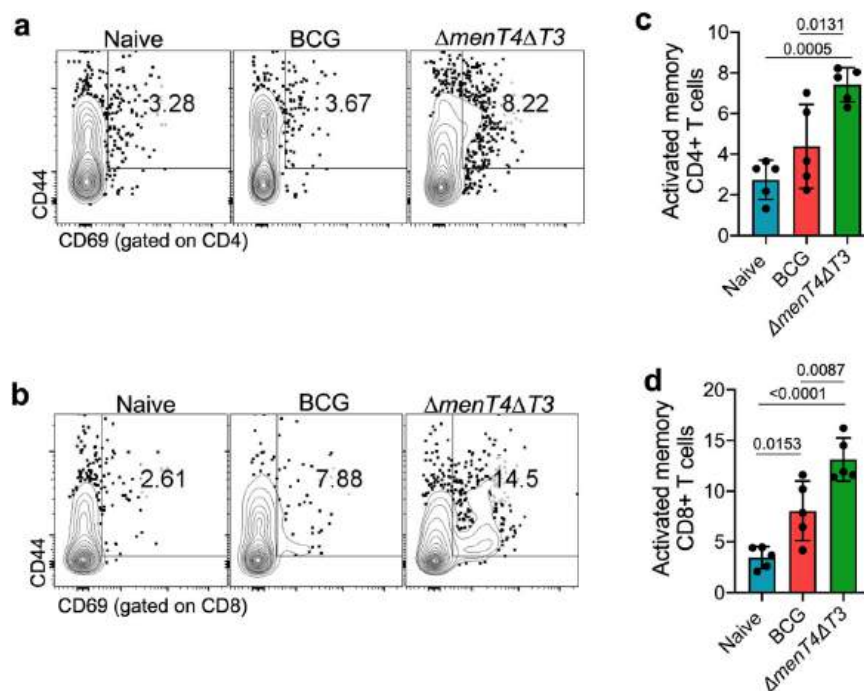


Fig. 6 | Immunization of mice with $\Delta menT4\Delta T3$ increases the expansion of activated memory T cell response. Representative FACS plots showing percentage frequency of CD4⁺ activated memory T_H cells (CD4⁺ CD44⁺ CD69⁺, **a**) and CD8⁺ activated memory T_C cells (CD8⁺ CD44⁺ CD69⁺, **b**) in spleens of naive or BCG or $\Delta menT4\Delta T3$ immunized C57BL/6 mice. These panels show the percentage

frequency of activated memory CD4⁺ T_H cells (**c**) and CD8⁺ T_C cells (**d**) in spleens of naive or BCG or $\Delta menT4\Delta T3$ immunized mice. The data shown in these panels are mean \pm SD of the percentage frequency of cells obtained from five animals from a single experiment. *p* values depicted on the graphs were assessed using one-way ANOVA. Source Data are provided as a Source Data file.

$\Delta menT4\Delta T3$ immunized mice (Fig. S9b, f, g). In comparison to BCG immunized mice, we observed a significant reduction in the proportion of central memory CD4⁺ and CD8⁺ T cells in $\Delta menT4\Delta T3$ immunized mice (Fig. S9a, b, e, h). The proportion of central memory CD4⁺ T cells was significantly reduced in $\Delta menT4\Delta T3$ immunized mice relative to naive mice (Fig. S9a, e). The frequency of effector CD4⁺ T cells, effector memory CD4⁺ and CD8⁺ T cells and central memory CD4⁺ and CD8⁺ T cells were comparable in naive and BCG immunized mice (Fig. S9a–e, g, h). Taken together, we show that immunization of mice with $\Delta menT4\Delta T3$ strain induces higher antigen-specific T_H1 response and expansion of activated memory T helper and cytotoxic T cell response in comparison to BCG immunized mice. These enhanced immune signatures might be associated with protection imparted by immunization with $\Delta menT4\Delta T3$ against *M. tuberculosis* challenge.

Discussion

TA systems are mostly bicistronic genetic elements that are widely distributed in prokaryotes and are involved in stress adaptation, genome maintenance, pathogenesis and control of phage infection. *M. tuberculosis* genome encodes for >90 TA pairs, and most of these belong to either type II or MenAT TA systems^{11,12,14}. TA systems belonging to type II subfamily have been extensively characterized in *M. tuberculosis*. However, very limited information is available about MenAT TA systems from *M. tuberculosis*. The three-dimensional structures of MenT1, MenT3 and MenT4 have been solved by X-ray crystallography, but their exact role in *M. tuberculosis* physiology and pathogenesis is still unknown^{29–31}. Superimposition of these solved structures revealed that MenT toxins have conserved folds and catalytic sites^{30,31}. In agreement with previous reports, we demonstrate that overexpression of MenT3 and MenT4 inhibits *E. coli* and *M. tuberculosis* growth^{29,30}. As expected, co-expression of cognate antitoxins or mutation of amino acid residues in the highly conserved motifs abrogated the growth inhibition activity associated with these toxins.

Studies have shown that MenT1, MenT3 and MenT4 homologs from *M. tuberculosis* possess NTase activity in vitro and inhibit protein synthesis by preventing aminoacylation of tRNAs^{30,31}.

Using temperature-sensitive mycobacteriophages, we generated *M. tuberculosis* mutant strains harboring deletions in either MenT3 or MenT4 or both MenT3 and MenT4. The growth patterns of single and double mutant strains were comparable to the parental strain. The relative abundance and upregulation of a subset of TA systems upon exposure to stress conditions and drugs suggests that these might function in a cumulative manner to enable *M. tuberculosis* to adapt to these conditions^{12,21,22}. We observed that MenT3 and MenT4 are mutually redundant, but both MenT3 and MenT4 cumulatively contribute to the adaptation of *M. tuberculosis* upon exposure to oxidative stress. Complementation of the double mutant strain with *menT3* partially restored the growth defect associated with the double mutant strain upon exposure to oxidative stress. We also observed that the relative transcript levels of *menA3*, *menT3*, *menA4* and *menT4* did not significantly change upon exposure to oxidative stress. It has been previously reported that in addition to their own promoter, antitoxins or TA complexes belonging to the type II subfamily can bind to other promoter sequences^{84–86}. We hypothesize that by binding to the promoter of genes involved in oxidative stress adaptation, MenAT3 and MenAT4 might regulate their expression. We also demonstrate that the survival of parental, $\Delta menT3$, $\Delta menT4$ and $\Delta menT4\Delta T3$ strains was similar after exposure to either nitrosative stress or nutritional stress or acidic stress.

Several studies have implicated the role of TA systems in the pathogenesis of various microorganisms. It has been shown that TA systems are essential for the virulence of bacterial pathogens such as *H. influenzae*, *V. cholerae*, *S. typhimurium*, *S. aureus*, and *M. tuberculosis*¹⁰. Here, we report that relative to the parental strain, $\Delta menT4\Delta T3$ strain was attenuated for growth at both acute and chronic stages of infection in guinea pigs. As observed in the case of

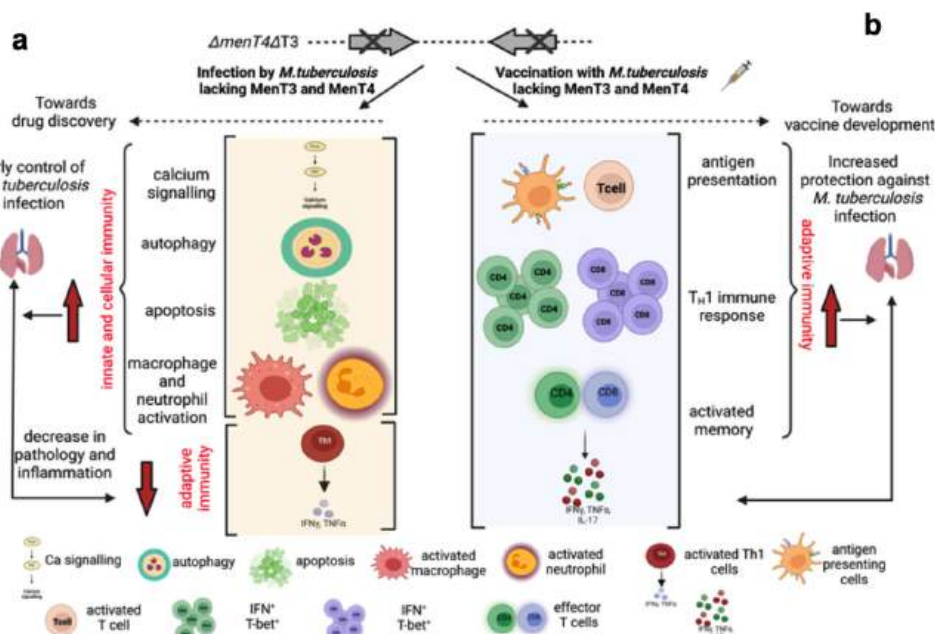


Fig. 7 | Proposed model for attenuation of $\Delta menT4\Delta T3$ in host tissues and for protection imparted by $\Delta menT4\Delta T3$ against *M. tuberculosis*. **a** In the present study, we show that deletion of *menT3* and *menT4* impairs the growth of *M. tuberculosis* in mice and guinea pigs. The attenuated phenotype of $\Delta menT4\Delta T3$ is most likely associated with increased levels of transcripts encoding for proteins involved in calcium signaling, autophagy, apoptosis and activation of macrophages and neutrophils. The increased expression of these pathways results in the generation of a robust innate immune response that restricts *M. tuberculosis* growth

and disease progression. **b** Here, we show that administration of $\Delta menT4\Delta T3$ imparts protection in mice and guinea pigs against challenge with *M. tuberculosis*. The immunization of mice with $\Delta menT4\Delta T3$ strain results in the expansion of activated memory immune response and induction of antigen-specific T $_H$ 1 in comparison to naive and BCG immunized mice. This significant increase in the generation of activated memory and T $_H$ 1 immune response might be associated with protection against *M. tuberculosis* challenge. The figure has been prepared using BioRender.

$\Delta mazF3\Delta 9\Delta 6$ or $\Delta vapC22$ or $\Delta higB1$ or $\Delta vapBC3$ or $\Delta vapBC4$ or $\Delta vapBC11$ or $\Delta menT2$, the growth defect associated with $\Delta menT4\Delta T3$ strain was more prominent in spleens and during the chronic stage of infection in guinea pigs^{21,23,25–27,35}. In agreement with guinea pig data, we observed that the deletion of *menT3* and *menT4* also impaired the growth of *M. tuberculosis* in mice tissues. As expected, we observed significantly reduced tissue damage in lung sections from guinea pigs infected with the double mutant strain in comparison to parental strain infected animals. We also observed that complementation with either *menT3* or *menT4* did not restore the growth defect associated with double mutant strain in host tissues. These findings imply that MenT3 and MenT4 are mutually redundant and that simultaneous deletion of both toxins results in an attenuated phenotype in vivo. However, based on the available data, the possibility of acquisition of secondary site mutation during the generation of $\Delta menT4\Delta T3$ can't be ruled out. In contrast to the in vivo phenotype, the growth patterns of both parental and $\Delta menT4\Delta T3$ strains were comparable in macrophages. A possible reason for the lack of growth defect in macrophages could be that the function of MenT3 and MenT4 lies outside macrophages, and these proteins are involved in the interaction or intracellular growth of *M. tuberculosis* inside other host cells such as lung epithelial cells, dendritic cells, adipocytes, neutrophils and mesenchymal stem cells^{87–91}.

Transcriptomics is widely used to gain a better understanding of the mechanisms for the attenuation of bacterial pathogens^{92–94}. Bacterial RNA sequencing revealed that transcript levels of genes encoding for proteins involved in stress adaptation and virulence were reduced in mid-log phase cultures of the double mutant strain as compared to the parental strain. Therefore, we hypothesize that the in vivo attenuated phenotype of the mutant strain might be associated with the reduced expression of these proteins. In order to further unravel the plausible mechanisms associated with the in vivo growth defect of the mutant strain, we also compared the transcriptional

profiles obtained from lung tissues of animals infected with either wild type or $\Delta menT4\Delta T3$ strain. Detailed analysis of the RNA-seq data revealed that the levels of transcripts encoding for proteins involved in calcium signaling, apoptosis and autophagy were increased in $\Delta menT4\Delta T3$ infected animals relative to parental strain infected animals (Fig. 7a). We also observed that the expression of proteins involved in inflammatory response was reduced in animals infected with the double mutant strain in comparison to parental strain infected animals (Fig. 7a). Taken together, the data suggests that the coordinated execution of these pathways might be associated with the observed growth defect of the mutant strain in host tissues.

Till date, BCG is the only licensed vaccine in use against TB. However, due to its limited efficacy, variable protection and adverse effects, there is an urgent need to develop new vaccine candidates that confer better protection against TB^{95–98}. There have been several reports regarding the development of attenuated mutant strains and evaluating their ability to impart protection against *M. tuberculosis* in animal models. The ability of these strains to impart protection is most likely due to the fact that they harbor a complete repertoire of genes encoding for immunodominant antigens. Given that $\Delta menT4\Delta T3$ was attenuated for growth in guinea pigs and Balb/c mice relative to the parental strain and was being further evaluated as a vaccine candidate, detailed immunological studies were performed in immunized C57BL/6 mice, a preferred model for immune studies. We observed that immunization of C57BL/6 mice with $\Delta menT4\Delta T3$ significantly reduced the lung bacterial burdens in comparison to naive mice at both 4- and 10 weeks post-infection. The observed protection was similar to the levels seen in BCG-immunized mice. However, the reduction in splenic bacterial counts at 10 weeks post-infection was statistically significant in comparison to bacterial loads observed in BCG-immunized mice. In agreement with mice protection data, we observed that immunization with $\Delta menT4\Delta T3$ was also able to impart protection against *M.*

tuberculosis in guinea pigs. The protection imparted upon immunization with $\Delta menT4\Delta T3$ at 4 weeks post-infection was significantly enhanced in comparison to protection observed in BCG-immunized guinea pigs. However, the levels of protection were comparable in $\Delta menT4\Delta T3$ and BCG-immunized guinea pigs at 8 weeks post-challenge. Interestingly, despite similar bacterial loads in lung tissues, analysis of H&E-stained lung sections revealed larger alveolar spaces and minimal cellular infiltration in lung sections of guinea pigs immunized with $\Delta menT4\Delta T3$ in comparison to BCG immunized animals. The levels of protection observed upon immunization of C57BL/6 and guinea pigs with $\Delta menT4\Delta T3$ were similar to those reported for other attenuated vaccine candidates such as $\Delta leuD$ (in guinea pigs) or $\Delta panCD$ (in guinea pigs) or $\Delta RD1\Delta panCD$ (in C57BL/6 mice)^{73,99,100}.

Several studies have shown that antigen-specific T_H1 response is desired to impart protection against *M. tuberculosis* challenge in C57BL/6 mice and guinea pigs^{76–78,81,101}. Previous studies have shown that protective immunity against TB depends on an acquired cellular immune response involving T-cell subsets, and a T_H1 -type response is considered favorable in imparting protection against *M. tuberculosis*¹⁰². In agreement, we observed significant upregulation of IFN- γ and T-bet expression in CD4⁺ and CD8⁺ T cell compartments in $\Delta menT4\Delta T3$ immunized mice in comparison to BCG-immunized mice. This T_H1 skewed response might be associated with the increased protection imparted by $\Delta menT4\Delta T3$ against *M. tuberculosis* challenge in spleen tissues. Next in order to further understand the immune correlates of protection in the $\Delta menT4\Delta T3$ immunized mice, we also evaluated the antigen-specific effector and memory T cell response in immunized mice. We observed increased activated memory T cell response in $\Delta menT4\Delta T3$ immunized mice as compared to BCG immunized or naive mice. Since memory responses are desirable for vaccine-induced long-lasting protection, we speculate that increased activated memory T cell response, as observed in $\Delta menT4\Delta T3$ immunized mice, might be able to impart protection against relapses as well. It is well documented that T_H1 immune responses are necessary for host defence against TB^{103–105}. We also observed a significant increase in the secretion of T_H1 cytokines such as IFN- γ , TNF- α and IL-2 in culture supernatants of PPD stimulated splenocytes from $\Delta menT4\Delta T3$ immunized mice, in agreement with the flow cytometry data. Studies have shown that IFN- γ and TNF- α are important for the effective control of *M. tuberculosis* infection¹⁰⁶. IL-2 has also been shown to stimulate the growth of B-cells, T-cells and NK cells and is essential for cellular immunity and granuloma formation in *M. tuberculosis* infection¹⁰⁶. We propose that increased amounts of these cytokines in culture supernatants from PPD stimulated splenocytes from $\Delta menT4\Delta T3$ immunized mice might contribute to its ability to impart protection against *M. tuberculosis* challenge^{81,107–110}. However, limitations of the present study include lack of experiments to study immunological responses in guinea pigs, and a small number of animals were utilized in mice experiments.

Overall, this study reveals that although MenT3 and MenT4 are dispensable for in vitro growth, these toxins function in a cumulative manner and are essential for *M. tuberculosis* to establish disease in mice and guinea pigs. We also show that immunization with $\Delta menT4\Delta T3$ is able to impart protection against *M. tuberculosis* in mice and guinea pigs. We propose that the protection observed in $\Delta menT4\Delta T3$ immunized animals is most likely associated with increased antigen-specific T_H1 biased and activated memory immune response (Fig. 7b). This study also provides the rationale for the development of live vaccines against TB based on the inactivation of virulence-associated pathways regulated by MenT3 and MenT4. Future studies include (1) unmarking and construction of $\Delta menT4\Delta T3$ -based multiple-allele mutant strains (such as *panCD*, *leuD*, *metX*, etc.), and these strains would be evaluated for safety and efficacy studies in compliance with the Geneva consensus¹¹¹, (2) identification of small molecule inhibitors against MenT3 and MenT4

proteins and (3) experiments to validate RNA seq data obtained from infected lung tissues.

Methods

Ethics approval

Ethics approval for this work was obtained from the Institutional Biosafety Committee and Review Committee on Genetic Manipulation of the Department of Biotechnology, Ministry of Science and Technology, Government of India.

Bacterial strains, plasmids, and culture conditions

The list of strains and plasmids used in the study are listed in Supplementary Table 1. The list of primers used in the study are listed in Supplementary Table 2. For overexpression studies, genes encoding for MenT3, MenT4 and their point mutants were PCR amplified and cloned in either isopropyl thio- β -galactoside (IPTG)-or anhydrotetracycline (Atc) inducible vectors, pET28b or pTetR, respectively¹¹². The recombinant constructs were verified by DNA sequencing. For co-expression studies, the toxin (*menT3* or *menT4*) and antitoxin (*menA2* or *menA3* or *menA4*) were separately cloned into MCS-1 and MCS-2 of the pETDuet vector¹¹³. The bacterial strains were cultured in either LB broth or LB agar or 7H9 or 7H11 medium as previously described¹¹⁴.

Growth inhibition assays in *E. coli* and *M. tuberculosis*

In order to determine whether inducible expression of MenT3 and MenT4 results in growth inhibition of *E. coli*, BL-21 (λ DE3, pLysS) was transformed with pET28b or pETDuet derivatives. The expression of proteins in recombinant *E. coli* strains was induced by the addition of 1.0 mM IPTG when OD_{600nm} of 0.4–0.6 was attained. The growth of recombinant strains was assayed by either measuring OD_{600nm} or by spotting diluted cultures on LB agar plates. For growth inhibition studies in *M. tuberculosis*, pTetR or pTetR-*menT3* or pTetR-*menT4* were electroporated in *M. tuberculosis* H₃₇Rv. The expression of MenT3 and MenT4 in early-log phase cultures (OD_{600nm} ~0.2) of recombinant strains was induced by the addition of 50 ng/ml Atc. The growth of parental and recombinant *M. tuberculosis* strains was determined by measuring OD_{600nm} and bacterial numbers at regular intervals. For CFU enumeration, 10.0-fold serial dilutions were prepared and plated on MB7H11 medium at 37 °C for 3–4 weeks.

Construction of various mutant and complemented strains of *M. tuberculosis*

The single and double mutant strains of *M. tuberculosis* Erdman were generated using temperature-sensitive mycobacteriophages¹¹⁵. Briefly, for the construction of $\Delta menT4$ strain, ~800 bp upstream and downstream region of *menT4* was PCR amplified and cloned into cosmid vector, pYUB854¹¹⁵. The recombinant pYUB854- $\Delta menT4$ was *Pac* I digested and packaged into phagemid, pYUB159. The recombinant phagemid was electroporated in *M. smegmatis* to generate temperature-sensitive mycobacteriophages. These temperature-sensitive mycobacteriophages were used to transduce mid-log phase cultures of *M. tuberculosis* Erdman (OD_{600nm} ~0.8–1.0) to generate $\Delta menT4$ strain. For the generation of $\Delta menT3$ and $\Delta menT4\Delta T3$ double mutant strain, ~800 bp upstream and downstream region of *menT3* was PCR amplified and cloned into cosmid vector, pYUB854. The hygromycin resistance gene pYUB854- $\Delta menT3$ was replaced with the kanamycin resistance gene resulting in pYUB854- $\Delta menT3$ -kan. The recombinant cosmid, pYUB854- $\Delta menT3$ -kan, was packaged, and temperature-sensitive mycobacteriophages were prepared as described above. For the construction of $\Delta menT3$ and $\Delta menT4\Delta T3$, mid-log phase cultures of *M. tuberculosis* Erdman or $\Delta menT4$ strain (OD_{600nm} ~0.8–1.0), respectively, were transduced with temperature-sensitive *menT3* mycobacteriophages. The replacement of *menT3* and *menT4* with kanamycin and hygromycin resistance gene, respectively, in $\Delta menT4\Delta T3$ strain of *M. tuberculosis* Erdman was verified by PCR and

whole genome sequencing. In order to complement the $\Delta menT4\Delta T3$ strain, *menA3-menT3* and *menA4-menT4* locus were PCR amplified along with 500 bp upstream region and cloned into pMV306-apramycin. The recombinant construct was electroporated into $\Delta menT4\Delta T3$ and transformants were selected on MB7H11 plates containing kanamycin, hygromycin and apramycin.

Stress experiments

For oxidative stress, early-log phase cultures of various strains ($OD_{600nm} \sim 0.2$) were exposed to 5 mM H_2O_2 for either 24 or 72 h. For acidic or nitrosative stress, early log phase cultures were harvested by centrifugation, washed twice and resuspended in MB7H9 medium, pH-5.2 (acidic medium) for 7 days or in the presence of 5 mM $NaNO_2$ (nitrosative stress for 24 h). For nutritional stress, early-log phase cultures were harvested, washed twice and resuspended in 1x tris-buffered saline tween-80 for 7 days. At designated time points, CFU enumeration was performed by plating 10.0-fold serial dilutions on MB7H11 agar plates at 37 °C for 3–4 weeks.

Macrophage experiments

Human monocyte cell-line THP-1 was obtained from National Centre for Cell Science and cultured in Roswell Park Memorial Institute (RPMI) 1640 medium and differentiated into macrophages by overlaying cells with RPMI medium with 20 ng/ml of phorbol myristate acetate (PMA) for 24 h. For macrophage experiments, differentiated THP-1 cells (2×10^5 per well) were infected with various strains at a MOI of 1:10 for 4 h. Subsequently, macrophages were washed with 1x PBS, cultured in RPMI medium containing 200 μ g/ml amikacin for 2 h to remove extracellular bacteria and overlaid with RPMI complete medium. The medium was replaced every 48 h during the experiment. At designated time points, macrophages were lysed using 1x PBS containing 0.1% triton X-100. The number of viable bacteria in lysates was determined by plating 10.0-fold serial dilutions on MB7H11 agar at 37 °C for 3–4 weeks.

Lipid extraction experiments

Briefly, various strains were grown to mid-log phase ($OD_{600nm} \sim 0.8$ –1.0). The cultures were harvested by centrifugation and washed twice with 1x PBS. Subsequently, apolar and polar lipids were extracted as previously described³⁵. An equal amount of different lipid fractions was loaded on silica plates and resolved using one-dimensional TLC in the different solvent systems as described previously³⁵. Different lipids were visualized by staining the TLC with 5% molybdophosphoric acid in ethanol and subsequent charring at 100 °C. TLC images were acquired using a gel documentation system (Bio-Rad).

Bacterial RNA sequencing

For bacterial RNA-seq experiments, total RNA was isolated from mid-log phase cultures ($OD_{600nm} \sim 0.8$ –1.0) of various strains using the Trizol method as previously described¹¹⁴. The quality of the isolated RNA was analyzed using Agilent Bioanalyzer. RNA samples were further processed for library preparation and sequenced using the Illumina HiSeq2000 platform. The sequenced reads were aligned to the *M. tuberculosis* Erdman sequence using the Hisat 2 program (Version 2.0.5). The differential gene expression analysis using aligned reads was performed using the Cuffdiff program of the Cufflinks package.

Animal husbandry

Six to eight weeks old outbred female Duncan Hartley guinea pigs (~250–300 g) were obtained from Disease Free Small Animal House, Lala Lajpat Rai University of Veterinary and Animal Sciences, Hisar. Six to eight weeks old inbred female Balb/c and C57BL/6 mice (~20–25 g) were obtained from the Experimental Animal Facility, NCR Biotech Science Cluster, Faridabad. Animals were housed in a group of either 5

(mice) or 3 (guinea pigs) in individually ventilated cages in BSL-3 labs. The animals were maintained at a room temperature of 22 ± 3 °C, relative humidity of 30 to 70%, 15–20 air changes/h, light intensity of 325–350 lux with a 14 h light/10 h dark cycle and noise intensity of <85 db. A sterilized pellet diet (Altromin International, Germany) was offered ad libitum to the animals throughout the experimental period. Ad libitum aqua guard filtered, and autoclaved water was served in bottles fitted with stainless steel nozzles.

Animal virulence studies

The institutional animal ethics committee of the Translational Health Science and Technology Institute (THSTI) approved the animal experiments. The animal experiments were performed as per the guidelines provided by the committee for the control and supervision of experiments on animals. For aerosol infections, mid-log phase cultures ($OD_{600nm} \sim 0.8$ –1.0) of various strains were harvested by centrifugation and washed twice with 1x PBS. Subsequently, single-cell suspensions were prepared, and cultures were diluted to 5×10^8 CFU (female Balb/c mice) or 1×10^8 CFU (female Duncan Hartley strain, guinea pigs) in 10 ml saline. The animals were infected using a Glass-col aerosol generation device that implanted ~100 bacilli in lung tissues. For CFU analysis, lungs and spleens were homogenized in saline, 10.0-fold serial dilutions were prepared and plated on MB7H11 agar for 3–4 weeks at 37 °C. For histopathology analysis, lung tissues were fixed in 10% formalin, embedded in paraffin wax and stained with hematoxylin and eosin (H&E). The stained sections were analyzed for tissue damage by a histopathologist. The total granuloma score in H&E-stained lung sections from infected guinea pigs was determined as described earlier¹¹⁶.

Host RNA-seq analysis

For host RNA-seq analysis, total RNA was isolated from lung tissues of uninfected Balb/c mice and those infected with either wild type or $\Delta menT4\Delta T3$ at 4 weeks post-infection using Qiagen RNA extraction protocol as per manufacturer recommendations²⁶. RNA was subjected to DNase I treatment, and the quality and integrity of RNA were analyzed using Agilent Bioanalyzer and subjected to sequencing. The paired-end reads obtained were analyzed for quality control using the NGS QC Toolkit, and those with a Phred score of >Q30 were carried forward for analysis. HISAT2 splice-aware read aligner was used for the alignment of the passed reads to the reference *Mus musculus* (mm10) genome. Stringtie was employed for the assembly and quantification of the aligned reads of all samples. Analysis for differential expression was performed using DESeq2. The heat maps were prepared using TB tools.

Protective efficacy studies

For immunization experiments, female mice (C57BL/6) or female guinea pigs (Duncan Hartley strain) were immunized with either saline or single-cell suspension containing 5×10^5 CFU of BCG or $\Delta menT4\Delta T3$ strain via subcutaneous route in mice or 1×10^5 CFU via intradermal route in guinea pigs. For protection studies, at 10 weeks post-immunization, animals were challenged with *M. tuberculosis* H₃₇Rv using a Glass Col aerosol chamber as described above. The protective efficacy imparted by immunization with either BCG or $\Delta menT4\Delta T3$ was determined by bacterial enumeration and histopathological analysis as described above.

Flow cytometry experiments

At 6 weeks post-immunization spleens from naive and immunized C57BL/6 mice were isolated and passed through a 70 μ m cell strainer to obtain a single-cell suspension. Subsequently, RBCs were lysed with ice-cold ammonium-chloride-potassium (ACK) lysis buffer (20–30 s at room temperature) and resuspended in RPMI complete media. For immunophenotyping experiments, splenocytes were seeded in a 96-

well plate (2×10^5 cells per well). The splenocytes were stimulated with $10 \mu\text{g/ml}$ purified protein derivative (PPD) for 72 h. Thereafter, cells were harvested, washed and incubated with anti-CD16/CD32 Fc block for 15 min. The cells were stained for surface markers with Live-Dead dye-BV421, anti-mouse: CD45.2-APC-Cy7, anti-CD4-PerCp-Cy5.5, anti-CD8-PE, anti-CD62L-APC, anti-CD44-PE-Cy7 and anti-CD69-FITC, for 30 min at 4°C (BD Biosciences, Supplementary Table 3). For intracellular staining of cytokine and transcription factor, single cells of PPD-stimulated splenocytes were additionally treated with Golgi stop containing Brefeldin A (BD Biosciences) for 6 h before the completion of the incubation as previously described^{117,118}. Following this, cells were harvested, washed, incubated for 20 min with anti-CD16/CD32 Fc block and stained with Live-Dead dye-Cy7, anti-CD4-PerCp-Cy5.5 and anti-CD8-BV510 for 1 h. Subsequently, intracellular staining of cells was performed using a cytofix/cytoperm kit with anti-IFN- γ -PE, anti-IL-17A-PE-Cy7, anti-T-bet-APC and anti-Foxp3-BV421 (Supplementary Table 3)¹¹⁹. The stained samples were washed twice with ice-cold 1x PBS, resuspended in FACS staining buffer and acquired on BD Canto II (BD Biosciences). The acquired data were analyzed using Flow Jo (Treestar) software version X.

ELISA experiments

Splenocytes from immunized C57BL/6 mice were seeded at a density of 2×10^5 cells per well in a 96-well plate and stimulated with $10 \mu\text{g/ml}$ PPD for 72 h. The levels of IFN- γ , TNF- α , IL-2 and IL-17A in supernatants of PPD-stimulated splenocytes were measured by ELISA as per the manufacturer's recommendations.

Statistical analysis

The statistical tests and graphs were prepared using GraphPad Prism (Version 9.5.1). The statistical tests used for data analysis are mentioned in the respective figure legends. The statistical analysis of RNA-seq data was performed using the Negative Binomial Wald test. * $p < 0.05$, ** $p < 0.01$, *** $p < 0.001$ and **** $p < 0.0001$ were considered statistically significant.

Reporting summary

Further information on research design is available in the Nature Portfolio Reporting Summary linked to this article.

Data availability

The RNA-seq data generated in the study have been deposited in NCBI-SRA repositories under accession code Bioproject [PRJNA997775](https://www.ncbi.nlm.nih.gov/bioproject/PRJNA997775) for *Mus musculus* and [PRJNA997818](https://www.ncbi.nlm.nih.gov/bioproject/PRJNA997818) for *M. tuberculosis*. Source data are provided with this paper.

References

- Harms, A., Brodersen, D. E., Mitarai, N. & Gerdes, K. Toxins, targets, and triggers: an overview of toxin-antitoxin biology. *Mol. Cell* **70**, 768–784 (2018).
- Jurenas, D., Fraikin, N., Goormaghtigh, F. & Van Melderen, L. Biology and evolution of bacterial toxin-antitoxin systems. *Nat. Rev. Microbiol.* **20**, 335–350 (2022).
- Qiu, J., Zhai, Y., Wei, M., Zheng, C. & Jiao, X. Toxin-antitoxin systems: classification, biological roles, and applications. *Microbiol. Res.* **264**, 127159 (2022).
- Page, R. & Peti, W. Toxin-antitoxin systems in bacterial growth arrest and persistence. *Nat. Chem. Biol.* **12**, 208–214 (2016).
- Song, S. & Wood, T. K. Toxin/antitoxin system paradigms: toxins bound to antitoxins are not likely activated by preferential antitoxin degradation. *Adv. Biosyst.* **4**, e1900290 (2020).
- Unterholzner, S. J., Poppenberger, B. & Rozhon, W. Toxin-antitoxin systems: biology, identification, and application. *Mob. Genet. Elem.* **3**, e26219 (2013).
- Sarpong, D. D. & Murphy, E. R. RNA regulated toxin-antitoxin systems in pathogenic bacteria. *Front. Cell Infect. Microbiol.* **11**, 661026 (2021).
- Singh, G., Yadav, M., Ghosh, C. & Rathore, J. S. Bacterial toxin-antitoxin modules: classification, functions, and association with persistence. *Curr. Res. Micro. Sci.* **2**, 100047 (2021).
- Zhang, S.-P. et al. Type II toxin-antitoxin system in bacteria: activation, function, and mode of action. *Biophys. Rep.* **6**, 68–79 (2020).
- Lobato-Marquez, D., Diaz-Orejas, R. & Garcia-Del Portillo, F. Toxin-antitoxins and bacterial virulence. *FEMS Microbiol. Rev.* **40**, 592–609 (2016).
- Akarsu, H. et al. TASmania: a bacterial toxin-antitoxin systems database. *PLoS Comput. Biol.* **15**, e1006946 (2019).
- Ramage, H. R., Connolly, L. E. & Cox, J. S. Comprehensive functional analysis of Mycobacterium tuberculosis toxin-antitoxin systems: implications for pathogenesis, stress responses, and evolution. *PLoS Genet.* **5**, e1000767 (2009).
- Sala, A., Bordes, P. & Genevaux, P. Multiple toxin-antitoxin systems in Mycobacterium tuberculosis. *Toxins* **6**, 1002–1020 (2014).
- Tandon, H. et al. Bioinformatic and mutational studies of related toxin-antitoxin pairs in Mycobacterium tuberculosis predict and identify key functional residues. *J. Biol. Chem.* **294**, 9048–9063 (2019).
- Schifano, J. M. et al. Mycobacterial toxin MazF-mt6 inhibits translation through cleavage of 23S rRNA at the ribosomal A site. *Proc. Natl Acad. Sci. USA* **110**, 8501–8506 (2013).
- Chattopadhyay, G. et al. Functional and biochemical characterization of the MazEF6 toxin-antitoxin system of Mycobacterium tuberculosis. *J. Bacteriol.* **204**, e0005822 (2022).
- Winther, K., Tree, J. J., Tollervey, D. & Gerdes, K. VapCs of Mycobacterium tuberculosis cleave RNAs essential for translation. *Nucleic Acids Res.* **44**, 9860–9871 (2016).
- Freire, D. M. et al. An NAD(+) phosphorylase toxin triggers Mycobacterium tuberculosis cell death. *Mol. Cell* **73**, 1282–1291.e8 (2019).
- Gupta, M. et al. The chromosomal parDE2 toxin-antitoxin system of Mycobacterium tuberculosis H37Rv: genetic and functional characterization. *Front. Microbiol.* **7**, 886 (2016).
- Deep, A. et al. Structural insights into DarT toxin neutralization by cognate DarG antitoxin: ssDNA mimicry by DarG C-terminal domain keeps the DarT toxin inhibited. *Structure* **31**, 780–789.e4 (2023).
- Agarwal, S. et al. System-wide analysis unravels the differential regulation and in vivo essentiality of virulence-associated proteins B and C toxin-antitoxin systems of Mycobacterium tuberculosis. *J. Infect. Dis.* **217**, 1809–1820 (2018).
- Gupta, A., Venkataraman, B., Vasudevan, M. & Gopinath Bankar, K. Co-expression network analysis of toxin-antitoxin loci in Mycobacterium tuberculosis reveals key modulators of cellular stress. *Sci. Rep.* **7**, 5868 (2017).
- Deep, A. et al. Structural, functional and biological insights into the role of Mycobacterium tuberculosis VapBC11 toxin-antitoxin system: targeting a tRNase to tackle mycobacterial adaptation. *Nucleic Acids Res.* **46**, 11639–11655 (2018).
- Sharma, A. et al. VapC21 toxin contributes to drug-tolerance and interacts with non-cognate VapB32 antitoxin in Mycobacterium tuberculosis. *Front. Microbiol.* **11**, 2037 (2020).
- Tiwari, P. et al. MazF ribonucleases promote Mycobacterium tuberculosis drug tolerance and virulence in guinea pigs. *Nat. Commun.* **6**, 6059 (2015).
- Agarwal, S. et al. VapBC22 toxin-antitoxin system from Mycobacterium tuberculosis is required for pathogenesis and modulation of host immune response. *Sci. Adv.* **6**, eaba6944 (2020).

27. Sharma, A. et al. HgB1 toxin in *Mycobacterium tuberculosis* is upregulated during stress and required to establish infection in guinea pigs. *Front. Microbiol.* **12**, 748890 (2021).
28. Cole, S. T. et al. Deciphering the biology of *Mycobacterium tuberculosis* from the complete genome sequence. *Nature* **393**, 537–544 (1998).
29. Yu, X. et al. Characterization of a toxin-antitoxin system in *Mycobacterium tuberculosis* suggests neutralization by phosphorylation as the antitoxicity mechanism. *Commun. Biol.* **3**, 216 (2020).
30. Cai, Y. et al. A nucleotidyltransferase toxin inhibits growth of *Mycobacterium tuberculosis* through inactivation of tRNA acceptor stems. *Sci. Adv.* **6**, eabb6651 (2020).
31. Xu, X. et al. MenT nucleotidyltransferase toxins extend tRNA acceptor stems and can be inhibited by asymmetrical antitoxin binding. *Nat. Commun.* **14**, 4644 (2023).
32. Keren, I., Minami, S., Rubin, E. & Lewis, K. Characterization and transcriptome analysis of *Mycobacterium tuberculosis* persisters. *mBio* **2**, e00100–e00111 (2011).
33. Singh, R., Barry, C. E. 3rd & Boshoff, H. I. The three RelE homologs of *Mycobacterium tuberculosis* have individual, drug-specific effects on bacterial antibiotic tolerance. *J. Bacteriol.* **192**, 1279–1291 (2010).
34. Zaveri, A. et al. Depletion of the DarG antitoxin in *Mycobacterium tuberculosis* triggers the DNA-damage response and leads to cell death. *Mol. Microbiol.* **114**, 641–652 (2020).
35. Gosain, T. P., Singh, M., Singh, C., Thakur, K. G. & Singh, R. Disruption of MenT2 toxin impairs the growth of *Mycobacterium tuberculosis* in guinea pigs. *Microbiology* **168**, 001246 (2022).
36. Lamichhane, G., Tyagi, S. & Bishai, W. R. Designer arrays for defined mutant analysis to detect genes essential for survival of *Mycobacterium tuberculosis* in mouse lungs. *Infect. Immun.* **73**, 2533–2540 (2005).
37. Sassetti, C. M. & Rubin, E. J. Genetic requirements for mycobacterial survival during infection. *Proc. Natl Acad. Sci. USA* **100**, 12989–12994 (2003).
38. He, H., Bretl, D. J., Penoske, R. M., Anderson, D. M. & Zahrt, T. C. Components of the Rv0081-Rv0088 locus, which encodes a predicted formate hydrogenlyase complex, are coregulated by Rv0081, MprA, and DosR in *Mycobacterium tuberculosis*. *J. Bacteriol.* **193**, 5105–5118 (2011).
39. Sun, X. et al. Transcription factors Rv0081 and Rv3334 connect the early and the enduring hypoxic response of *Mycobacterium tuberculosis*. *Virulence* **9**, 1468–1482 (2018).
40. Mehra, A. et al. *Mycobacterium tuberculosis* type VII secreted effector EsxH targets host ESCRT to impair trafficking. *PLoS Pathog.* **9**, e1003734 (2013).
41. DeJesus, M. A. et al. Comprehensive essentiality analysis of the *Mycobacterium tuberculosis* genome via saturating transposon mutagenesis. *mBio* **8**, e02133–16 (2017).
42. Garg, R. et al. The conserved hypothetical protein Rv0574c is required for cell wall integrity, stress tolerance, and virulence of *Mycobacterium tuberculosis*. *Infect. Immun.* **83**, 120–129 (2015).
43. Jia, Q. et al. Universal stress protein Rv2624c alters abundance of arginine and enhances intracellular survival by ATP binding in mycobacteria. *Sci. Rep.* **6**, 35462 (2016).
44. Ahmed, M. et al. *Mycobacterium tuberculosis* senses host Interferon-gamma via the membrane protein MmpL10. *Commun. Biol.* **5**, 1317 (2022).
45. Domenech, P. & Reed, M. B. Rapid and spontaneous loss of phthiocerol dimycocerosate (PDIM) from *Mycobacterium tuberculosis* grown in vitro: implications for virulence studies. *Microbiology* **155**, 3532–3543 (2009).
46. Harr, M. W. & Distelhorst, C. W. Apoptosis and autophagy: decoding calcium signals that mediate life or death. *Cold Spring Harb. Perspect. Biol.* **2**, a005579 (2010).
47. Tang, W. et al. Adenylyl cyclase 1 as a major isoform to generate cAMP signaling for apoA-1-mediated cholesterol efflux pathway. *J. Lipid Res.* **59**, 635–645 (2018).
48. Russell, D. G., Cardona, P. J., Kim, M. J., Allain, S. & Altare, F. Foamy macrophages and the progression of the human tuberculosis granuloma. *Nat. Immunol.* **10**, 943–948 (2009).
49. Vergne, I. et al. Autophagy in immune defense against *Mycobacterium tuberculosis*. *Autophagy* **2**, 175–178 (2006).
50. Parys, J. B., Decuypere, J. P. & Bultynck, G. Role of the inositol 1,4,5-trisphosphate receptor/Ca²⁺-release channel in autophagy. *Cell Commun. Signal* **10**, 17 (2012).
51. Joseph, S. K. & Hajnoczky, G. IP₃ receptors in cell survival and apoptosis: Ca²⁺ release and beyond. *Apoptosis* **12**, 951–968 (2007).
52. Jayachandran, R. et al. Survival of mycobacteria in macrophages is mediated by coronin 1-dependent activation of calcineurin. *Cell* **130**, 37–50 (2007).
53. Parihar, S. P. et al. Protein kinase C-delta (PKCdelta), a marker of inflammation and tuberculosis disease progression in humans, is important for optimal macrophage killing effector functions and survival in mice. *Mucosal Immunol.* **11**, 579–580 (2018).
54. Hubbard, K. B. & Hepler, J. R. Cell signalling diversity of the Gqalpha family of heterotrimeric G proteins. *Cell Signal.* **18**, 135–150 (2006).
55. Niu, H. & Deng, M. Editorial: The role of autophagy in infectious diseases. *Front. Cell Infect. Microbiol.* **12**, 1039282 (2022).
56. Gutierrez, M. G. et al. Autophagy is a defense mechanism inhibiting BCG and *Mycobacterium tuberculosis* survival in infected macrophages. *Cell* **119**, 753–766 (2004).
57. Szyniarowski, P. et al. A comprehensive siRNA screen for kinases that suppress macroautophagy in optimal growth conditions. *Autophagy* **7**, 892–903 (2011).
58. Niikura, Y., Dixit, A., Scott, R., Perkins, G. & Kitagawa, K. BUB1 mediation of caspase-independent mitotic death determines cell fate. *J. Cell Biol.* **178**, 283–296 (2007).
59. Wang, Z. et al. PHF23 (plant homeodomain finger protein 23) negatively regulates cell autophagy by promoting ubiquitination and degradation of E3 ligase LRSAM1. *Autophagy* **10**, 2158–2170 (2014).
60. Golovkine, G. R. et al. Autophagy restricts *Mycobacterium tuberculosis* during acute infection in mice. *Nat. Microbiol.* **8**, 819–832 (2023).
61. Zhang, W. et al. IL-6 promotes PD-L1 expression in monocytes and macrophages by decreasing protein tyrosine phosphatase receptor type O expression in human hepatocellular carcinoma. *J. Immunother. Cancer* **8**, e000285 (2020).
62. Liu, X. et al. Wingless homolog Wnt11 suppresses bacterial invasion and inflammation in intestinal epithelial cells. *Am. J. Physiol. Gastrointest. Liver Physiol.* **301**, G992–G1003 (2011).
63. Kishi, H. et al. Role of chemokine C-C motif ligand-1 in acute and chronic pulmonary inflammations. *Springerplus* **5**, 1241 (2016).
64. Kumar, N. P. et al. Plasma chemokines are biomarkers of disease severity, higher bacterial burden and delayed sputum culture conversion in pulmonary tuberculosis. *Sci. Rep.* **9**, 18217 (2019).
65. Nouailles, G. et al. CXCL5-secreting pulmonary epithelial cells drive destructive neutrophilic inflammation in tuberculosis. *J. Clin. Invest.* **124**, 1268–1282 (2014).
66. Chang, J. W., Koike, T. & Iwashima, M. hnRNP-K is a nuclear target of TCR-activated ERK and required for T-cell late activation. *Int. Immunol.* **21**, 1351–1361 (2009).
67. Xiong, X. et al. SAG/RBX2 E3 ubiquitin ligase differentially regulates inflammatory responses of myeloid cell subsets. *Front. Immunol.* **9**, 2882 (2018).
68. Moraes-Vieira, P. M. et al. RBP4 activates antigen-presenting cells, leading to adipose tissue inflammation and systemic insulin resistance. *Cell Metab.* **19**, 512–526 (2014).

69. Yamaguchi, M., Samuchiwal, S. K., Quehenberger, O., Boyce, J. A. & Balestrieri, B. Macrophages regulate lung ILC2 activation via Pla2g5-dependent mechanisms. *Mucosal Immunol.* **11**, 615–626 (2018).
70. Rubio, J. M. et al. Group V secreted phospholipase A2 is upregulated by IL-4 in human macrophages and mediates phagocytosis via hydrolysis of ethanolamine phospholipids. *J. Immunol.* **194**, 3327–3339 (2015).
71. Schneider, B. E. et al. Lysosomal phospholipase A2: a novel player in host immunity to *Mycobacterium tuberculosis*. *Eur. J. Immunol.* **44**, 2394–2404 (2014).
72. Martinot, A. J. et al. Protective efficacy of an attenuated Mtb DeltaLprG vaccine in mice. *PLoS Pathog.* **16**, e1009096 (2020).
73. Sambandamurthy, V. K. et al. A pantothenate auxotroph of *Mycobacterium tuberculosis* is highly attenuated and protects mice against tuberculosis. *Nat. Med.* **8**, 1171–1174 (2002).
74. Gonzalo-Asensio, J., Marinova, D., Martin, C. & Aguilo, N. MTBVAC: attenuating the human pathogen of tuberculosis (TB) toward a promising vaccine against the TB epidemic. *Front. Immunol.* **8**, 1803 (2017).
75. Silva, F. et al. Mouse subcutaneous BCG vaccination and *Mycobacterium tuberculosis* infection alter the lung and gut microbiota. *Microbiol. Spectr.* **10**, e0169321 (2022).
76. Weinrich Olsen, A., van Pinxteren, L. A., Meng Okkels, L., Birk Rasmussen, P. & Andersen, P. Protection of mice with a tuberculosis subunit vaccine based on a fusion protein of antigen 85b and esat-6. *Infect. Immun.* **69**, 2773–2778 (2001).
77. Hanna, C. C. et al. Synthetic protein conjugate vaccines provide protection against *Mycobacterium tuberculosis* in mice. *Proc. Natl Acad. Sci. USA* **118**, e2013730118 (2021).
78. Khan, A. et al. A recombinant bovine adenoviral mucosal vaccine expressing mycobacterial antigen-85B generates robust protection against tuberculosis in mice. *Cell Rep. Med.* **2**, 100372 (2021).
79. Jia, Q., Masleša-Galić, S., Nava, S. & Horwitz, M. A. Listeria-vectored multi-antigenic tuberculosis vaccine protects C57BL/6 and BALB/c mice and guinea pigs against *Mycobacterium tuberculosis* challenge. *Commun. Biol.* **5**, 1388 (2022).
80. Zeng, M., Nourishirazi, E., Guinet, E. & Nouri-Shirazi, M. The genetic background influences the cellular and humoral immune responses to vaccines. *Clin. Exp. Immunol.* **186**, 190–204 (2016).
81. Lyadova, I. V. & Panteleev, A. V. Th1 and Th17 cells in tuberculosis: protection, pathology, and biomarkers. *Mediators Inflamm.* **2015**, 854507 (2015).
82. Jaron, B., Maranghi, E., Leclerc, C. & Majlessi, L. Effect of attenuation of Treg during BCG immunization on anti-mycobacterial Th1 responses and protection against *Mycobacterium tuberculosis*. *PLoS ONE* **3**, e2833 (2008).
83. Scott-Browne, J. P. et al. Expansion and function of Foxp3-expressing T regulatory cells during tuberculosis. *J. Exp. Med.* **204**, 2159–2169 (2007).
84. Wen, W. et al. Autoregulation and virulence control by the toxin-antitoxin system SavRS in *Staphylococcus aureus*. *Infect. Immun.* **86**, e00032–18 (2018).
85. Guo, Y. et al. Antitoxin HigA inhibits virulence gene mvfR expression in *Pseudomonas aeruginosa*. *Environ. Microbiol.* **21**, 2707–2723 (2019).
86. Sun, C. et al. MqsR/MqsA toxin/antitoxin system regulates persistence and biofilm formation in *pseudomonas putida* KT2440. *Front. Microbiol.* **8**, 840 (2017).
87. Lyadova, I. V. Neutrophils in tuberculosis: heterogeneity shapes the way? *Mediators Inflamm.* **2017**, 8619307 (2017).
88. Scordo, J. M., Knoell, D. L. & Torrelles, J. B. Alveolar epithelial cells in *Mycobacterium tuberculosis* infection: active players or innocent bystanders? *J. Innate Immun.* **8**, 3–14 (2016).
89. Khan, A. et al. Mesenchymal stem cells internalize *Mycobacterium tuberculosis* through scavenger receptors and restrict bacterial growth through autophagy. *Sci. Rep.* **7**, 15010 (2017).
90. Beigier-Bompadre, M. et al. *Mycobacterium tuberculosis* infection modulates adipose tissue biology. *PLoS Pathog.* **13**, e1006676 (2017).
91. Mihret, A. The role of dendritic cells in *Mycobacterium tuberculosis* infection. *Virulence* **3**, 654–659 (2012).
92. Robbe-Saule, M., Babonneau, J., Sismeiro, O., Marsollier, L. & Marion, E. An optimized method for extracting bacterial RNA from mouse skin tissue colonized by *Mycobacterium ulcerans*. *Front. Microbiol.* **8**, 512 (2017).
93. Lachmandas, E. et al. Metformin alters human host responses to *Mycobacterium tuberculosis* in healthy subjects. *J. Infect. Dis.* **220**, 139–150 (2019).
94. Nalpas, N. C. et al. RNA sequencing provides exquisite insight into the manipulation of the alveolar macrophage by tubercle bacilli. *Sci. Rep.* **5**, 13629 (2015).
95. McShane, H. Tuberculosis vaccines: beyond bacille Calmette-Guerin. *Philos. Trans. R. Soc. Lond. B Biol. Sci.* **366**, 2782–2789 (2011).
96. Netea, M. G. et al. Trained immunity: a program of innate immune memory in health and disease. *Science* **352**, aaf1098 (2016).
97. Sterne, J. A., Rodrigues, L. C. & Guedes, I. N. Does the efficacy of BCG decline with time since vaccination? *Int. J. Tuberc. Lung Dis.* **2**, 200–207 (1998).
98. Davenne, T. & McShane, H. Why don't we have an effective tuberculosis vaccine yet? *Expert Rev. Vaccines* **15**, 1009–1013 (2016).
99. Sampson, S. L. et al. Protection elicited by a double leucine and pantothenate auxotroph of *Mycobacterium tuberculosis* in guinea pigs. *Infect. Immun.* **72**, 3031–3037 (2004).
100. Sambandamurthy, V. K. et al. *Mycobacterium tuberculosis* DeltaRD1 DeltapanCD: a safe and limited replicating mutant strain that protects immunocompetent and immunocompromised mice against experimental tuberculosis. *Vaccine* **24**, 6309–6320 (2006).
101. Tree, J. A., Elmore, M. J., Javed, S., Williams, A. & Marsh, P. D. Development of a guinea pig immune response-related microarray and its use to define the host response following *Mycobacterium bovis* BCG vaccination. *Infect. Immun.* **74**, 1436–1441 (2006).
102. Barnes, P. & Vankayalapati, R. Th1 and Th2 cytokines in the human immune response to tuberculosis. *Tuberculosis and Tubercle Bacilli*, Ch. 31, 489–495 (2004) <https://doi.org/10.1128/9781555817657.ch31>.
103. Cardona, P. J. What we have learned and what we have missed in tuberculosis pathophysiology for a new vaccine design: searching for the “Pink Swan”. *Front. Immunol.* **8**, 556 (2017).
104. Cooper, A. M. et al. Disseminated tuberculosis in interferon gamma gene-disrupted mice. *J. Exp. Med.* **178**, 2243–2247 (1993).
105. Flynn, J. L. et al. An essential role for interferon gamma in resistance to *Mycobacterium tuberculosis* infection. *J. Exp. Med.* **178**, 2249–2254 (1993).
106. Domingo-Gonzalez, R., Prince, O., Cooper, A. & Khader, S. A. Cytokines and chemokines in *Mycobacterium tuberculosis* infection. *Microbiol. Spectr.* **4**, 5 (2016).
107. Behar, S. M., Woodworth, J. S. & Wu, Y. Next generation: tuberculosis vaccines that elicit protective CD8+ T cells. *Expert Rev. Vaccines* **6**, 441–456 (2007).
108. Zeng, G., Zhang, G. & Chen, X. Th1 cytokines, true functional signatures for protective immunity against TB? *Cell Mol. Immunol.* **15**, 206–215 (2018).

109. Choi, H. G. et al. Antigen-specific IFN-gamma/IL-17-co-producing CD4(+) T-cells are the determinants for protective efficacy of tuberculosis subunit vaccine. *Vaccines* **8**, 300 (2020).
110. Pitt, J. M. et al. Blockade of IL-10 signaling during bacillus Calmette-Guerin vaccination enhances and sustains Th1, Th17, and innate lymphoid IFN-gamma and IL-17 responses and increases protection to Mycobacterium tuberculosis infection. *J. Immunol.* **189**, 4079–4087 (2012).
111. Kamath, A. T. et al. New live mycobacterial vaccines: the Geneva consensus on essential steps towards clinical development. *Vaccine* **23**, 3753–3761 (2005).
112. Ehrst, S. et al. Controlling gene expression in mycobacteria with anhydrotetracycline and Tet repressor. *Nucleic Acids Res.* **33**, e21 (2005).
113. Deep, A., Kaundal, S., Agarwal, S., Singh, R. & Thakur, K. G. Crystal structure of Mycobacterium tuberculosis VapC20 toxin and its interactions with cognate antitoxin, VapB20, suggest a model for toxin-antitoxin assembly. *FEBS J.* **284**, 4066–4082 (2017).
114. Singh, R. et al. Polyphosphate deficiency in Mycobacterium tuberculosis is associated with enhanced drug susceptibility and impaired growth in guinea pigs. *J. Bacteriol.* **195**, 2839–2851 (2013).
115. Bardarov, S. et al. Specialized transduction: an efficient method for generating marked and unmarked targeted gene disruptions in Mycobacterium tuberculosis, M. bovis BCG and M. smegmatis. *Microbiology* **148**, 3007–3017 (2002).
116. Singh, M. et al. Establishing virulence associated polyphosphate kinase 2 as a drug target for Mycobacterium tuberculosis. *Sci. Rep.* **6**, 26900 (2016).
117. Rizvi, Z. A. et al. Golden Syrian hamster as a model to study cardiovascular complications associated with SARS-CoV-2 infection. *Elife* **11**, e73522 (2022).
118. Rizvi, Z. A. et al. High-salt diet mediates interplay between NK cells and gut microbiota to induce potent tumor immunity. *Sci. Adv.* **7**, eabg5016 (2021).
119. Rizvi, Z. A. et al. Pharmacological potential of Withania somnifera (L.) Dunal and Tinospora cordifolia (Willd.) Miers on the experimental models of COVID-19, T cell differentiation, and neutrophil functions. *Front. Immunol.* **14**, 1138215 (2023).

Acknowledgements

This work was supported by the DBT/Wellcome Trust India Alliance Fellowship (IA/S/19/2/504646) awarded to R.S. R.S. is a recipient of the Ramalingaswami fellowship (BT/HRD/35/02/18/2009) and the National Bioscience award (BT/HRD/NBA/37/01/2014). The authors acknowledge the staff members of the BSL-3 facility and experimental animal facility, THSTI for technical help during animal and BSL-3 experiments. The authors also acknowledge the experimental animal facility, NCR Biotech Science Cluster, Faridabad and disease free small animal house, LUVAS for providing mice and guinea pigs, respectively. T.P.G. and S.C. acknowledge DBT and CSIR for their respective research fellowship. The authors sincerely thank late Dr. Ashok Mukherjee for the histopathology analysis. Ms. Neha Rana and Ms. Saruchi Wadhwa are acknowledged for their help with cloning experiments. The authors acknowledge

Agrigenome and Bionivid for bacterial and host RNA sequencing, respectively. The authors acknowledge Dr. Amar Deep, Dr. Deepak Saini and Dr. Sheetal Gandotra for scientific discussions. The authors sincerely thank Dr. Bhabatosh Das, THSTI, for sequencing the genomic DNA of *M. tuberculosis* strains. Mr. Rajesh, Mr. Sher Singh and Ashish are acknowledged for technical assistance.

Author contributions

R.S. conceived the idea and supervised the experiments. T.P.G., S.C., N.K.C. and S.K. performed in vitro and stress experiments. T.P.G., S.C. and N.K.C. performed animal virulence studies. T.P.G. and S.C. performed animal protection studies. T.P.G. and S.C. analyzed bacterial and host RNA-seq data. Z.A., S.C. and T.P.G. performed immune response studies. K.G.T. supervised growth inhibition experiments, A.A. supervised immune response studies. R.S. and T.P.G. wrote the manuscript with inputs from other authors.

Competing interests

The authors declare no competing interests.

Additional information

Supplementary information The online version contains supplementary material available at <https://doi.org/10.1038/s41467-024-49246-5>.

Correspondence and requests for materials should be addressed to Ramandeep Singh.

Peer review information *Nature Communications* thanks the anonymous, reviewers for their contribution to the peer review of this work. A peer review file is available.

Reprints and permissions information is available at <http://www.nature.com/reprints>

Publisher's note Springer Nature remains neutral with regard to jurisdictional claims in published maps and institutional affiliations.

Open Access This article is licensed under a Creative Commons Attribution 4.0 International License, which permits use, sharing, adaptation, distribution and reproduction in any medium or format, as long as you give appropriate credit to the original author(s) and the source, provide a link to the Creative Commons licence, and indicate if changes were made. The images or other third party material in this article are included in the article's Creative Commons licence, unless indicated otherwise in a credit line to the material. If material is not included in the article's Creative Commons licence and your intended use is not permitted by statutory regulation or exceeds the permitted use, you will need to obtain permission directly from the copyright holder. To view a copy of this licence, visit <http://creativecommons.org/licenses/by/4.0/>.

© The Author(s) 2024